Durham E-Theses

Laser Spectroscopy of Wire-Like Molecules

SANDERS, SCOTT,EDWARD

How to cite:

SANDERS, SCOTT,EDWARD (2012) *Laser Spectroscopy of Wire-Like Molecules*, Durham theses, Durham University. Available at Durham E-Theses Online: http://etheses.dur.ac.uk/3482/

Laser Spectroscopy of Wire-Like Molecules

Scott Edward Sanders

Department of Chemistry

Durham University

A thesis submitted for the partial fulfilment of the requirements for the degree of *Doctor of Philosophy*

2011

Declaration

The material contained within this thesis has not previously been submitted for a degree at Durham University or any other university. The research reported within this thesis has been conducted by the author unless indicated otherwise.

Copyright

Acknowledgements

This thesis is the culmination of four years work and would not have been possible without the assistance of a number of people:

First and foremost I offer my sincerest gratitude to my supervisor, E. Wrede, who has supported me thoughout my thesis with his knowledge whilst allowing me the room to work in my own way. His academic experience, patience and answers to ridiculous questions have made these past four years very interesting. I must also thank him for giving me the opportunity to work on this research project under his supervision.

With the late arrival of the CeLIF portion of the experiment I am indebted to several members of the Laser Spectroscopy and Dynamics group here at Durham. N. H. Nahler and O. Willis provided a great deal of input in helping to characterise the CeLIF technique and I thank them for taking time out of their research to help. They have also been invaluable when discussing various aspects of CRDS in both the context of my experiment and as a general subject. Other members of the LSD group, past and present have also played a part in ensuring the success of this project. From "acquiring" various parts and tools from Team Verlet, to purloining pieces from other (A. Rowland's) experiments for incorporation into my own, all have played a part in this research, be it willingly or as a victim. I must also thank S. Matthews and N. Ord for their help in running my actual experiment during their final year research.

From the molecular wire side of things I would like to thank P. Low, Neil and Phil for providing me with the time and supervision to try my hand a pot boiling to synthesise my own sample molecule for analysis. I'd also like to acknowledge A. Beeby for helpful discussions on the behaviour of these electron rich molecules, with a special mention to Bob for the extra BPEB he prepared of the CeLIF measurements. For the simulation work I'd like to thank D. Tozer for his guidance in using Gaussian09 and making sense of the results.

Without the guys in the Electronic and Mechanical workshops none of the additions to the experimental set-up would have been possible. I wish to thank all those involved in these services for working their magic on the less than clear designs and requests I submitted.

Finally I'd like to thank Mam, Dad, Jim, Ryan and Cass for putting up with me over the years and who have supported me during my studies. Without them providing late night pick ups none of this would have been possible.

Abstract

Cavity-enhanced Laser-Induced Fluorescence

With the incorporation of a new optic mount and focussing lens a cavity ring-down set-up was altered to collect fluorescence signal from molecules seeded in a molecular beam. Running both the CRDS and fluorescence measurements simultaneously produced a technique with significantly enhanced sensitivity compared to either of the two individual methods. Preliminary analysis with SO_2 and a selection of polyaromatic molecules point to the method been best suited for measuring the fluorescence spectra of fast fluorescence lifetime (< 1 ns) molecules and in confined environments i.e. molecular beams. This has been characterised using a known sample and also compared to the CRDS and fluorescence measurements ran as individual techniques.

The method was found to increase the sensitivity of the current experimental set-up by two orders of magnitude. This was then applied in the analysis of two new molecular samples to obtain spectra for use in analysing the torsional motions within the molecule.

Torsional Motion Analysis of 2,5-bis(phenylethynyl)thiophene

Torsional motions in polyphenyls, potential molecular wires, are important in the charge carriage capability of the species. Using a combination of UV-cavity ring-down and fluorescence detection the absorption and photoexcitation spectra of 2,5-bis(phenylethynyl)thiophene were successfully measured. Using a simple cosine potential and simulation program the spectra were reproduced and were found to be close to the values determined in previous research on the two ring system tolane and 1,4-bis(phenylethynyl)benzene.

Contents

Chapter 1

Introduction

1.1 Molecular Scale Wires

A fundamental problem running throughout engineering, physics, chemistry and biology is the linking of isolated functional units in order to transport electrons between them. This connection must facilitate the flow of a current between the units, in a predetermined direction and without signal mixing or short-circuits. A solution to this problem is joining the individual units via a simple wire. To be an effective method of connection the wire must control the direction of current flow as well as maintain the topology of the system. Conventional, metal based wires are rigid enough to support the topological structure of the system but are directionless with respect to charge carriage. One of the strengths of metal wiring is the low resistance (R) displayed in their use, which is proportional to the length of wire used (Equation (1.1)).[1]

$$R = \rho \frac{L}{A} \tag{1.1}$$

in which ρ is the resistivity of the conducting material (units of Ω m), L is the length of the wire and A the cross-sectional area of the material.

Traditionally electronics consist of metallic wires for charge transport and inorganic/organic coatings to function as insulators. On the macroscopic scale this is a simple process and can be readily accomplished. However, connecting isolated units on the nanoscale requires ever smaller linkage pieces between them. This can be achieved by decreasing the size of metal wires, requiring progressively more technical means to accomplish this, therefore an alternative is being sought. Instead of working from a top down perspective the smaller scale preparation can be achieved from a bottom up approach. Self assembled monolayers make this concept of small scale assembly a real possibility. The use of individual molecules allows the con-

struction of molecular architectures which can function in a similar way to their macroscale contemporaries. One such possibility is that of molecular scale wiring and functionalities. These molecule sized components can be organic or inorganic in nature, usually consisting of a metal centre connected to adjacent units by an organic linker molecule. These organic connectors serve as molecular scale wires and can shuttle charge between the individual inorganic components. In contrast to metal based wiring it has been found that these architectures display dramatically increased resistance with the lengthening of the molecules.[2]

1.2   Energy and Electron Transfer in Molecules

Energy transfer between species can occur by either direct orbital overlap, whereby the energy moves through the orbitals of one unit to the other, or by ranged methods such as dipole interactions. Electron transfer, however, can only occur via electron exchange schemes, which require orbital overlap.

During energy transfer an energy donor (usually a molecule in an excited state) will interact with an energy acceptor through orbital overlap or longer range methods. These longer range methods include processes such as dipole interactions, where oscillations in the electric field of the energetic molecule affect that of the acceptor, which is subsequently energised to an excited state/level.[3]

Electron transfer requires orbital overlap of the HOMO and LUMO orbitals and as a result it is a much more restrictive method. The interaction between the excited molecule and the second molecular species can be as either the excited molecule acting as the electron donor or as an acceptor. The split in function is a result of the orbitals used in the exchange of an electron (Figure 1.1). In the case of the excited molecule A* functioning as the donor the electron in the the A* LUMO is transferred into the LUMO of the acceptor molecule B. When A* is acting as an acceptor it will accept an electron from the donor B into its HOMO to allow the transfer of the hole generated by the excitation of its electron into the LUMO.

For effective electron transfer from one species to the next consideration must be given to various limiting factors, such as the distance separation between the donor and acceptor and the nature of the separating medium.[2] As the orbital overlap is a critical component in the electron exchange the molecules must remain a minimum distance apart to ensure orbital mixing can occur. To surmount this particular limitation the two units may be linked by a medium capable of supporting electron transfer. This is can be accomplished through the use of either a flexible or rigid linking unit, with the donor and acceptor located at different points.
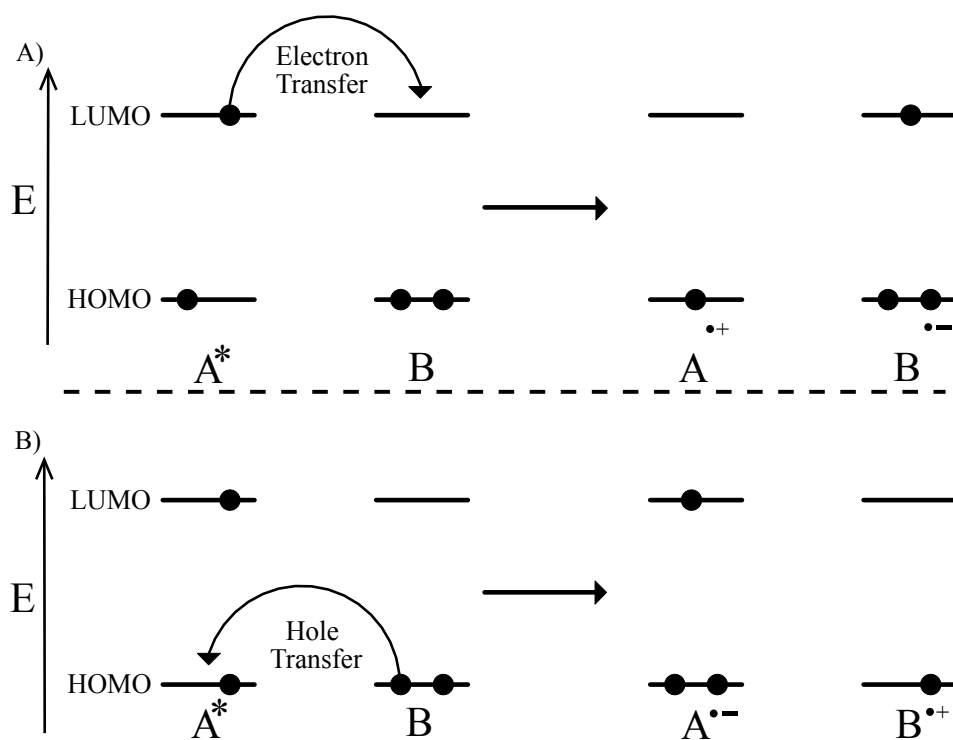
Figure 1.1: Illustration of the excited state molecule, (A*), performing the function of both an A) electron donator and B) electron acceptor in its interaction with a second molecular species (B).

For a physical linkage between the two units, the carriage of the electron must be facilitated via orbital overlap as already stated. The effect of the length of these links tends towards a reduction in the electron carriage efficiency as the length increases.[4] The actual mechanism for the movement of an electron through the bond again involves the HOMO and LUMO of the donor and acceptors, and also those of the connecting medium. Through the use of linkage units, composed of species with HOMO and LUMO energy levels similar to those of the donor and acceptor molecules, the various orbitals can mix and facilitate the transport of the electron from one molecule to the other.[5] This carriage of the electron through the bonds of the bridge unit, electron superexchange, occurs as the LUMO of the excited state can mix with a bridge LUMO, such as a π^* orbital, and so the electron has a reasonable chance to move through this bridge unit LUMO until it is deposited in the LUMO of the acceptor. Alternatively the HOMO of the donor and the acceptor can interact with that of the molecular bridge in a similar fashion to the LUMO. With the units now linked the hole generated in the excited molecule also has a reasonable chance of traveling the length of the linking unit to the acceptor, resulting in the complimentary transfer of an electron from the ground state molecule to the excited state (Figure 1.2). The mechanism which occurs is mainly governed by how well the LUMO interacts with the antibonding orbitals of the bridge and for the hole

transfer it is the mixing of the bonding orbitals of the bridge with the HOMO of the donor and acceptor.
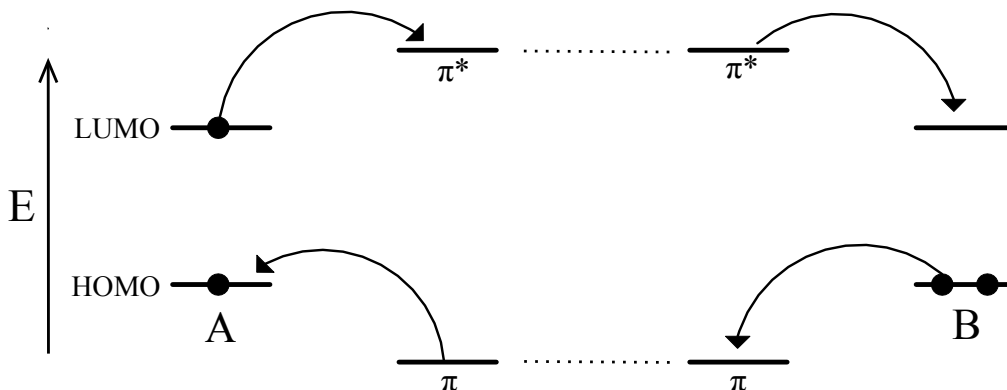
Figure 1.2: Through bond electron transfer using π and π^* orbitals. σ orbitals can also facilitate the carriage of electrons.

1.3 Molecular Scale Wires

In 1974 Aviram and Ratner[6] postulated that a molecular species comprising a donor-spacer-acceptor could function as a molecular scale diode. The nanoscale assembly could function by allowing the flow of electrons from the cathode to the acceptor portion and the anode receiving electrons from the donor section of the unit, with the system allowing the flow of current in one direction only. To accomplish this the makeup of the diode would need to be tailored to allow this oneway flow of electrons across the system. With the experimental realisation of the charge carrying characteristics of delocalised molecular systems[7] the concept of molecular scale architectures capable of functioning in a similar fashion to conventional charge carriers became a more realistic possibility. As in this experimental study, one of the simplest forms of molecular wire is a linear chain of sp/sp^2 hybridised carbon atoms, with alterations incorporated accordingly in the form of double/triple bonds to generate a conjugated system. The delocalised system allows the π and π^* orbitals to function as facilitators for charge carriage along the length of the system.[8]

1.3.1 Polyaromatic Molecules

In systems such as chlorophyll the absorption of photons results in the excitation of systems based around polyaromatic molecular sub-units, for chlorophyll this is

achieved through a porphyrin structure. The delocalised nature of the polyaromatic component of the pigment allows the energy or an electron to move through the orbitals along the length of the molecule. In addition to chlorophyll there are other examples of charge carriage capability in the natural world. DNA has also been described as a molecular level charge conductor,[9;10] or "molecular wire", with the movement of electrons facilitated by polyaromatics via π-stacking interactions between base-pairs.

The majority of these conjugated molecules are characterised by delocalised states. In the mid 1970s it was found that these π electron rich materials were highly susceptible to chemical or electrochemical oxidation.[11] This factor could then be used to modify the molecule's optical and electrical properties over wide ranges and thus allow the systems to be tailored for a particular purpose. On the basis of this a wide body of research has evolved analysing a plethora of different features and characteristics, including changing the source of the π system with units such as alkynes,[12] porphyrins[13] and polyphenyls.[14] These units have been researched as both architectures to enhance the conducting capabilities of metal centres[12] and as bridges between the units themselves.[15] A class of polyaromatic molecules which has received a large body of interest is that of polyarylethynyl molecules.[16–18]

1.3.2 Simple Polyarylethynyl Molecular Systems

Polyarylethynyl molecules possess a highly rigid, conjugated structure, consisting of discrete units of aromatic rings connected by ethynyl bridging sections (Figure 1.3). Owing to the structure of the molecules, the aryl rings can rotate around the C(sp)-C(sp^2) bonds that link the rings to the ethynyl bridges. The extended, linear π-conjugated system runs along the principal molecular axis of the system, with the rotation of the aryl rings highly influential on the molecules properties and performance.[19]
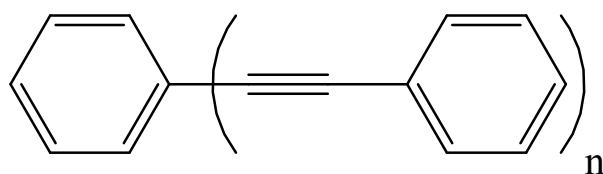

Figure 1.3: Repeating unit of a polyphenylethynylene.

Tolane (diphenylacetylene) is the simplest polyarylethynyl molecule and has been studied extensively from both a theoretical and experimental aspect.[20–24] Interest in the molecule results from the separation between the phenyl rings being such that

the steric effects of the opposite ring are negligible, and so the degree of twist between the rings is primarily influenced by the level of conjugation in the molecule.[25] From the substituted tolanes many other polyaryls have been studied which have different functional groups attached to alter the electronic properties of the conjugated system (Figure 1.4).[24;26]
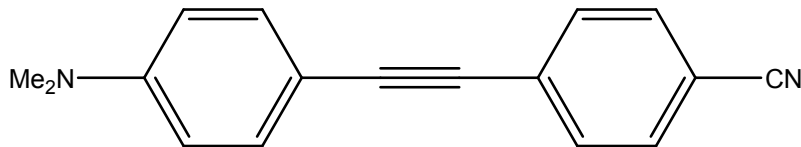
Figure 1.4: A substituted tolane derivative, p-dimethylamino-p'-cyano-diphenylacetylene, studied using picosecond time resolved methods.[26]

Increasing the complexity of the molecule from tolane, one polyarylethynyl molecule which has received strong attention is 1,4,bis-(phenylethynyl)benzene (BPEB). Several studies have been conducted into the properties of molecules based around the BPEB framework for use as a molecular scale wire.[16;27;28] Solution phase measurements of the basic architecture have shown it to have a high fluorescence quantum yield ($\Phi_F = 0.75$ in hexane and 0.9 in MeCN)[29] and a fluorescence lifetime typical of many similar molecules ($\tau_F = 0.63$ ns).[19] Gas phase measurements have yielded differing values of $\Phi_F = 0.58$ and $\tau_F = 0.85$ ns for the quantum yield and fluorescence lifetime respectively.[30]
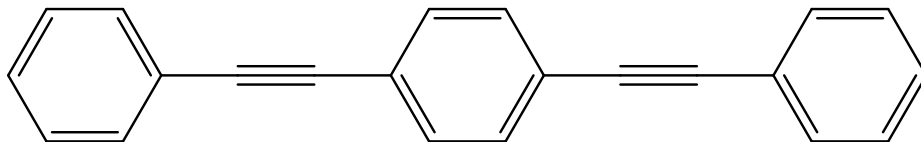
Figure 1.5: 1,4-bis(phenylethynyl)benzene.

Levitus *et al.*[31] carried out absorption, fluorescence and phosphorescence measurements of BPEB in a variety of solvents, which pointed towards the presence of two or more absorbing species. Further investigation revealed the presence of two spectroscopically distinct structures as opposed to a continuum. Cooling the BPEB samples to 77 K in methylcyclohexane allowed the identification of these two probable entities, with one conformer absorbing at higher wavelengths than the other. The structure exhibiting absorbance at shorter wavelength was deduced to be the planar conformation, while the longer wavelength absorption was a structure with the central ring perpendicular to the outer two. The phosphorescence displayed by BPEB was recorded showing a weak spectrum, with an approximate phosphorescence lifetime of 447 ms. Upon further scrutinisation of the absorption data, by Beeby,[32] it was determined that the two structures were actually caused by an impurity in the BPEB sample. Subsequent measurements by the Levitus group (using

a new sample) found that the longer wavelength absorbance between 350-370 nm no longer appeared and the emission measurements also required alteration. The remaining data on the affect of the solvent environment was found to still be reliable and so the group's conclusions on the solvent influence on the molecules fluorescence were still valid. In addition to the solvent environment affecting the photophysical properties of BPEB, changing the length of the chain of molecules which follow the BPEB framework has also been found to alter the absorption and fluorescence profiles recorded, depending on whether the chain is lengthened or shortened.[33]

Levitus *et al.*[34] have also spectroscopically analysed 9,10-Bis(phenylethynyl)anthracene and found that it too displays properties which are reliant on the conformation of the molecule with respect to the orientation between successive phenyl rings. This molecule has also been investigated for its charge carrying capability by placement between two gold electrodes, in which they postulated the molecule's symmetry delivered an advantage over an asymmetric alternative.[35]

Studies of this class of molecule have been carried out which show the molecule and its derivatives displaying several interesting electronic characteristics such as controlled switching and a reduced voltage at higher applied currents (negative differential resistance (NDR)).[16;18;36–38] These studies were accomplished using self-assembled monolayers of the sample molecule tethered to a gold plate via a sulphur bridge. This then allowed the substrate layer to be probed via either an additional gold contact or scanning tunnel microscopy (STM). While these studies appear to indicate good electronic properties, it has been suggested that the conductance measurements may be due to the formation of gold nanowires between the lower gold plate and the STM tip.[39]

As previously mentioned, molecules which contain the BPEB framework, but possess substituted portions of the ring, exhibit NDR, with derivatives such as 2-amino-4,4-di(ethynylphenyl)-5-nitro-1-benzenethiol (Figure 1.6) receiving significant interest.[16;18;36;37] In the study by Chen *et al.* the pure BPEB and amine substituted derivative displayed no NDR characteristics, while the framework possessing an NO_2 substituent did show the switching from high conductance to lower with application of increasing current.[18] Although BPEB was found not to display NDR research has shown it to possess random conductance switching behavior when tethered to a dodecanethiolate monolayer matrix with a, subsequently, applied voltage.[37]

Sluch *et al.*[40] analysed the dynamics exhibited by structures based around the core BPEB framework (Figure 1.7) using absorption, steady-state and picosecond emission measurements. The results of scans carried out in $CHCl_3$ indicated the Franck-Condon envelope of the absorption spectrum was more broadened than that of the
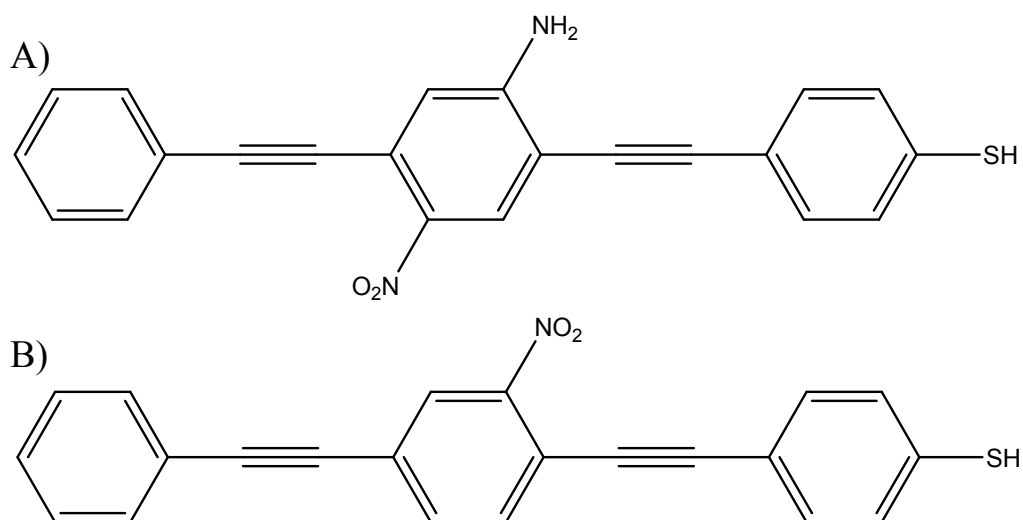
Figure 1.6: A) 2-amino-4,4-di(ethynylphenyl)-5-nitro-1-benzenethiol and B) 4,4-di(ethynylphenyl)-2-nitro-1-benzenethiol. Both derivatives of BPEB display negative differential resistance when placed between gold eletrodes.

emission spectrum. When dissolved and suspended in a restrictive matrix of olgiostyrene, at 77 K, the molecule was found to have an emission spectrum which closely mirrored that of its absorption profile. To test this the group then measured the spectra once again, using the olgiostyrene as a solvent at 300 K, which resulted in a spectrum between that of the $CHCl_3$ and the low temperature matrix. Interpretation of the results lead to the group suggesting the dynamics being dominated by the collective twisting of the phenyl rings relative to the planar configuration. This conclusion was based on the low barrier of rotation of the phenyl rings in the ground state.
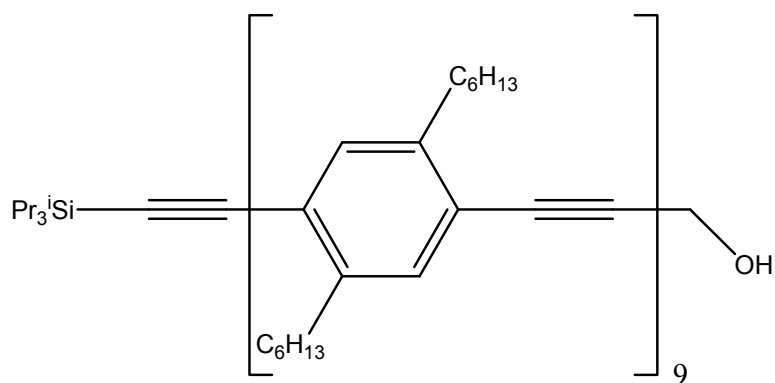
Figure 1.7: Oligo(p-phenyleneethynylene) molecule analysed by Sluch *et al.*

Additionally, it was noted that the first excited state also favoured a planar conformation. As a result the molecule possess a broad thermal distribution, allowing a large number of conformers to be adopted in the ground state. With a broad distribution the molecule can subsequently absorb over a wide range into the first

excited state. In the $CHCl_3$ measurements the emission spectra are narrower than the associated absorption distribution, which was attributed to the viscosity of the solvent. $CHCl_3$ has a sufficiently low viscosity that the excited molecules can quickly return to a planar conformation and so the subsequent emission frequency distribution is narrower than the corresponding absorption. The restrictive matrix (77 K) of olgiostyrene meant that the excited state could not rearrange back to the planar conformation and so the emission spectra reflects that of the absorption. The viscosity of the olgiostyrene when used as a solvent meant that the rate at which the molecule could move towards a planar conformation in the excited state was more inhibited than in $CHCl_3$. This restriction of movement meant that the rearrangement time was close to that of the fluorescence time of the molecule (350 ps). Consequently the spectra obtained for this intermediate case were between the two extremes of $CHCl_3$ and olgiostyrene matrix.

Further measurements using time-correlated single-photon counting, with an instrument response function of 45 ps and excitation with a 397 nm pulse, of the sample in $CHCl_3$ revealed no shift of the emission peak position, but did show a collapse of the blue edge. This collapse had a time constant of 60 ps, illustrating the steady-state spectrum was relaxed in the solvent. The same measurements carried out in the olgiostyrene solvent produced a decay time of 0.5 ns, very similar to that of the fluorescence lifetime of the molecule (350 ps), pointing towards the steady-state only having achieved partial relaxation. Comparison of the two results point to the more viscous solvent (olgiostyrene) prolonging the relaxation time of the molecule and, hence, the viscosity of the medium influencing the rate of relaxation in the molecule.

1.3.3 Effects of Ring Torsion

The spectroscopic and electronic properties of polyaromatics is a major driving force for the continued interest in this class of molecule, with the extended, linear π system they display being the basis for these interesting characteristics. This reliance on the conjugation means the molecular properties are susceptible to any change in the degree of conjugation afforded by the molecule at a particular time.

The characteristic twisting motion between the phenyl rings of these molecules demonstrates the low barrier to rotation, at room temperature, in species such as BPEB.[41] With the interest in these systems as potential molecular charge carriers it is necessary to restrict this twisting motion to prevent the breaking of the conjugation between the rings. Examples of limiting this motion are means such as Langmuir films[42] and self-assembled monolayers.[43]

Studies into the internal rotational energy of the attached phenyl rings around the C≡C of small polyaromatic molecules have yielded results which indicate a low energy barrier to the motion.[25;44] One of the simplest molecules, tolane, has an experimentally determined barrier of $\approx$ 200 cm^{-1} (2.4 kJ mol^{-1}).[23] Early calculations concluded that the calculated torsional potential (the twisting of the phenyl rings) displayed a minimum when the rings were perpendicular, and a maximum when coplanar.[20;21] Computational methods have yielded more accurate results for the torsion potential of the tolane system, indicating a lower energy conformation in the coplanar molecular state.[22;45] Application of ab initio,[46;47] and further quantum mechanical methods such as DFT,[17] have produced results which are in much greater agreement with experimental evidence with regards to the torsional motion around the tolane C≡C.

These investigations were carried out on units with only a single C≡C between two aromatic rings. Theoretical simulations of the torsional energy of these molecules are found to significantly over estimate this barrier.[48] Investigations into larger molecules have produced results which also indicate low barriers for these species, such as that of Greaves *et al.* which estimated the rotational barrier in 1,4-bi-(phenylethynyl)benzene to be around 220-235 cm^{-1}, yielding a result similar to that of tolane.[41]

Initial explanation was provided by Bunz *et al.* into the effects of the twisting aryl groups on the characteristics displayed by the molecules.[49;50] Through comparison of theory to both absorption and emission spectra they were able to relate their experimental data to the calculated molecular structure. The results pointed to the energy spacing between the HOMO and LUMO of the molecule increasing as the dihedral angle between the adjacent rings changed from a more planar conformation to that with perpendicular rings.

Solution phase fluorescence studies conducted on BPEB indicated the conformation adopted by the molecule in its lowest energy state is planar.[19;31] Absorption studies have found similar trends,[30;41] with these carried out under similar experimental conditions used by Okuyama *et al.* in the deduction of the rotational barrier in tolane.[23] Analysis of the frontier orbitals of the BPEB molecule, and its derivatives, show the effects of the molecule adopting a planer or twisted conformation.[31;36] The π orbitals are delocalised across the entire molecule in the planar configuration (Figure 1.8) but become restricted to the central ring in the twisted configuration.

Upon electronic excitation from the HOMO (π) to the LUMO (π^*) the bonding character of the molecule changes to weaken the alkyne triple bonds, but strengthen those between the phenyl ring and the nearest alkyne carbon (Figure 1.9). It has
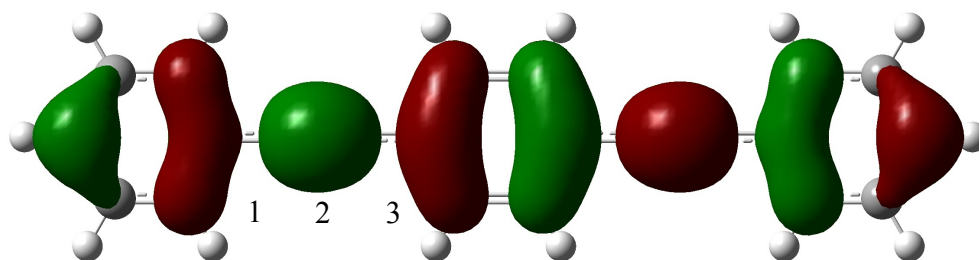
Figure 1.8: Planar geometry adopted by 1,4-bis(phenylethynyl)benzene displaying the HOMO orbital. Points 1 and 3 show orbital nodes between the alkyne triple bond and the benzene rings.

been found that in its excited state the molecule does not lose its alkyne bond character,[27] however, with the placement of a node on the triple bond a reduction in electron density will lead to a weakening of this bond. Coupled with the shared density between the phenyl ring and its linking alkyl carbon, the excited state displays, overall, a much greater potential energy well.[41]
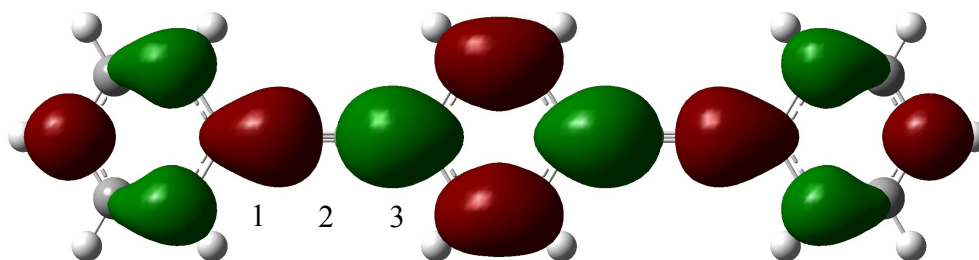
Figure 1.9: Planar geometry of 1,4-bis(phenylethynyl)benzene LUMO. Shown is the change in orbital distribution, whereby point 2 displays a node and points 1 and 3 now exist as bonds between the benzene ring and alkyne carbons.

1.4 Spectroscopy

Spectroscopy is the study of the absorption, emission or scattering of electromagnetic radiation by matter. When interacting with a sample radiation can cause a transition between energy levels within the molecule should it satisfy certain selection rules. These transitions are electronic, vibrational and rotational in nature, with electronic transitions requiring the greatest energetic input. When a photon contains insufficient energy to generate an electronic transition in the molecule the energy can be absorbed by means of vibrational or rotational excitation. In this instance the molecule can be excited to a higher lying ro-vibrational level within the same electronic state.

Spectroscopic measurements are concerned with the radiation measured resulting from an external source interacting directly with the sample (absorption or scattering type spectroscopy) or by the sample itself producing the radiation for detection (emission type spectroscopy). Absorption spectroscopy uses the principle that the analyte can absorb photons with an energy corresponding to a transition within the molecule, be that electronic, vibrational or rotational in nature, allowing a picture of the different states within the molecule to be constructed.

Emission based spectroscopic techniques use the fluorescence and phosphorescence generated from the relaxation of an excited state molecule. By dispersing the emitted light the fate of electrons and vibrations, excited with a particular frequency of energy, can be determined. This gives an indication of the energy levels occupied in a state after relaxation. This in turn can provide information about the internal states of atoms and molecules, however; a problem is that not all absorptions lead to an emission.

A major application of spectroscopy is to measure the concentration of an analyte, which can be explained by considering the Beer-Lambert law.

1.4.1 Beer-Lambert law

$$A = \log_{10} \frac{I_0}{I} = \varepsilon(\bar{\nu})Cl \qquad (1.2)$$

Equation (1.2) describes the relationship between concentration (C, mol dm^{-3}), sample pathlength (l, usually cm) and the ability of a molecule to absorb a photon of a particular wavenumber (extinction coefficient, $\varepsilon(\bar{\nu})$, dm^3 mol^{-1} cm^{-1}). When radiation of intensity I_0 travels distance l through and interacts with a sample medium of concentration C, the emerging intensity will be reduced to I. The Beer-Lambert

law (in this form) is generally applied when carrying out absorbance measurements in the solution phase. Gas phase measurements tend to make use of the equivalent equation

$$I = I_0 \exp(-\sigma \rho l) \tag{1.3}$$

where σ is the absorption cross-section of the molecule (m^2 molecule^{-1}), ρ is the particle density (molecule m^{-3}) and l is again the pathlength.

In both equations there is a direct relationship between concentration and pathlength (when operating at a fixed wavelength), thus a reduction in one can be compensated for with an increase in the other. For practical purposes the sample pathlength can only be increased to a certain point to allow for a reduction in the concentration of a species. However, eventually a point will be reached when distinguishing a reduction in I_0 will become extremely difficult as a result of the concentration becoming too low.

Historically, analytical spectroscopy has been carried out using broadband light sources such as tungsten light bulbs or deuterium discharge lamps, depending on the wavelength range required. As the light passes through the sample volume and emerges through the other side it is then dispersed into its component wavelengths by a series of prisms or gratings in a monochromator. A problem with conventional absorption based spectroscopic methods is that it can be difficult to detect very weak absorptions from a sample or from a low concentration of the particular species being analysed. From Equations (1.2) and (1.3) it can be seen that by having a small concentration, or low molecular absorption coefficient/cross-section, the actual absorbance will be very small. This weak absorption will thus only produce a small change in the intensity of the light beam and, hence, makes it difficult to distinguish between the intensity of the emerging light and that from before it entered the sample (the reference beam). The sensitivity problem can be alleviated by considering the third component of the Beer-Lambert equation, that of the pathlength. By increasing the pathlength of the analyte the beam will be reduced by a more easily detectable amount. In order to increase the pathlength to a sufficient degree for low concentration detection Cavity Ring-Down Spectroscopy (CRDS) uses multiple passes, of the same laser pulse, through the sample volume.

1.5 Cavity Ring-Down Spectroscopy (CRDS)

Placing two highly reflective mirrors in such a manner as to create a cavity enables the confinement of a laser pulse. After entering the cavity the laser pulse is reflected from the surface hundreds, if not thousands, of times. With each successive reflection a small portion of the laser light exits the cavity. It is this small amount light escaping the cavity which is detected and used to determine the length of time the pulse remains confined within the cavity, known as the ring-down time (Figure 1.10).
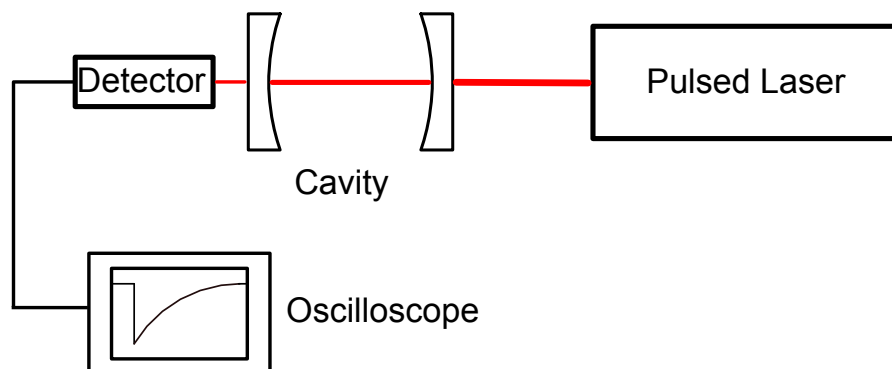
Figure 1.10: A simple CRDS set-up comprising of a laser source, reflective cavity and detection equipment.

CRDS has been used as an analytical technique in solid, solution and gas phase measurements, with the bulk of CRDS application with respect to analysis of samples in the gas phase.[51–53] The (usual) lower density of molecules in a gas phase sample, coupled with the ease to which it can be placed within the cavity for accurate analysis, makes gas phase measurements the most routine to perform. The example of Dube *et al.*[53] even uses the installation of a CRDS system on an aircraft to enable simultaneous *in situ* measurements of NO_3 and N_2O_5 concentrations in the atmosphere. Measurements in the solid and solution phases are becoming more common, with applications to the solid phase using both an extra substrate to mount the sample[54;55] or the mirrors themselves as the substrate.[56] Applying CRDS to the solution phase also presents the problem of the substrate used to contain the fluid for analysis. Different methods can be employed to overcome this, including filling the entire cavity with the solution[57] or placing the solute containing cuvette in at the Brewster angle.[58] In a similar vein CRDS can be used to study surface processes via the use of Evanescent Wave Cavity Ring-Down Spectroscopy (EW-CRDS).[59;60] This method combines the multi-pass nature of CRDS with the total internal reflection used in the production of evanescent waves to create a technique capable of probing condensed phase substrates (Figure 1.11). As the confined beam is reflected from the surface it generates an evanescent beam which has a small portion of light

"leak" to the other side of the prism surface. This leaked light returns to the pulse within the prism should no other factors effect it. A substrate which absorbs at the laser frequency can remove this leaked light, resulting in a reduction in the lasers ring-down time in the cavity.
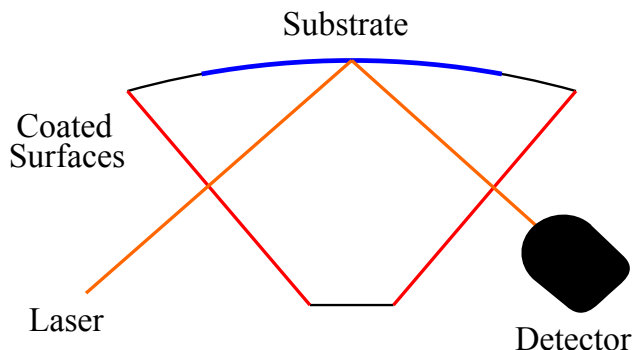

Figure 1.11: EW-CRDS carried out using a monolithic resonator. The coated surfaces (red) act as the high reflectivity mirrors to confine the laser beam. As the confined light is reflected by the upper surface it generates an evanescent wave which can be used to probe condensed phase substrates (blue).

1.5.1 Development of CRDS

CRDS was first devised as a technique by O'Keefe and Deacon[61] based on previous research and observations carried out by Herbelin *et al.*[62] and Anderson *et al.*[63] during the 1980s. The work of Herbelin *et al.* and Anderson *et al.* provided an accurate method for measuring the reflectivity of low loss mirrors by means of measuring the lifetime of a trapped laser pulse. The work by Herbelin *et al.* was based around modulating the frequency of a continuous wave (cw) laser to measure the reflectivity by trapping a resonant frequency of light between mirrors which comprised the cavity. By analysing the phase-shift of the trapped pulse they were able to determine the length of time the pulse had been confined and so determine the reflectivity of the mirrors used. Anderson *et al.* improved upon this idea by switching the cw laser off through the use of a fast optical switch. The switch was triggered via the detector sending a signal when the light emerging from the cavity reached a threshold value. This method allowed the group to measure the actual decay time of the pulse as it left the cavity. In both methodologies a problem is that the confinement of the light is only to a select few narrow cavity modes, owing to the lasers bandwidth.

O'Keefe and Deacon further altered the set-up by exchanging the cw-laser with a pulsed laser. This was done to surmount the problem of the matching of the laser

frequency with a single cavity mode. Additionally the electronics could be simplified as there was no need to monitor the power in the cavity as the laser pulse acted as the trigger. With this significantly simplified set-up the weak $b^1\Sigma_g^+ \leftarrow X^3\Sigma_g^-$ absorption in atmospheric oxygen was analysed and recorded (Figure 1.12)[61].
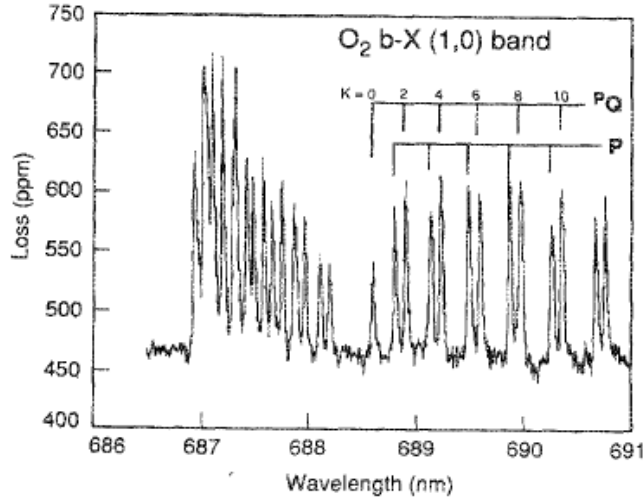
Figure 1.12: Absorption spectrum of O_2 displaying the $b^1\Sigma_g^+ \leftarrow X^3\Sigma_g^-$ transition.

1.5.2 Principles of CRDS

The cavity is typically made from two highly reflective mirrors with reflectivity >99.95%. As the laser pulse encounters the first mirror it will lose most of its power as it will be reflected back from the high reflectivity coating as it moves through the mirror into the cavity. Once the laser pulse enters it will bounce back and forth between the two mirrors, leaking a small amount ($1 - R$ with each reflection, where R is the mirror reflectivity) of the laser light which entered the cavity. The confined pulse progressively reduces in intensity by a factor of R^2 with each complete round trip between the two mirrors. After k round trips between the mirrors the initial pulse intensity (I_0) in the cavity is reduced by:

$$I_k = I_0 R^{2k} = I_0 \exp\left(2k \ln R\right) \tag{1.4}$$

Each round trip will have a corresponding time it takes to complete, $t_r = 2L/c$, c being the speed of light and L the distance between the two mirrors. The time the pulse remains within the cavity can be described using the number of round trips by $t = k \times t_r$. The gradual reduction in the signal intensity (I_t) can thus be written as

$$I_{(t)} = I_0 \exp\left(\frac{tc \ln R}{L}\right) \tag{1.5}$$

22

Since $R \approx 1$, it can be assumed that $\ln R \approx -(1-R)$. Equation (1.5) can then be re-written as

$$I_{(t)} = I_0 \exp\left(\frac{-tc(1-R)}{L}\right) = I_0 \exp(-t/\tau_0) \tag{1.6}$$

where τ_0 is the empty cavity ring-down time of the pulse, that is the time taken for the signal amplitude to fall to $1/e$ (≈ 0.37) of original intensity. The value of τ_0 is related to both the length of the cavity and also the reflectivity of the mirrors used,

$$\tau_0 = \frac{L}{c(1-R)} \tag{1.7}$$

In the absence of any absorbing/scattering medium (i.e. in vacuum) the only loss experienced in laser intensity is that from the mirrors. When an absorber is present and interacts with the laser pulse the loss is attributed to the mirror and also absorption by the absorbate (in addition to losses from light scatter by the sample etc), resulting in the original τ_0 reducing to τ'.

$$\tau' = \frac{L}{c(1-R+\alpha d)} \tag{1.8}$$

in which d is the distance the beam travels through the absorbing medium and α is the absorption coefficient, the product of the absorption cross-section, σ, and the sample number density, ρ.

$$\alpha = \sigma\rho \tag{1.9}$$

From Equation (1.7) it can be seen that the ring-down time has no dependence on the laser intensity, thus shot-to-shot variations in laser power should have little effect on the results. By recording the ring-down time of an empty cavity (τ_0) and then one containing a sample of absorbing medium (τ') it is possible to extract an absorption spectrum of the species in question, carried out using the relationship

$$\frac{1}{\tau'} = \frac{1}{\tau_0} + \alpha c \tag{1.10}$$

if the sample volume probed is across the length of the cavity. Should the sample pathlength (d) be less than the cavity length (L) the absorption coefficient must be appropriately scaled using a slightly altered version containing $\alpha c \frac{d}{L}$.

From the ring-down time it is possible to determine other parameters of the cavity, namely the number of round trips the beam makes in the cavity, N_r, where t_r is the round trip time, and the effective pathlength of the cavity, D_{eff}.

$$N_r = \frac{\tau_0}{t_r} = \frac{\tau_0 c}{2L} \tag{1.11}$$

23

$$D_{\text{eff}} = \tau_0 c = \frac{L}{1 - R} \tag{1.12}$$

1.5.3 Mode effects

A resonant cavity is formed when a particular frequency of radiation is confined within a set space by multiple mirrors. The confinement is possible only when the radiation field satisfies the condition of having a node (zero amplitude) at the reflective surfaces. With the need to maintain waves that are in phase, and so constructively interfere, the condition of zero amplitude is only satisfied when multiples of half-wavelengths can be fitted between the reflective surfaces.[64] This restriction defines the longitudinal modes, with the size/width of modes and spacing between adjacent modes (Figure 1.13) given by the cavity finesse ($\mathcal{F}$=1600 for our cavity) and the free spectral range (FSR=0.6Hz) respectively.[65]

$$\mathcal{F} = \frac{\pi\sqrt{F}}{2} = \frac{\pi\sqrt{R}}{1 - R} \tag{1.13}$$

where F is the finesse coefficient,

$$F = \frac{4R}{(1 - R)^2} \tag{1.14}$$

$$\text{FSR}(\Delta v) = \frac{1}{n2L\cos\theta} \approx \frac{1}{2L} \tag{1.15}$$

In which Δv (Hz) is the spacing between consecutive modes, n is the refractive index of the medium, θ is the angle of incidence and L is the cavity length.

The FWHM of these modes can be calculated using the ratio between the free spectral range and the cavity finesse

$$\text{FWHM} = \frac{\text{FSR}}{\mathcal{F}} \tag{1.16}$$

In order to be detected a sample must have an absorption feature which overlaps with at least one of the active cavity modes. Those which have features which do not encompass any of the modes will not contribute to the increase in the signal decay rate of the confined beam. The use of pulsed laser sources allows multi-mode excitation, from the bandwidth of the laser light, and thus dramatically reduces this problem. Cw-lasers, however, have much narrower bandwidths and so it is much more difficult to couple into the correct mode for the absorption feature. Whilst the broader bandwidth of a pulsed laser leads to a more easily established
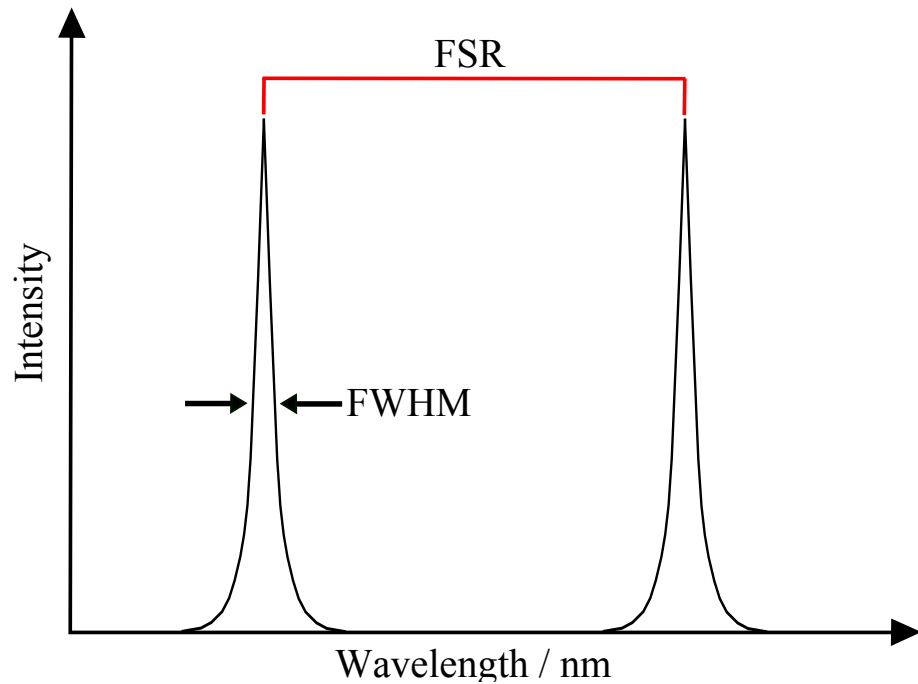
Figure 1.13: Illustration of the free spectral range and finesse displayed by a cavity. The free spectral range describes the spacing between successive modes in the cavity, while the finesse influences how narrow these modes will be. With increasing mirror reflectivity comes a narrowing of the cavity modes.

ring-down event it can also cause problems with the previously mentioned multiple excited modes as they can yield multi-exponential decays. If the laser light frequency corresponds to a transition within the absorbing medium the refractive index will increase. This means the absorbed laser light frequency will come out of phase with the remaining wavelengths confined within the cavity modes. When emerging from the cavity these out of sync frequencies can cause destructive interference and so mode beating can be seen on the signal trace. This is of particular importance when detecting an absorption feature which is narrower than the bandwidth of the laser.

In addition to the number of longitudinal modes excited by a laser pulse, the pulse can also display deviation from the laser axis. This variation is described by the notation TEM_{qmn} (Transverse Electromagnetic Modes), where the m and n subscripts denotes the number of nodes in the two perpendicular directions to the laser propagation (longitudinal) axis and q describes the longitudinal mode.[66] The frequency identity can be determined using;

$$\nu_{qmn} = \frac{c}{2L}\left[q + \frac{2}{\pi}\arctan\left(\frac{L}{\sqrt{L(2r-L)}}\right)(m+n+1)\right] \qquad (1.17)$$

r being the radius of curvature of the mirrors which confine the laser pulse. The spacing between adjacent transverse modes (changing $m + n$ but with a fixed q

value) is given by Equation (1.18).[67]

$$\left(\frac{c}{\pi L}\right) \arctan\left(\frac{L}{\sqrt{2r - L}}\right) \tag{1.18}$$

The most basic of these is the TEM_{00}, a pure longitudinal mode with respect to the laser axis and displays a Gaussian distribution of intensity. Higher order modes are excited when the oscillating wave deviates from the beam path and propagates in a manner off axis to the traveling beam. These result in signal mode beating on the decay trace.

1.5.4   Minimum Detection Limit

The lowest absorption coefficient (α_{min}) which can be measured using CRDS corresponds to the smallest change in τ_0 which can be distinguished and accurately recorded.

$$\alpha_{min} = \frac{(\tau_0 - \tau)_{min}}{c\tau_0\tau} \simeq \frac{\Delta\tau_{min}}{c\tau_0^2} \tag{1.19}$$

If the reflectivity of the mirrors is accurately known the limit can be found by incorporating R into the calculation of α_{min}.[68]

$$\alpha_{min} = \frac{1 - R}{L}\left(\frac{\Delta\tau}{\tau_0}\right)_{min} \tag{1.20}$$

The obtainable accuracy of τ is determined by many factors, for example, the laser system (bandwidth, modes and power), cavity (mirror reflectivity and modes), detector, data acquisition and data analysis.[69] The main factor in the current project was mirror reflectivity. With better mirror performance (higher reflectivity) comes a longer ring-down time, which will result in a greater sensitivity owing to the reduction in the fractional error value in accordance with Equation (1.20). Mirrors optimised for use with ultraviolet wavelengths perform poorly, when compared to those used in the visible region, and so the ring-down times are comparatively short ($1 - 5\mu s$ (UV) vs $\geq 40\mu s$ (Visible)).

1.5.5   Molecular Wires and CRDS

CRDS has previously been used to obtain an absorption spectrum of BPEB (Figure 1.15) to gain an understanding of the torsional motions of the molecule.[41] The UV absorption spectrum of BPEB at room temperature is broad as a result of the thermal distribution in the molecule. By making use of a supersonic expansion

this distribution was reduced and the ground state vibrational levels more easily accessed. CRDS was employed as the greater sensitivity afforded by the technique meant the sample could be detected in the low concentration environment of the expansion. Through the use of a custom simulation program peaks in the spectra were assigned to the symmetric and antisymmetric twisting motions (Figure 1.14). It was found that a large portion of the molecules experienced free rotation at room temperature, leading to the conclusion that BPEB was not a suitable candidate for a molecular wire.
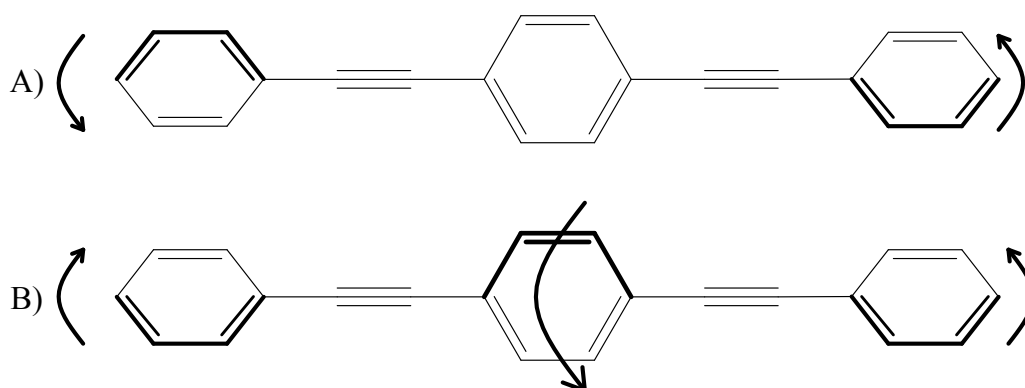
Figure 1.14: A) Antisymmetric and B) symmetric normal mode twists of BPEB.
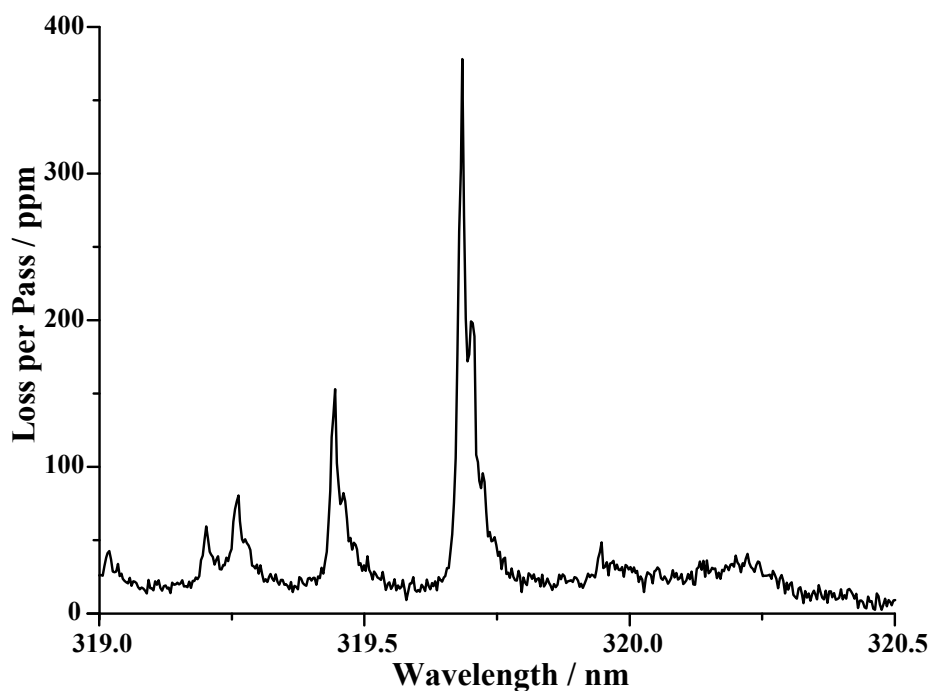
Figure 1.15: Absorption coefficient of BPEB obtained via CRDS in a molecular beam.

Chapter 2

Experimental Setup

2.1 Original Vacuum Chamber

As this research was the continuation of a previous project (carried out by S. Greaves[70]) the overall set-up was carried over from this work. The vacuum chamber consisted of a 6-way cross (BOC Edwards, 100/80 ISO-K/F) (Figure 3.4). The top flange was used as the feedthrough point for the molecular beam carrier gas and supports the nozzle assembly.
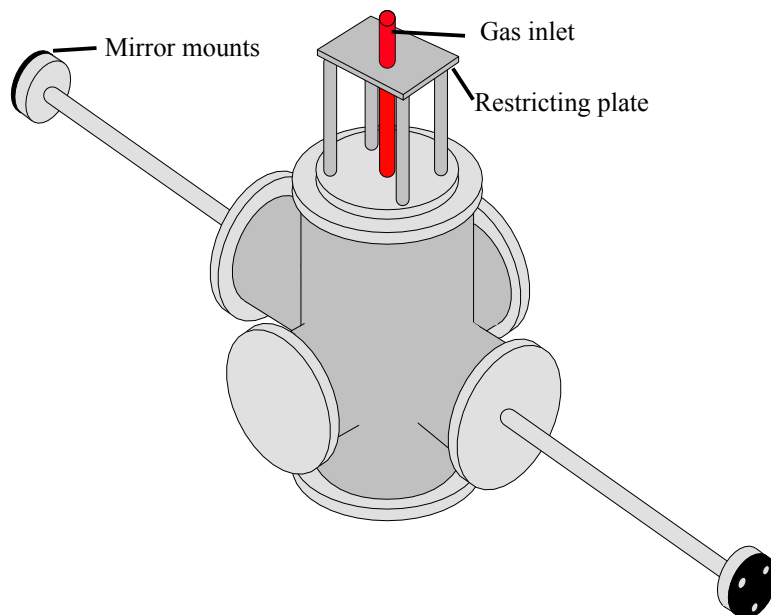
Figure 2.1: Vacuum chamber set-up with CRDS mirror mounts.

The vacuum diffusion pump (BOC Edwards, Diffstak CR100/300, 230 L s^{-1}) backed by a rotary pump (Oerlikon Leybold Vacuum, DB16 Trivac, 16 m^3 h^{-1}) was mounted

on the bottom flange. This allowed the chamber to be pumped to $\approx 10^{-6}$ mbar, with the pressure monitored using a Penning gauge (Edwards CP25K). The laser axis is defined by the centres of the mirror mounts supported by DN16CF flanges, producing a laser pathlength of approximately 0.85 m between the mirrors.

A subsequent summer project carried out by N. Andrews and R. Smith enabled the accurate measurement of the laser cavity length. Using a 1 GHz oscilloscope (LeCroy, Waverunner 104Xi) and a fast PMT (Hamamatsu H3695-10, rise time 0.7 ns) the frequency of the cavity was determined by Fourier transform analysis. The cavity frequency ($\bar{\nu}$) corresponds to $1/t_r$ (where t_r is the laser pulse roundtrip time) and can be related to the cavity length by

$$2L = \frac{c}{\bar{\nu}} \tag{2.1}$$

where c is the speed of light. A cavity frequency of approximately 177.7$\pm$0.1 MHz was found, yielding a cavity length of 84.36$\pm$0.05 cm.
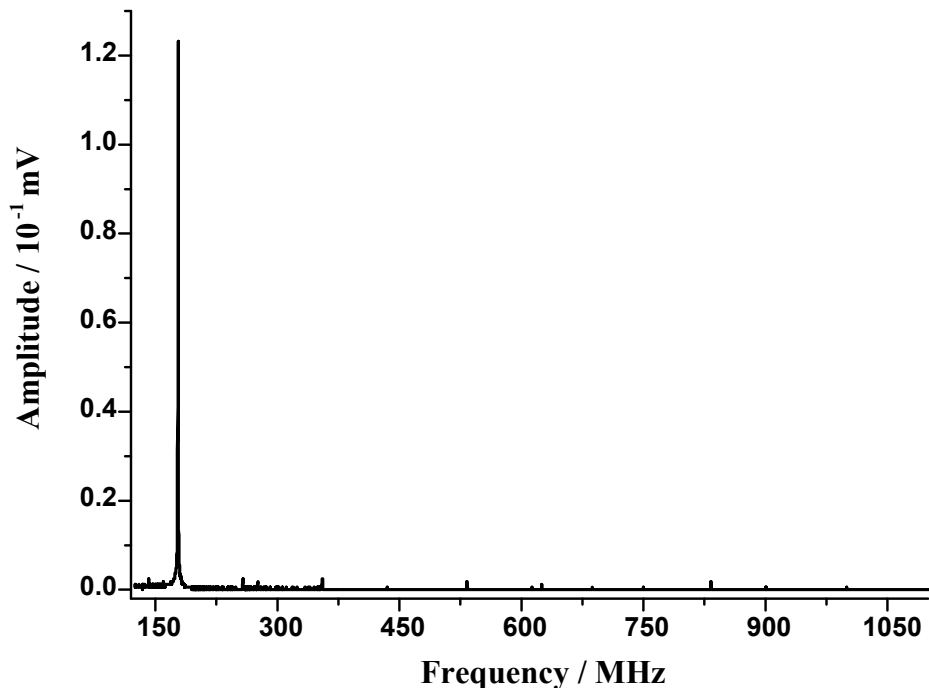

Figure 2.2: The frequency spectrum of the laser cavity, as shown after Fourier transform analysis. The main peak is at a frequency of $\approx$ 177.7 MHz.

Using the Fourier transform analysis the transverse modes of the cavity could be minimised, as seen in Figure 2.2 where the Fourier transform has only a single strong peak.

2.1.1   Sample Analysis

The ultimate goal of this research project was the measurement of an absorption spectrum of a sample molecule. This could then be used in conjunction with a simulation program to determine approximate torsional energies for the respective sample species. An absorption spectrum can be obtained though standard methods using a spectrometer, however, at room temperature these spectra will be broad and unstructured. While this can be used to determine certain aspects of a molecule's absorption profile, such as a charge transfer band, for our purposes it was insufficient.

To obtain a useable spectrum the sample is cooled using a molecular beam set-up. Broadly speaking a molecular beam cools by reducing the number of populated states in a molecule. This means that the transitions obtained during a scan start from fewer energy levels. With this reduced number of transitions comes a simplified spectrum for interpretation.

Supersonic Molecular Beams

When two molecules collide and subsequently fly apart they can undergo one of two processes. They can scatter elastically, where translation energy is exchanged, or inelastically, in which case in addition to translational energy they can also exchange internal (vibrational and rotational) energy. The basic premise for generating a molecular beam is the transfer of a sample gas from a region of high pressure/low volume to a region of significantly lower pressure/larger volume. A molecular beam can be generated using the pure sample under study (should it be a gas), or through the use of a carrier gas with the species under scrutiny seeded within it. Carrier gases tend to be one of the noble series, with their cooling ability a result of their lack of vibrational and rotational energies. As a result of this they do not impart a significant amount of energy to a colliding sample species.

Within the region of high pressure the mean free path (Equation (2.2))[71] of the molecules will be smaller than in the vacuum chamber.

$$\text{MFP} = \frac{k_B T_0}{\sqrt{2}\sigma p_0} \qquad (2.2)$$

where k_B is the Boltzmann constant, T_0 the temperature of the gas inside the nozzle (K), σ the molecular cross-section (m^2 molecule^{-1}) and p_0 the pressure of the gas (Pa). Using a p_0 pressure of 4 bar, and temperature of 300 K, of argon carrier gas moving into a vacuum of 1×10^{-6} mbar the mean free path changes from 2 nm to 8 m. This change in mean free path is an important factor in the production of a

molecular beam.

Initially the gas begins in a region of high pressure, the stagnation state (p_0, T_0).[72] By creating a pressure difference $(p_0$-$p_1)$ the molecules move to the lower pressure region. For a successful supersonic expansion the mean free path of the molecules must be smaller than the diameter of the exit orifice.[73] This maximises the collisions between molecules in the source volume as they move into the low pressure region, undergoing inelastic and elastic scattering with one another. Upon exiting the channel the flow undergoes a supersonic expansion, with the centre of the beam containing those molecules which are cooled to the greatest extent, displaying free molecular flow.[72]

By channeling the molecules from a high pressure region to one of lower pressure, through an orifice which is larger than the mean free path after the exit orifice, the number of collisions will be reduced and so the mean free path increases. During the time before exiting the channel the molecules collide with the carrier gas and transfer energy through intermolecular collisions. These collisions continue to occur as the molecules exit the orifice. As the molecules in the beam move away from the exit they begin to average out their velocities through elastic collisions. The collisions have the effect that the molecules momentum take on the same direction. As the molecules move downstream they travel at similar speeds and so the number of collisions occurring are dramatically reduced. Since the velocity distribution, and so the kinetic energy, of the molecules is narrow they display a lower translational temperature. With the low translational temperature comes lower rotational and vibrational energies. As the rotational and vibrational populations are lower than at room temperature the spectra are produced from fewer populated states. The result of this is that the spectra are simplified by a reduced number of transitions. The degree of cooling can be controlled to allow a balance to be struck between reducing the spectral features and the number of available features to analyse in the spectrum.

Usual practice can also involve the addition of a skimmer downstream from the nozzle to assist in the production of a more refined beam by removing the outer portion of the expansion, leaving only the (cooler) central portion.

The gas pulse was generated using a pulsed valve (Parker Instrumentation, General Valve, series 9, 0.5 mm orifice, with IOTA ONE pulse driver), attached to the feedthrough pipe of the top flange. The timing of the nozzle fire was controlled via a delay generator (BNC model 565 pulse delay generator) which was triggered by the laser pulse.

Seeding the Sample in the Pulse

A hurdle to cross is that the molecules chosen for analysis are solid at room temperature. The aim of the experiment is the study of the molecules as individual units (gas phase). To successfully analyse the sample in a molecular beam it is therefore necessary to vapourise the molecules. A copper oven was used to heat the sample until sublimation occurred and allowed the sample vapour to be "picked up" by the carrier gas. The oven was developed during the previous research by S. Greaves[70] as an addition to the pulsed valve, and is based on a design used for the sublimation of amino acids for study using a supersonic expansion.[74]
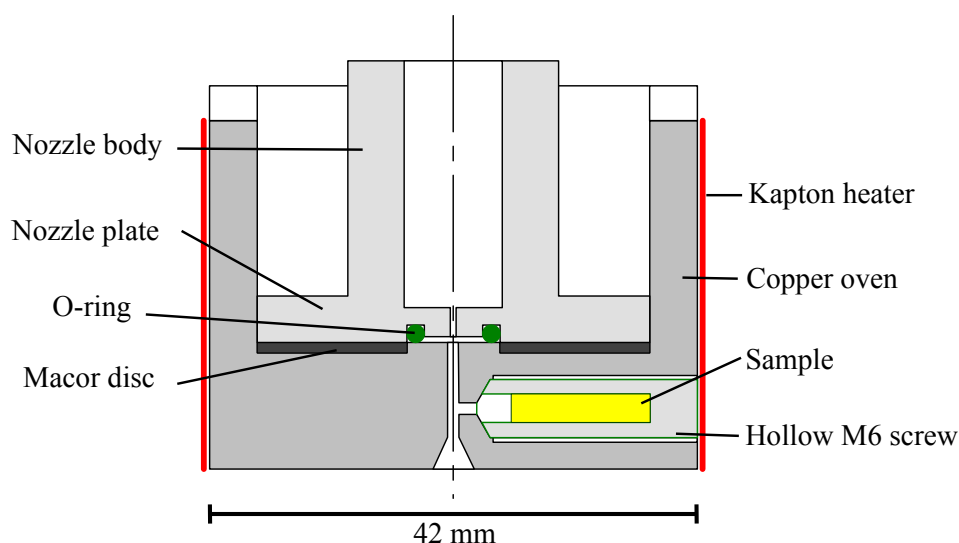
Figure 2.3: Vertical cut through of the cylindrical sample oven attached to the pulsed nozzle.

To seed the sample molecules into the supersonic expansion the solid is placed into a hollow M6 screw, located in the side of the oven. The oven is heated, using a flexible heating strip (Omegalux, Kapton flexible heater), until the solid sample sublimes and the vapour travels through into the main channel where it can then be picked up by a carrier gas pulse. Once seeded in the carrier gas the sample is carried further down the channel to the 1 mm exit orifice. A ceramic disc (Macor) is used to alleviate some of the conducted heat from the copper oven to the General Valve assembly. When exiting the oven, the gas expands and cools via a 3 mm deep, 40° cone.[75]

The feedthrough was also used to adjust the position of the nozzle and oven assembly. Using an O-ring (Ultra-Torr, Cajun fitting) sealed portion it could be raised or lowered to alter the height of the oven relative to the laser axis (Figure 2.4). Lateral movement was also possible and allowed the positioning of the oven exit orifice over the decaying pulse. Additionally, the mount was designed to allow the adjustment

of the tension in the nozzle springs. This altered the opening characteristics of the nozzle poppet and subsequently the molecular beam profile/quality.

The unskimmed molecular beam then intersects the laser beam at a right angle 3-5 mm downstream of the oven exit. For this experiment no skimmer was used as the density of the sample molecules was low and so it was decided skimming off any of the sample would be a hinderance. This, combined with height difference between the oven exit and the laser beam, assisted in maximising the sample length for the ring-down set-up and, hence, increasing the sensitivity.
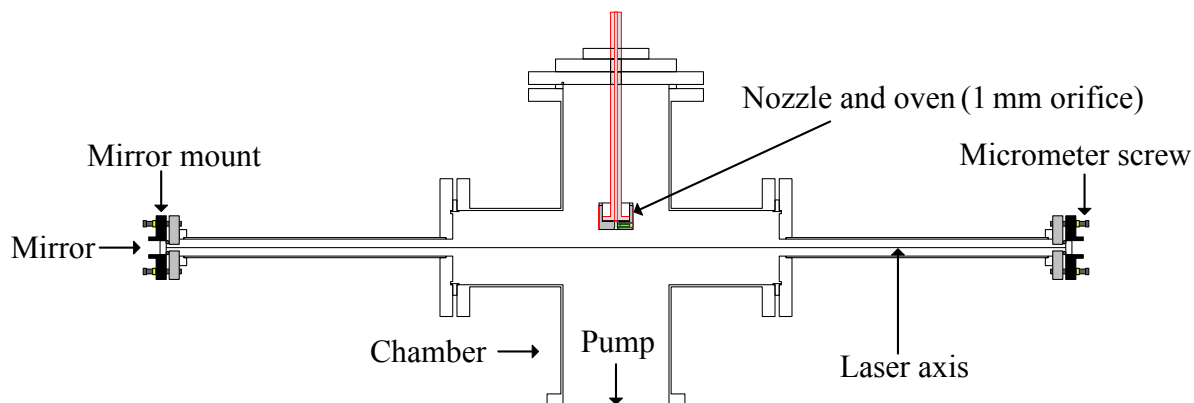
Figure 2.4: Vacuum chamber set-up with CRDS mirror mounts.

2.1.2 New Additions to the Existing Design

Mirror Mounts

While developing a new undergraduate teaching lab experiment, based on Cavity Ring-Down Spectroscopy, a major requirement was the design of a simple, small and robust mirror mount. Whilst testing the new mount in the teaching lab it was found that they performed extremely well, and thus were incorporated into the existing research experiment. The initial configuration, used in the undergraduate lab, was a Delrin mount with a recess for a $0.5''$ mirror. The depth was such that the mirror would protrude approximately 2 mm from the surface of the Delrin piece. Positioning the mirror against an O-ring and the addition of micrometre screws (Owis, FGS Fine-thread Screw, with 35 mm travel) allowed the alignment of the mirror to be accomplished by exploiting the flexibility of the O-ring. The micrometre screws exerted a pull on the Delrin mount altering, the angle of the mirror on the O-ring and forming the sealing surface of the vacuum.

A problem encountered with the mounts was the cleaning of the mirrors after ex-

posure to the samples under investigation. The constant removal of the micrometre screws proved stressful on the threads and so a new design was adopted. The new mounts comprised 3 separate parts, namely the mirror holder, a mount for the holder (which also acted as the mirror adjustment plate), both being machined from Delrin, and finally the stainless steel mount to connect the Delrin mount to the DN16CF extension piping of the chamber. The addition of a separate area to house the mirror allowed easier cleaning and also eliminated the need to remove the micrometre screws when doing so. This additional portion was attached to the main Delrin section via three M6 screws.
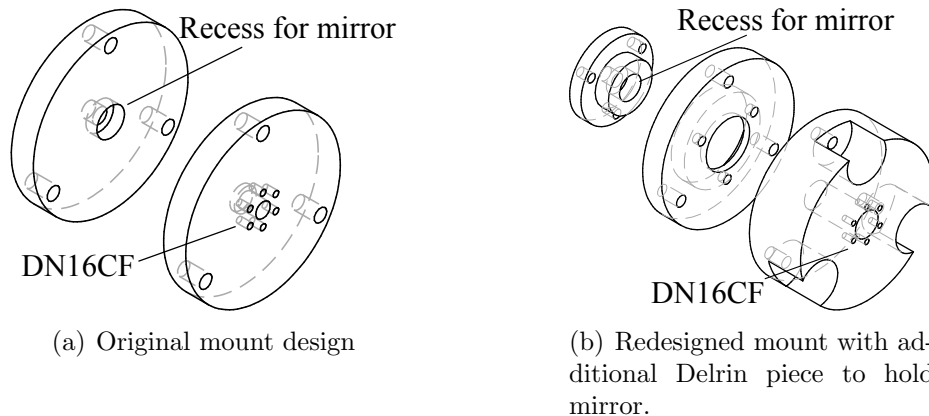

(a) Original mount design

(b) Redesigned mount with additional Delrin piece to hold mirror.

Figure 2.5: Evolution of the mirror mount used to establish optimum ring-down time.

Beam Quality Analysis

Being able to monitor the temporal profile quality of a molecular beam is a useful tool when working to cool molecules. This allows both the optimal conditions to be achieved, but also to monitor the condition of the poppet used in the nozzle (to ensure poppet degradation was not influencing the beam quality). Originally this was accomplished through the use of a fast ionisation gauge (FIG),[70] however, this was unavailable due to its incorporation into another experiment.

Since the gas pulse is itself a pressure wave a microphone (Knowles Acoustics, SPM0204UD5, Ultra-son-acoustmems4) was mounted to one of the chamber flanges at 90°C to the laser axis. A magnetic push-pull (Kurt Lesker, MPPL-100-H) was used as the mount, which allowed the manipulation of the microphone in a longitudinal direction below the molecular beam. The microphone converts this pressure wave into a measurable voltage. It was anticipated that the voltage output of the microphone would be small and thus an approximate value was calculated.

$$L_{\mathrm{dB}} = 10\log\frac{P_1}{P_0} \tag{2.3}$$

where L_{dB} is the nominal microphone performance at 1 kHz (dB), P_0 the sensitivity value of the microphone (1 V/Pa at 0 dB) and P_1 is the new microphone power reading (V/Pa) (both at 1 kHz).

Using Equation (2.3) and the nominal sensitivity of -42 dB (as supplied by the manufacturer) an approximate value of 0.63 mV was determined. To ensure a sufficiently strong signal would be generated by the molecular beam striking the microphone membrane an approximate density was calculated using Equation (2.4) and used to determine an approximate signal strength.[72]

$$\frac{\rho}{\rho_0} = \left(1 + \frac{\gamma - 1}{2}M^2\right)^{-\gamma/\gamma-1} \tag{2.4}$$

where γ is the ratio of the heat capacities (C_p/C_v) of the gas and M is the mach number of the expansion. The mach number can be approximated by[72]

$$M = A\left(\frac{x - x_0}{d}\right)^{-\gamma/\gamma-1} - \frac{0.5\left(\frac{\gamma+1}{\gamma-1}\right)}{A\left(\frac{x-x_0}{d}\right)^{-\gamma/\gamma-1}} \tag{2.5}$$

in which A is a tabulated constant dependant on γ and x_0 are constants relative to the heat capacity at set pressure (C_p), x is the distance from the exit orifice to the microphone and d is the exit orifice diameter.

Table 2.1: The parameters used in determining an approximate value for the Mach number and number density in the molecular beam.

γ	A	x_0/d	x / mm	d / mm
1.67	3.26	0.075	25	0.5

It was found that with an approximate molecular beam density of 4×10^{21} m^{-3} yielded a pressure of $\approx$ 112 Pa at the microphone. This was determined using the relationship

$$P = \frac{F}{A} = \rho\nu^2 m \tag{2.6}$$

where P is the pressure (Pa), F (kg m s^{-2}) is force, A is the area (m^2), ρ the number density (m^{-3}), ν the velocity of the molecular beam (ms^{-1}) and m the atomic mass of the species in the molecular beam (kg). As the major component of the beam was the argon carrier gas the calculations were performed based on a pure argon beam. An approximate signal strength of 70 mV was determined for the microphone response.

During initial trials with the microphone it was found that the performance was not
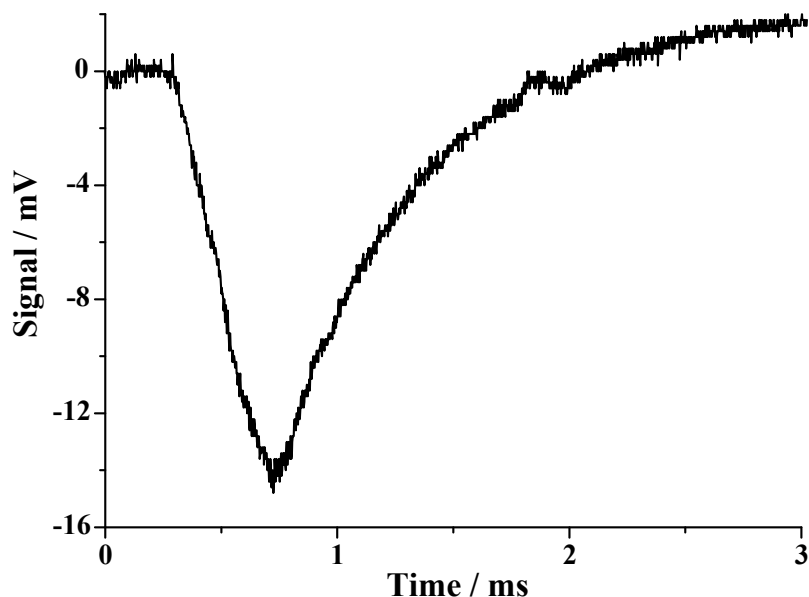
Figure 2.6: A preliminary signal trace from the microphone.

that of the anticipated signal levels (Figure 2.6). With a replaced poppet and opti-
mised conditions it was found that the signal from the centre of the molecular beam
could be in excess if 100 mV. With the addition of the microphone the beam quality
could be monitored and altered to produce a quality supersonic expansion. The
best results achieved were those when using a short, sharp pulse (FWHM between
200-300 μs).

Optimal Molecular Beam Conditions

With the addition of the microphone the performance of the nozzle pulse could
be monitored *in situ*. The quality of the signal from the supersonic expansion
was changed through a mixture of backing pressure adjustment, altering the spring
tension in the nozzle housing, the height of the oven exit channel relative to the
laser beam axis and the duration of the opening time for nozzle.

Adjusting the backing pressure allowed an alteration in the pressure ratio between
the sample line and the vacuum chamber. An increase would thus allow a greater
degree of cooling as more carrier gas would be present to remove the energy from
the sample. However, an increase in pressure caused an additional strain on the
pumping system, at a chamber pressure greater than 1×10^{-3} mbar the change in
ring-down signal reduced, pointing towards a poor expansion. This was verified using
the microphone, which indicated the FWHM of the molecular beam had increased
to ≈ 400 μs and the profile was poor.

The poppets eventually became deformed as a result of the heating of the nozzle and
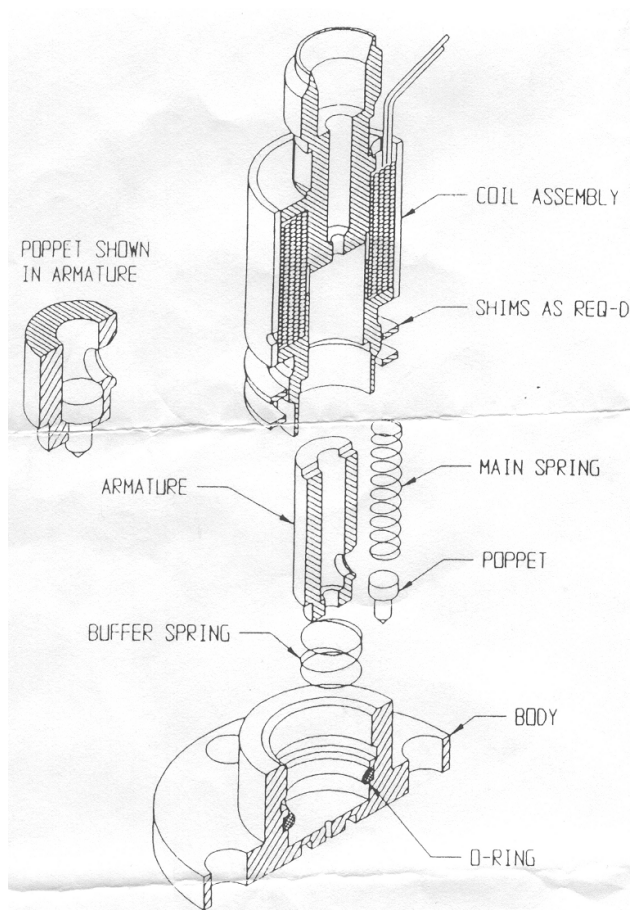
Figure 2.7: Schematic drawning of the General Valve used in the production of the molecular beam, as supplied by Parker Instruments.

the frequent impacts from the repetition rate. The poppets used were composed of PTFE and were found to be useable for only a very limited time before becoming too damaged for further use. More durable poppets were employed (Parker, PI(Vespel) poppets), which resulted in the poppet never requiring changing. Taking both the backing pressure and poppet quality into account the optimised conditions for successful signal detection were 4-5 bar backing pressure and an approximate chamber pressure of 2×10^{-4} mbar.

Altering the distance between the exit orifice and the laser beam required a balance between signal strength and spectrum quality. The exit of the oven was placed a minimum distance of 3 mm from the laser beam in order to ensure the molecular beam signal resulted from free molecular flow. The closer the nozzle was to the laser beam the higher the number density in the molecular expansion, however, the temperature range of the beam was also much greater. This would lead to signal with more intensity but broader absorption features as a result of the warmer peripheral sections of the expansion. Increasing the distance between the two allowed these warmer sections to lessen in effect, but would lead to reduced number density.

Figure 2.8 (a) illustrates the quality of spectra which were obtained using a poor expansion configuration. As the supersonic expansion is hindered by the poor opening of the poppet, or the shaping of the PTFE piece, the sample molecules are not cooled as effectively. As a result of this the absorption features of the molecules are broader than those of more refined beams. The poorer cooling means the sample molecules will have a greater number of initially populated states according to the Boltzmann distribution.
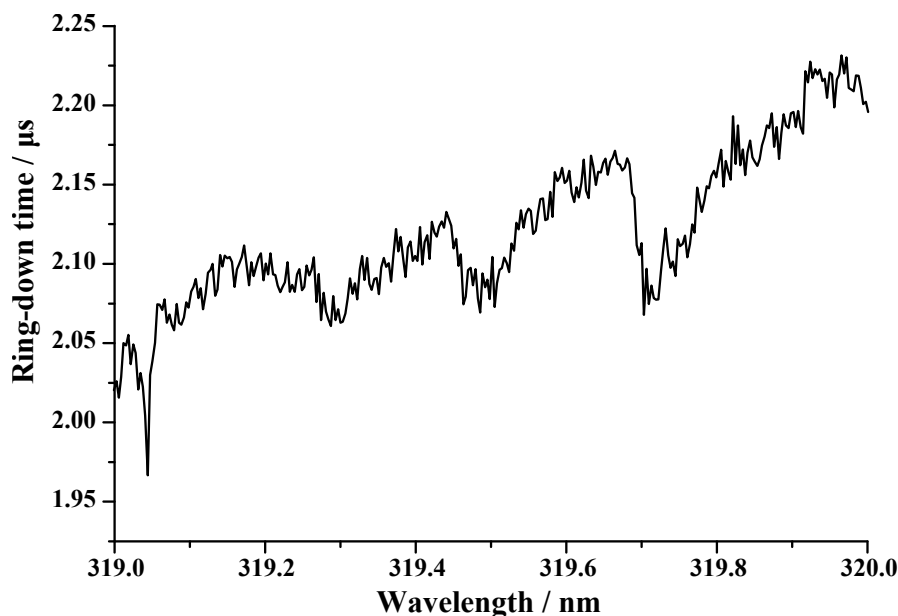
(a) Ring-down scan of BPEB obtained using poor quality PTFE poppet.
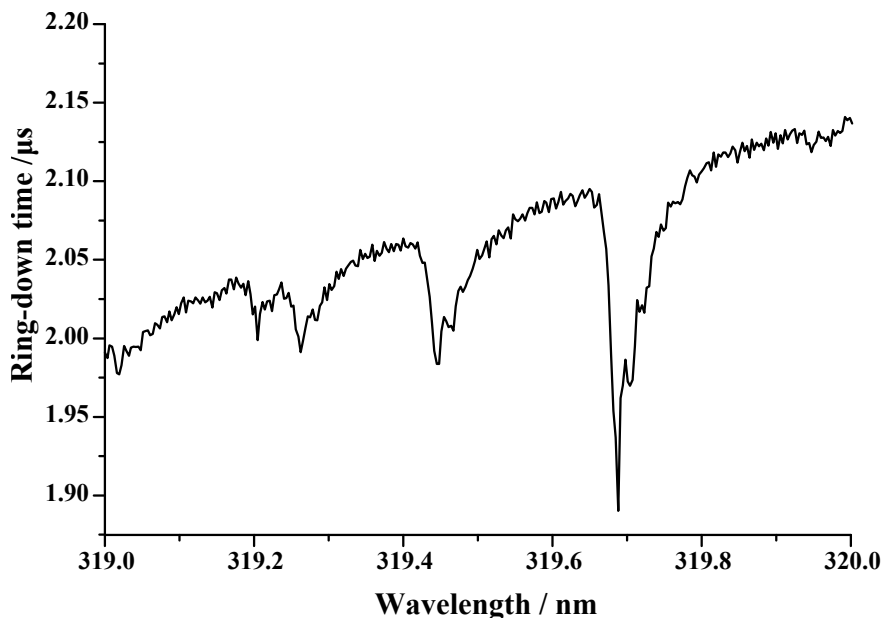
(b) Ring-down scan of BPEB obtained using a good quality poppet.

Figure 2.8: Quality comparison between spectra obtained with a poor and a good supersonic expansion profile.

By using a better quality poppet, be that PTFE of Vespel, the absorption profile of a molecular beam can be significantly improved (Figure 2.8 (b)).

Sample Oven

A second generation oven unit was designed which incorporated an hour glass shaped exit, mimicking a de Laval nozzle, to replace the straight channel of the original oven. The intention of this redesign was to allow more sample vapour to collect in the chamber before becoming seeded in the molecular beam. The asymmetric shape was also hoped to aid in the cooling of the heated sample by the argon gas (Figure 2.9).
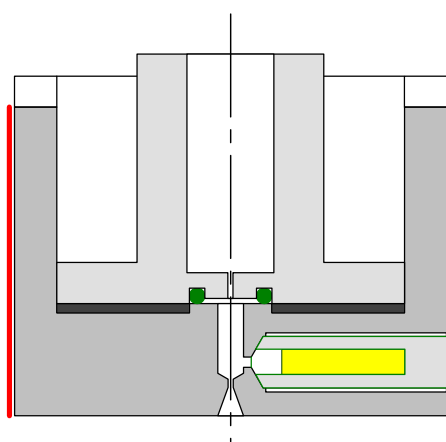
(a) The redesigned oven unit incorporating a de Laval based exit section.

1 mm orifice
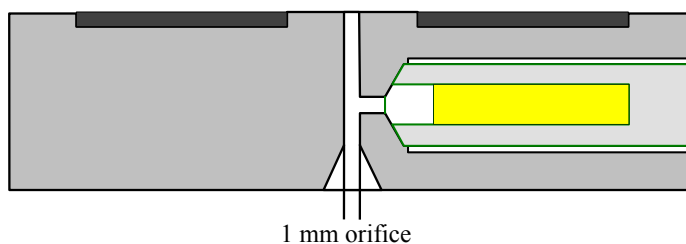
(b) Original oven channel.

0.5 mm orifice
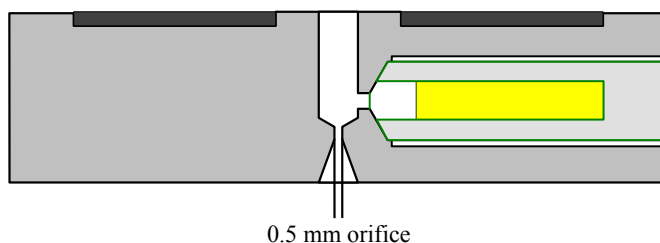
(c) Redesigned oven channel incorporating a narrower exit orifice.

Figure 2.9: Comparison between exit channels of the two different oven designs.

During the previous work on the torsional motions of BPEB it was found that the

sample distribution in the molecular beam was located primarily towards the rear of the gas pulse,[70] where the greatest reduction in ring-down time was observed. With the re-design of the copper oven and the addition of the microphone for pulse optimisation the beam was once again analysed. This was accomplished by monitoring the reduction in ring-down time in relation to the nozzle fire time. By monitoring the reduction of the ring-down signal from the main absorption feature at 319.68 nm of BPEB a rough estimate of sample distribution in the beam could be acquired. As the gas pulse was progressively timed to arrive before the ring-down event the ring-down time reduction distribution could be seen to have the greatest reduction around the centre of the pulse (Figure 2.10). This pointed to the sample being distributed in a more uniform manner throughout the beam pulse.[76] An alternative explanation could be the presence of clusters in the beam. The initial spike in ring-down time reduction (towards the front of the pulse) could be the result of the individual molecules. The width of the pulse is consistent with Figure 2.6, while the broader portion of the ring-down reduction could be from the presence of dimers and larger clusters in the rear portion of the molecular beam.
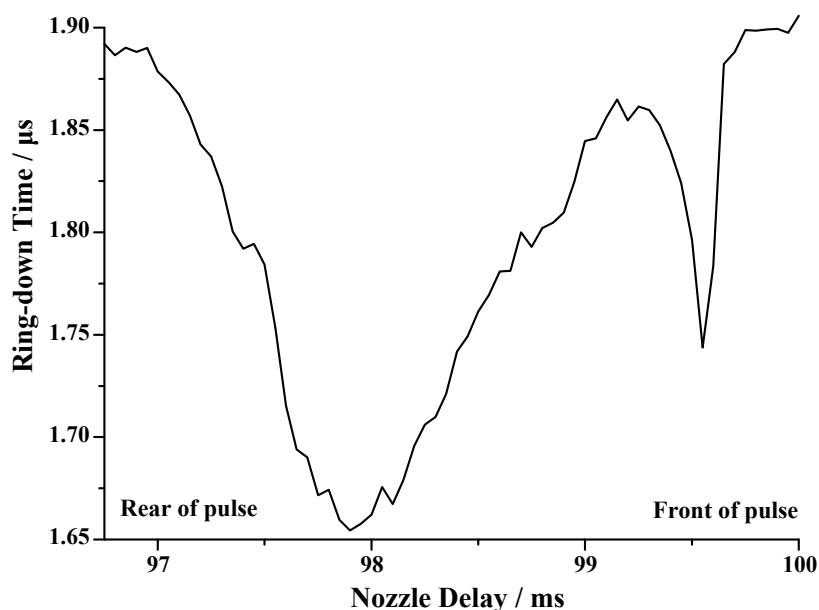
Figure 2.10: Reduction in ring-down time as a function of nozzle delay. Where previously the main reduction concentration of sample molecule was towards the end of the pulse the new oven provides a distribution towards the centre. Note that longer nozzle delay corresponds to earlier portions of the molecular beam.

With the capability to monitor the quality of the gas pulse and incorporation of the de Laval section of the new oven a greater degree of cooling of the sample was achieved when compared to the original oven design (Figure 2.11), as evident from the fewer peaks in the spectrum. However, the signal from the original oven design displays a superior signal-to-noise ratio compared to that achieved with the new

design. This may result from the molecules cooled in the redesigned oven having a smaller thermal population distribution, or be a result of the newer design actually producing a less dense sample pulse in the molecular beam. This may be due to the larger orifice size of the original oven allowing a greater portion of the sample into the chamber.
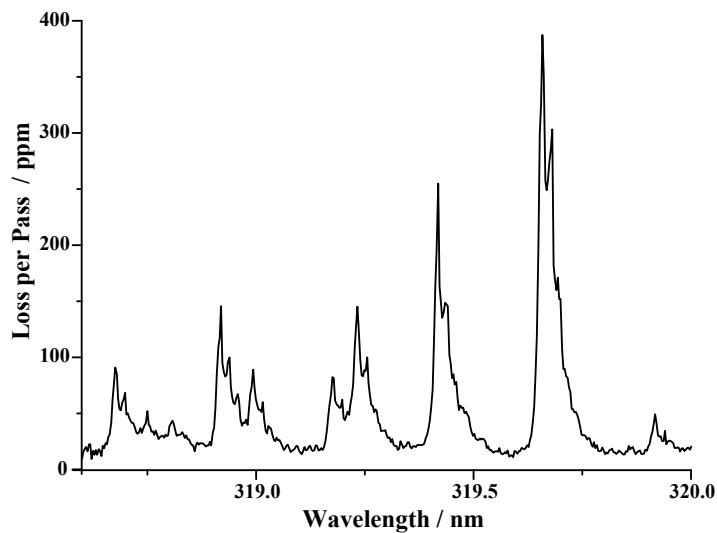
(a) Performance of original oven design.
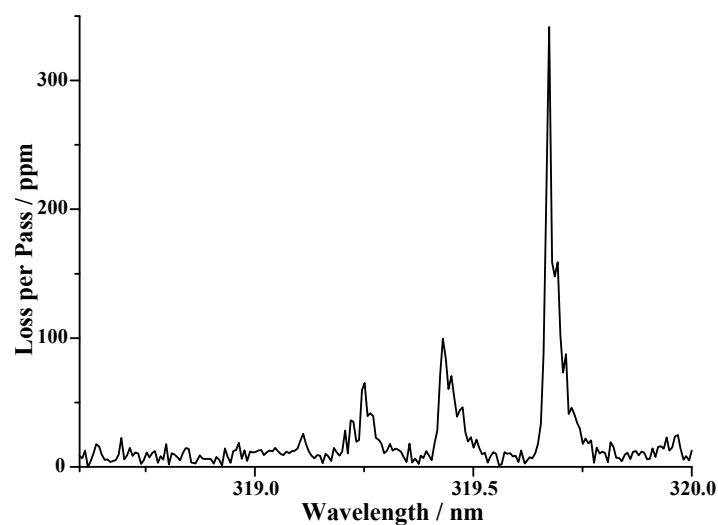
(b) Re-designed oven performance.

Figure 2.11: Absorption spectra obtained from the two different oven unit designs used to vapourise the solid sample. Both scans were carried out with an oven temperature of 135 °C

2.1.3 Laser System

The second harmonic of a Nd:YAG laser (Continuum, Surelite I-10, 10 Hz repetition rate) was used to pump a dye laser (Sirah, Cobra Stretch), with a second harmonic crystal (KDP) and Pellin-Broca wavelength separator installed. Two dyes were used in the laser in order to cover a scan range of 313-362.5 nm. DCM dye (in DMSO or methanol) was used to cover 313-342 nm while Pyridine 1 (in MeOH) was employed for 333.5-362.5 nm. The amplifier cuvette was only ran with methanol. In both cases only the oscillator and pre-amplifier beams were used for the frequency conversion. The power performance of the laser varied with the dye used, with the DCM producing $\approx$ 0.16 mJ at 320 nm and the Pyridine 1 yielding $\approx$ 90 μJ at 348 nm.
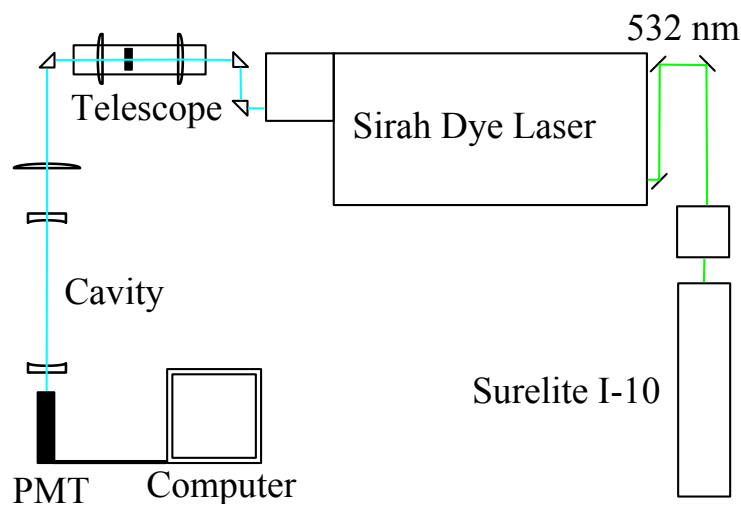
Figure 2.12: The experimental set-up.

The frequency conversion unit produced a second harmonic beam which was not well suited for optimum cavity ring-down. In an effort to increase the coupling of the laser beam into the cavity a telescope assembly was placed in the beam path. By employing the beam shaping optics the irregular laser beam from the frequency doubled dye laser could be more efficiently coupled into the TEM_{00} mode of the cavity. Prior to the placement of the telescope the approximate size of laser beam was first required. This was determined to be approximately 2 mm by 1.2 mm, with the polarisation of the laser light entering the cavity being horizontal.

2.1.4 Gaussian Beam Optics and the Cavity

For optimum cavity performance it is general practice to maximise the TEM_{00} mode and minimise any others. This is necessary as higher order transverse modes may

have different decay rates in the cavity and so lead to multi-exponential signals. In addition to the multi-exponential decays the presence of additional TEM modes can also result in mode beating, caused by the different cavity modes interfering with one another. This manifests itself as oscillations in the decay trace of the ring-down time. To minimise the higher order TEM excitations a strategy was developed by Lee *et el.*[66] using spatial filtering optics. Two convex lenses in a telescope arrangement are used with a pinhole placed between them. The set-up provided a means of shaping the pulse to form a more Gaussian profile (required for optimum TEM_{00} coupling). The shaped beam was then focussed into the centre of the ring-down cavity through the use of a convex lens for coupling into the TEM_{00} mode by matching the wavefront radii to the curvature of the entrance cavity mirror.

To couple the pulse into the cavity as efficiently as possible the spatial filter and mode matching lens required particular placement. Using the method described by Yariv[77] the position of the optics was calculated from the centre of the ring-down cavity, as used by S. Greaves.[70] Starting from the beam waist (ω_0) size,

$$\omega_0 = \left(\frac{\lambda z_0}{\pi \eta}\right)^{\frac{1}{2}} \tag{2.7}$$

where η is the refractive index of the cavity medium, λ the wavelength and z_0 is the characteristic length of the cavity, which is obtained through the relationship between the curvature of the mirror (r) and the cavity length (L).

$$z_0 = \sqrt{\left(\frac{(2r - L)L}{4}\right)} \tag{2.8}$$

Finally the beam spot size at the surface of the entrance mirror ($\omega_{l/2}$) can be found through the combination of (2.7) and (2.8), allowing the position to place the focussing lens to be calculated.

$$\omega_{\frac{1}{2}} = \omega_0 \left(1 + \left(\frac{L}{2z_0}\right)\right) \tag{2.9}$$

Through this placement of optics it was possible to increase the TEM_{00} component of the laser pulse entering the ring-down cavity.

The telescope assembly consisted of a plano-convex lens (focal length 200 mm), a 50 μm pinhole and a second plano-convex lens (focal length 50 mm). A final addition to the beam shaping set-up was the placement of a plano-convex mode matching lens (focal length 750 mm) before the first cavity mirror to act as a coupling lens into the cavity.

L

ω_0

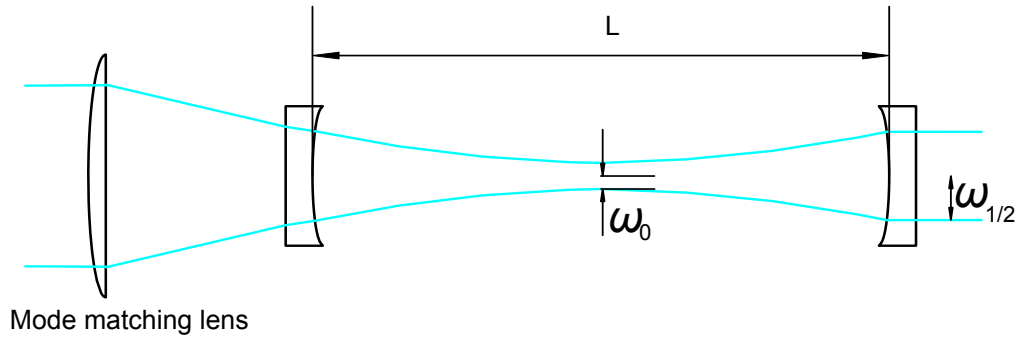$\omega_{1/2}$

Mode matching lens

Figure 2.13: Coupling of light into the optical cavity through the use of a mode matching lens.

The actual cavity ring-down portion of the experiment was carried out using 2 highly reflective mirrors (Layertec specification; plano-concave mirrors, diameter 12.7 mm, with 30 min wedge, $R = 1$ m, reflectivity $\geq 99.8\%$ at 330 nm) placed in Delrin mounts. The reflectivity was later found to be better than specified (99.86

2.1.5 Data Acquisition

The decaying laser pulse inside the cavity was detected using a PMT module (Hamamatsu, PMT, H7732-10) connected to a PC mounted digitiser card (National Instruments, NI PXI/PCI-5124, 12 bit). The computer was used to control the scanning laser and process the acquired signal from the PMT input channel. This laser control and data collection was carried out using a customised LabVIEW (National Instruments) program developed within the research group and based on a previous version from the University of Bristol.[78] For each laser shot the program acquires a baseline for subtraction from the laser pulse signal. This is taken before the laser enters the cavity and begins the ring-down event (Figure 2.14).

The program then fits a first order exponential curve to the trace, the decay constant of which is the inverse ring-down time. The residual of this first order exponential fit is displayed to aid the alignment of the laser. This allowed for optimisation of the decay signal by producing a visual display for assisting in identifying any mode beating or non-exponential decay in the signal. The cavity alignment could then be altered to minimise any none single exponential behaviour. The residual is then used to generate a value for the mean square error of the fit. The ring-down time and associated mean square error are then saved by the program along with the initial signal intensity at the start of the ring-down decay to record the shot-to-shot fluctuations in the laser pulse power.
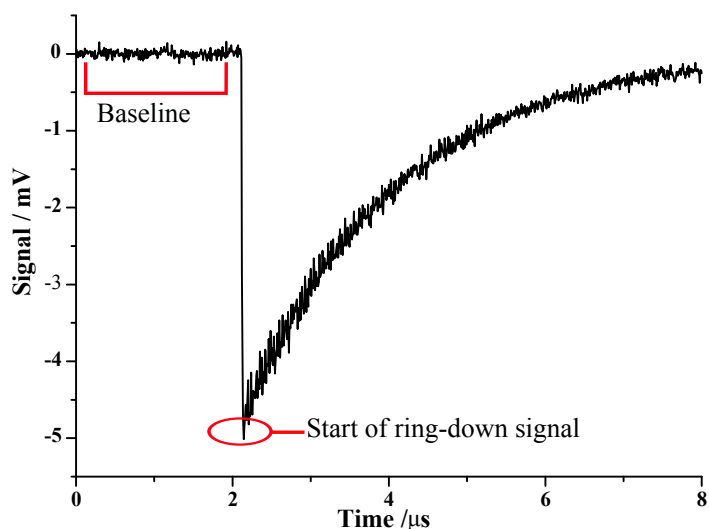
Figure 2.14: Decay trace displayed by the data analysis program.

When recording the spectra it was necessary to scan a background ring-down time value (τ_0). This was required because of the significant change in the mirror reflectivity over the scan range. By setting the nozzle fire time to just after the arrival of the laser pulse a blank scan, in similar pressure conditions to the optimised τ' could be achieved for the τ_0.

2.2 Screening of BPEB Derivatives

2.2.1 Early attempts

Table 2.2: Summary of the compounds analysed for use as potential candidates.

Molecule	Solution UV	TGA	Vapour UV
1	✓		
2	✓		
3	✓	> 180°C	Not obtained
4	✓		
5	✓		
6	Inaccessible		
7	Inaccessible	✓ 60°C	✓
8	✓	✓ 55°C	✓
9	✓	✓ 70°C	✓

A variety of compounds were trialled during the research as potential subjects for analysis (Figure 2.15). Each was screened using three different methods to assess their suitability.

Solution UV-spectrum A compound was dissolved in cyclohexane and analysed using a UV-spectrometer (Unicam UV/Vis spectrometer, UV4), with the solution made to a concentration yielding a peak absorbance of 1 on the spectrum. This
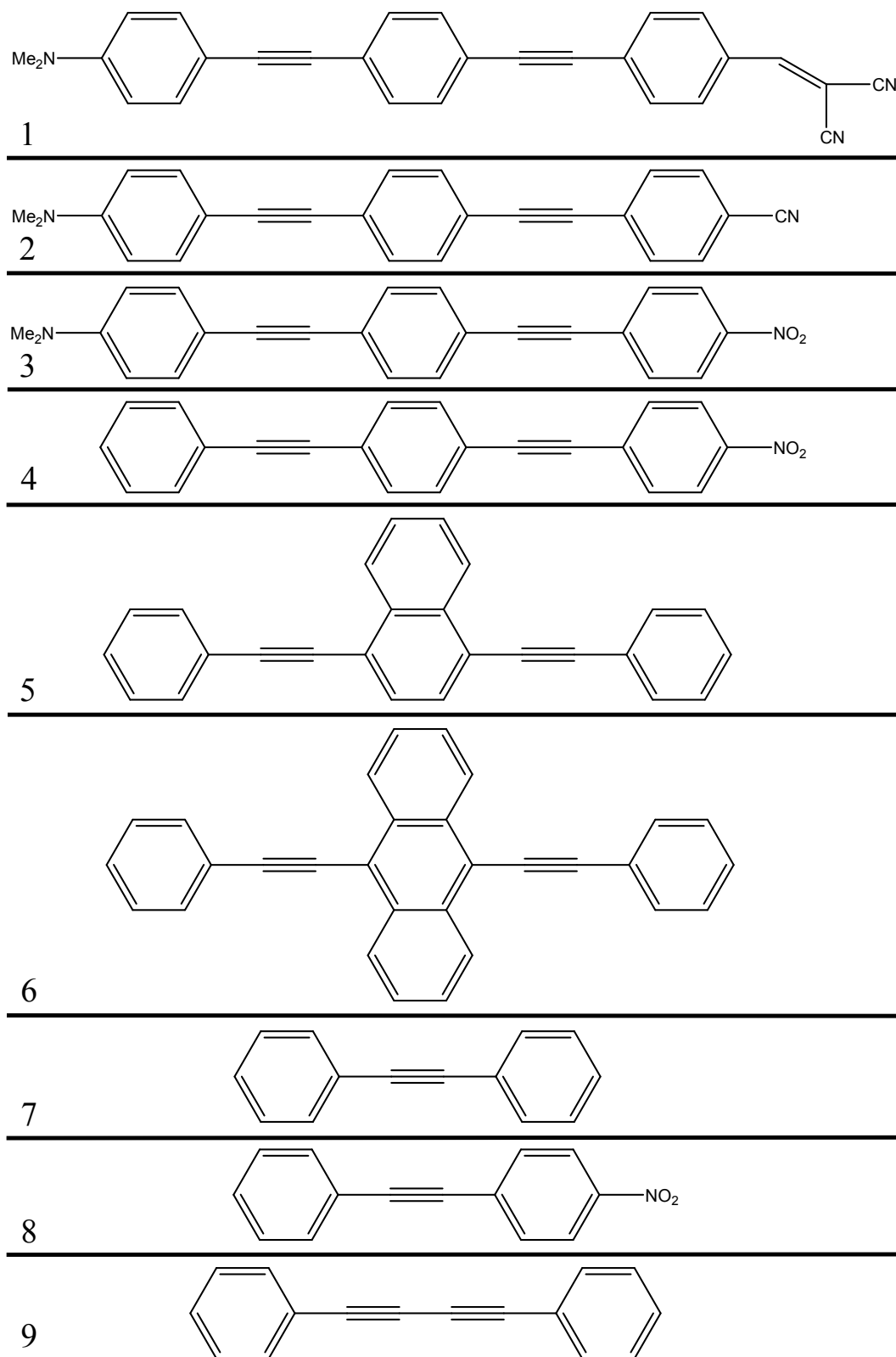
Figure 2.15: Molecules analysed for use in the experiment.

was done to assess if the compounds absorption range was suitable to the available range of cavity ring-down mirrors of 310-410 nm.

Thermogravimetric Analysis (TGA) Submitting the compound for TGA meant the vapourisation temperature of the sample could be determined. In doing so this would indicate if the compound was able to be safely vapourised within the operating limits of the General Valve nozzle assembly (180°C).

Vapour UV-Spectrum Once the vapourisation temperature of the compound was known the gaseous sample was then analysed in the UV-spectrometer. This was obtained by placing the solid sample in a glass cell with quartz windows at each end. This was sealed and then placed under vacuum using a diaphragm pump (Boc Edwards XDS 10c, 9.3 m^3 h^{-1}) with a flexible heater strip placed around the cell.

Analysis Comments

Compounds 1-3 The compounds did not dissolve in cyclohexane, even under heating. Dichloromethane (DCM) was used as the more polar character of the solvent could dissolve the compounds. The vapourisation temperature of all three of the compounds was found to be significantly higher than the safe operating temperature of the nozzle. This was attributed to the electron withdrawing/donating substituents forming strong dipole interactions in the solid. As a result of this high temperature of vapourisation the compounds were incompatible with the experiment.

Figure 2.16: The potential compound (1-dimethylamine, 2-ethynylphenyl), 4(1-ethynyl, 2-dicyanoethene phenyl)benzene (1) UV-spectrum taken in DCM.

Compound 4 This compound was synthesised *via* the Sonogashira cross-coupling reaction using an established method under the supervision of P. Low.[19] A compound with a single electron withdrawing/donating group was trialled to see i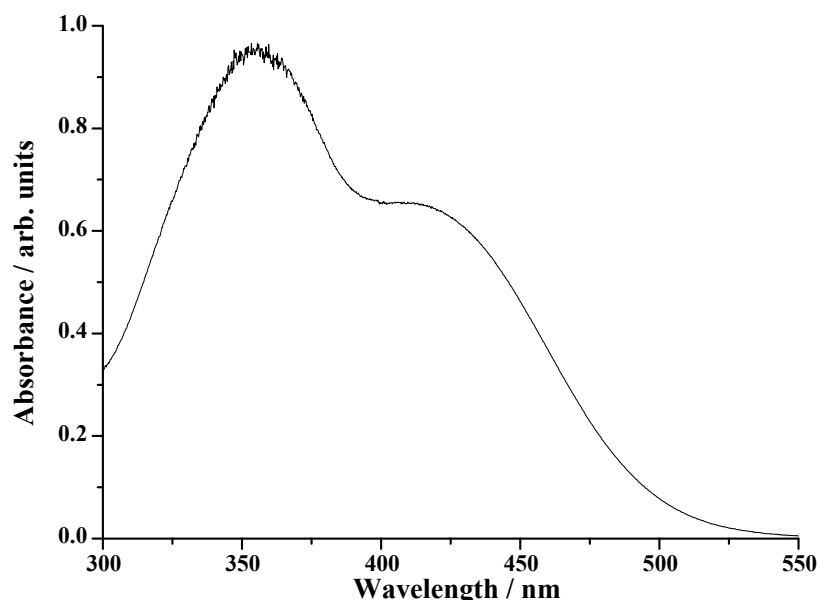f the single substitution would grant a more favourable vapourisation temperature by reducing the dipole in the molecule. This compound was shown to be less stable during TGA as the mass reduced by approximately 30% at 180°C. Following further analysis it was found that after this initial reduction the remaining compound mass was stable in excess of 300°C, meaning this too was unsuitable.
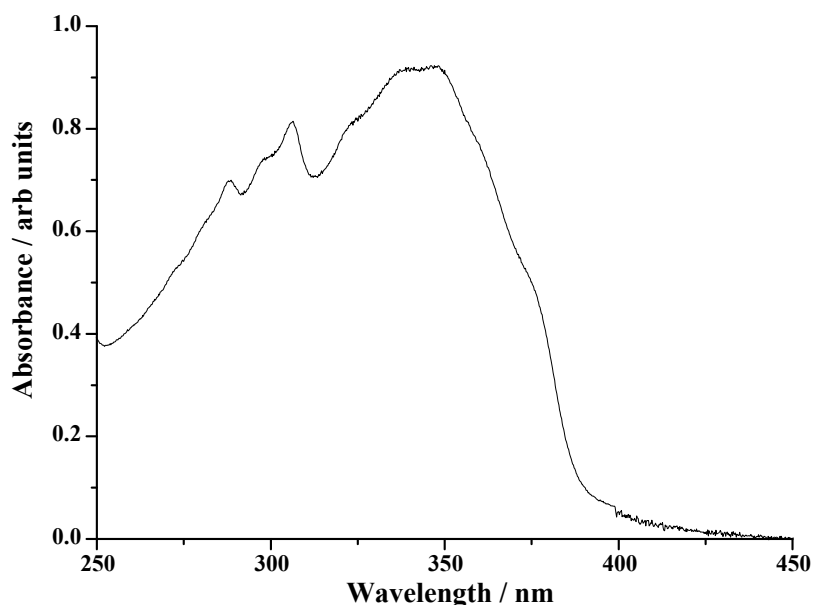
Figure 2.17: The monosubstituted polyaromatic 1(1-nitro,4-ethynylphenyl), 4(phenylethynyl)benzene (4) UV-spectrum taken in cyclohexane.

Compounds 5 and 6 Since the presence of electron withdrawing/donating groups resulted in vapourisation temperatures in excess of safe nozzle operating limits trials were carried out on compounds which displayed different phenyl ring configurations. Both the naphthalene (5) and anthracene (6) displayed vapourisation temperatures too high for use with the nozzle.

Compounds 7-9 With the problem of high vapourisation temperature encountered with the BPEB type systems a move was made to analyse compounds of two ring structures. The initial target of tolane (diphenylacetylene) was incompatible as the accessible wavelength range of the cavity ring-down mirrors did not cover the tolane absorption spectra.[79] The remaining compounds (8) and (9) were revealed to both be promising candidates, with accessible absorption spectra, safe vapourisation temperature and a successful gas phase spectrum acquired in the UV-spectrometer.

During the previous work carried out by S. Greaves on BPEB it was found that even a non-polar solvent such as cyclohexane induced a solvent shift on the compound
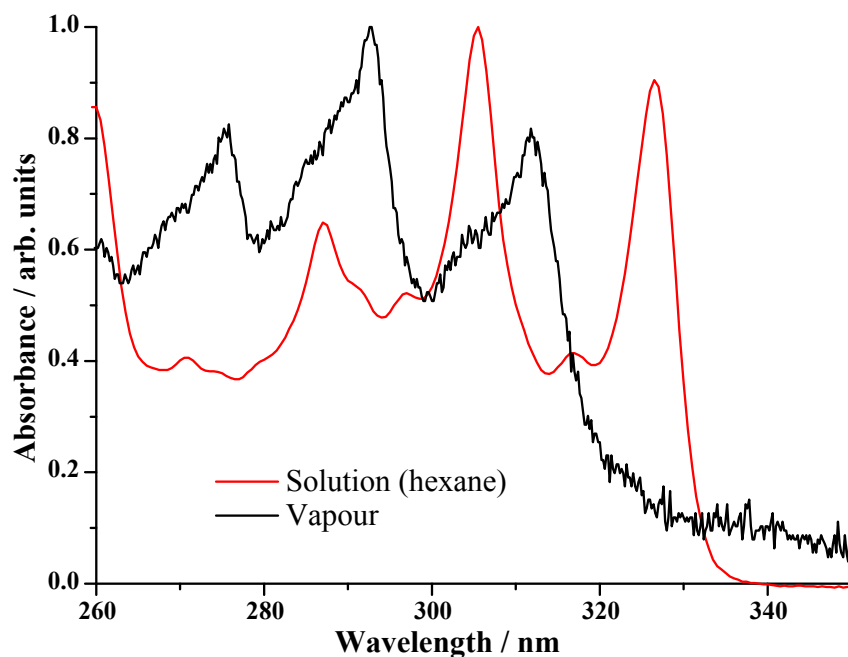
Figure 2.18: 1, 4-diphenylbutadiyne (9) UV spectrum carried out in cyclohexane and its vapour phase counterpart. Both scans have been normalised to 1.

when compared to the vapour spectrum. A similar effect was found to occur in both of the new sample compound, with the solvent producing a shifting effect on the compound UV spectrum to longer wavelengths.

Since the TGA had been carried out at atmospheric pressure the performance of heating the samples under vacuum was then investigated. To do so the sample was loaded into the M6 sample screw and weighed before being screwed into the oven. This was then mounted into the chamber and heated using a flexible heating strip. The oven was heated in steps of 10°C and allowed to remain at the set temperature for 20 minutes. After each heating increment the chamber was then slowly repressurised and the sample screw weighed. This was repeated (each time increasing the temperature by one increment) until the screw displayed a reduction in mass. The temperature was then noted as the approximate time the sample began to vapourise. Further heating was then carried out to ascertain the limit of the samples heating before the screw became completely empty.

Unfortunately, even with a favourable spectrum and vapourisation temperature, scanning for a reduction in ring-down time signal did not yield any results with either potential molecular candidate. A significant problem encountered was the timing of the molecular beam pulse relative to the ring-down event within the cavity. It was also found that the samples would sublime and exit the screw over a relatively narrow temperature range (70-88 °C for 1,4-diphenylbutadiyne). It was decided that

in order to overcome the narrow temperature range a technique was required which was more sensitive than CRDS, to enable the detection of lower concentrations of sample molecules. With the successful location of a feature within the selected range it would then be possible to move the laser to the features wavelength when using CRDS and so optimise the nozzle timing to detect the sample in the molecular beam.

Chapter 3

Incorporation of Laser Induced Fluorescence

3.1 Why Laser-Induced Fluorescence?

After the analysis of a wide variety of possible sample candidates, and the eventual selection of two which displayed the necessary characteristics, the problem of successfully overlapping the nozzle's gas pulse fire time with the ringing laser pulse was encountered. Coupled with this was the problem of narrow temperature ranges over which the samples would sublime before completely vapourising and leaving the sample screw empty and not knowing at what wavelength the compounds would absorb at when cooled.

Taking into account costs and time restraints Laser-induced Fluorescence (LIF) was incorporated as this technique potentially has a far better sensitivity than CRDS. LIF is essentially a background free technique as it detects the emission of photons from the sample molecules. For the experiment it could aid in the detection of any molecules in the beam as a detected photon would produce a signal which is more easily distinguished from a "zero" background value as opposed to a small ring-down time reduction as in CRDS. By incorporating LIF into the chamber the detection of any sample species should be possible at lower number densities compared to CRDS. This would prolong the duration of time a sample screw would contain a compound in the chamber and thus avoid frequent recharging of the sample.

The method to be employed would be to use the LIF as a means to detect any transitions which may be indiscernible in a ring-down spectrums noise level. Once a wavelength which generates a fluorescent signal (and so indicates an absorption at that wavelength) is identified the signal can be optimised and probed using CRDS

to generate an absorption spectrum.

3.2 Laser-Induced Fluorescence

Luminescence is based around the emission of light from matter following electronic promotion from the ground state to an excited state, and the subsequent return to a lower lying state with the expulsion of the excess energy as a photon. Luminescence itself can be divided into two categories, fluorescence and phosphorescence. The early scientific acknowledgement of fluorescence was around the middle of the 19th century, where it was found that quinine appeared to glow after exposure to sunlight.[80–83] As the understanding of fluorescence has improved and chemical theory evolved to better describe its process, the methods used to investigate the phenomenon have also developed in sophistication. From the early work carried out by Stokes, using sunlight and prisms, to current methods from an electrical discharge[84] to use of a laser (LIF) where through the use of monochromatic light it is possible to accurately excite specific transitions within molecules.[85]

As a technique, LIF exploits photoluminescence in molecules to produce spectra, with fluorescence occurring in all molecules. The absorption of a photon by a molecule occurs at a rate much faster than the nuclei can rearrange themselves to compensate for the electronic excitation, following the Franck-Condon principle. Besides fluorescence the molecule can then lose this excitation energy by various pathways (Figure 3.1) such as through collisions with other sample molecules or those of the solvent (in the case of solution phase measurements). These non-radiative means also include internal conversion (IC) and internal vibrational redistribution (IVR). During internal conversion the electronically excited state can revert back to the S_0 configuration, but with much greater vibrational energy (and hence populates higher vibrational levels in that state). IVR involves the redistribution of the excited state energy into other, accessible vibrational modes within the molecule to lower the energy. The removal of energy is more restricted in the gas phase (particularly in a molecular beam) as vibrational relaxation into solvent molecules is not possible. In the gas phase the only non-radiative pathways available are IC, intersystem crossing (ISC) into a triplet state and IVR, where even with these alternative energy pathways the internal energy of the molecule must be maintained as there is no way to remove it to other bodies, unlike in the solution phase. With this in mind the molecular excited state may survive for a sufficiently long time to undergo spontaneous emission of a photon. This release of energy does not necessarily correspond to the initial excitation transition between an excited state and a lower lying one. The excited state can return to almost any of the energy levels of the lower states,

providing it satisfies the Franck-Condon principle for the vertical transition down to one of the lower state's levels.
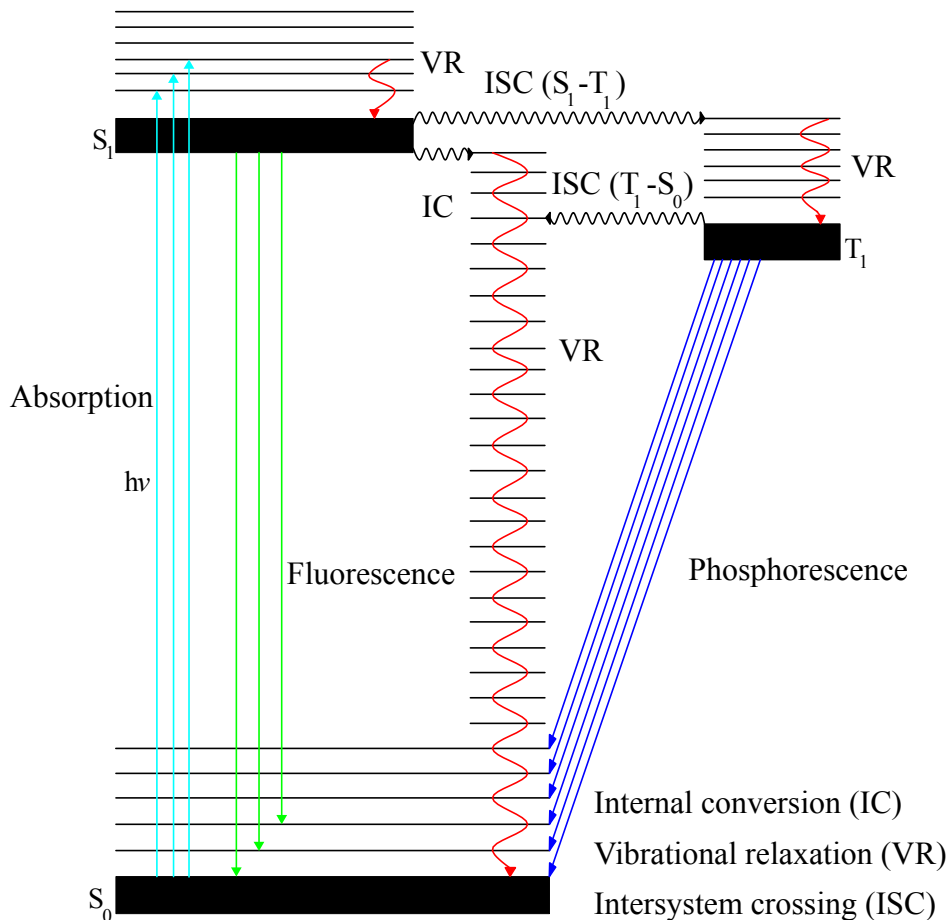
Figure 3.1: Jablonski diagram illustrating the various pathways available to a molecule to remove excess energy from an excited state. In the gas phase the molecule does not have the option of vibrational relaxation with solvent molecules.

The probability of an excited molecule making a transition to a lower lying vibrational level by spontaneous emission is related to the Einstein A coefficient.

$$A = \frac{8\pi h\nu^3}{c^3}B \tag{3.1}$$

in which h is the Planck constant, ν the laser frequency, c is the speed of light and B is the Einstein coefficient for stimulated absorption.

After time $\tau_i = 1/A_i$ (the fluorescence lifetime) the population of the excited state N_i has decayed to $1/e$ of its initial value at $t = 0$. τ represents the mean spontaneous lifetime of the molecule in its excited state. When undergoing spontaneous emission the molecule can relax to a variety of lower lying states with each of these relaxations governed by their own transition probability. As a result a single frequency exci-

tation can yield a variety of radiated frequencies, with a mixture of spectroscopic intensities. The method of dispersed fluorescence makes use of this principle by using a single excitation wavelength and separating the resulting fluorescence signal into its component frequencies.

The spectra obtained tend to be one of two main types: the previously mentioned dispersed fluorescence where a single exictation wavelength yields a variety of emission wavelengths, or a photoexcitation spectrum whereby the laser is scanned over a set wavelength range and the resulting fluorescence recorded. This second method can also make use of the dispersion technique and divide fluorescence from each wavelength into its component wavelengths or simply record the entire event as a single signal.

One key component of a fluorescence signal is the ratio of emitted photons in relation to the photons absorbed by the sample, known as the quantum yield (Φ_{F}). This parameter can indicate the aspects of a sample in relation to dynamics and structure in the excited state. It can be used to determine either the general yield of the entire system i.e. all emitted photons are counted as one transition regardless of origin, or, as in the case of dispersed fluorescence, each emitted wavelength will have an individual corresponding quantum yield.

$$\Phi_{\mathrm{F}} = \frac{\#\text{ fluorescence photons emitted}}{\#\text{ photons absorbed}} \tag{3.2}$$

The value of a system's yield is heavily influenced by the presence of other pathways within the molecule which can remove the excess energy through non-radiative channels. These alternative avenues for energy removal can involve vibrational redistribution of energy, quenching or internal conversion (Figure 3.1). The actual lifetime of the excited state before undergoing fluorescence varies from species to species and can range from ps,[30] ns[86] and μs.[87]

3.2.1 Incorporating LIF - Chamber Alterations

The changes required only minimal alterations to the chamber: removal of the cavity ring-down mirrors and their replacement with standard windows, a mount and focussing lens for collecting any emitted photons from the sample and finally an additional port for mounting of a PMT at 90° to the laser axis.

The remaining flange, at 90° to the laser axis, had a stainless steel frame mounted for placement of a plano-convex lens (Thorlabs, UV grade silica, focal length of 35 mm) below the copper oven exit orifice.
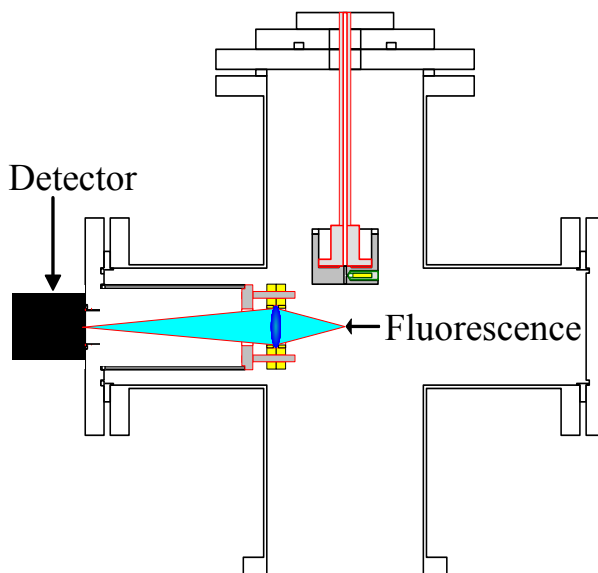
Figure 3.2: View down the laser axis of the chamber with the addition of the focussing lens mount.

The 35 mm focal length of the lens was selected via the thin lens approximation so that the object, in this case the probe volume of the laser pulse interacting with the molecular beam, distance from the lens surface would allow the projection of the image onto the PMT mounted on the flange.

$$\frac{1}{f} = \frac{1}{o} + \frac{1}{i} \tag{3.3}$$

where f is the focus length, o the object distance from lens and i the image distance from the lens. In addition to positioning the lens used in the collection of the emitted photons the mount was also designed to aid in reducing the effects of scattered laser light. By welding a plate onto a cylindrical length of piping the lens could be mounted in such a way as to effectively restrict the light which could be detected; only the light coming through the lens and mount would hit the detector (Figure 3.3). This plate also served as the base for the support of four threaded bars to secure the lens between two teflon mounts.

The placement of an adjustable iris between the PMT and filter allowed a degree of control over the portion of the beam's fluorescence which could reach the PMT surface. With the iris fully open the entire fluorescence signal could impact on the PMT cathode and produce a signal for the whole fluorescence source volume. By progressively closing the iris, however, the LIF signal would only come from the inner portions of the beam where we expect the cooler molecules to be located.

A filter (Semrock, 341 nm blocking edge BrightLine, long-pass filter) was also em-
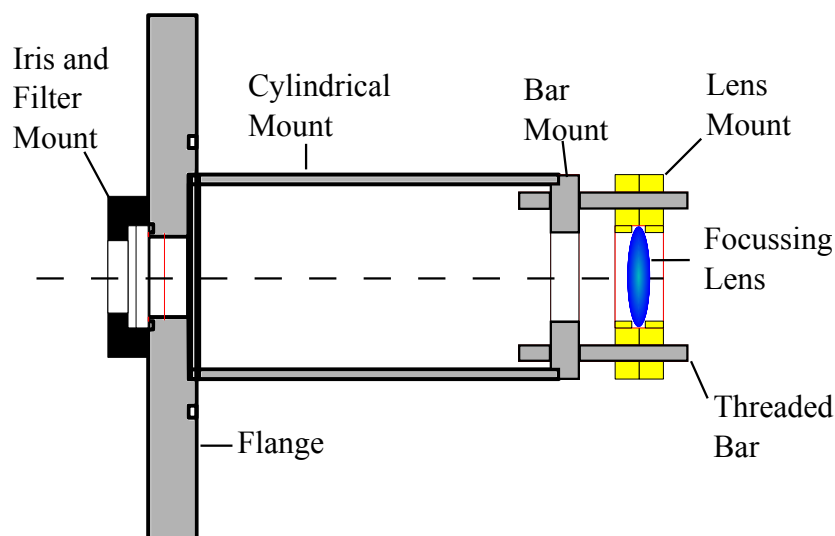
Figure 3.3: Design of the lens mount used for focussing molecular fluorescence in the chamber. The view is taken along the cylindrical axis.

ployed to minimise the effects of any scattered light. The filter removed light of wavelengths below $\approx$350 nm, with the solution phase fluorescence of BPEB indicating the emission wavelength could be in excess of 400 nm this was deemed an appropriate cut-off point for a filter.[31] Since the UV-spectra of the potential molecules indicated no absorbance above 350 nm the filter would be sufficient for the laser scans of the sample molecules.

With the installation of the LIF detection system the LabView software was adapted to measure the produced signal. A program based on that used for measuring the ring-down time was used in which the fitting the exponential decay signal was replaced with a portion of the program which integrated over a chosen data interval. The LIF signal was then normalised through the use of a pyrometer placed at the exit mirror/window. The laser power signal was fed into the LabView program where it could be used to scale the fluorescence signal detected by the PMT according to the power of the pulse.

3.2.2 Performance Test With SO_2

The LIF set-up was tested using a sample of SO_2 gas. With an absorption cross section of $\approx 4 \times 10^{-20}$ cm^2 around 320 nm the molecule was chosen to be a fair test of the set-up.[88] In addition it was also found that a fluorescence signal was produced over a range of wavelengths in excess of 350 nm, meaning the filter could still be employed.[89] The photoexcitation spectrum was recorded over a range of 319-320.4 nm (Figure 3.5). The spectra were obtained using a sample of SO_2 from the undergraduate teaching labs, with a pressure of $\approx$ 4 bar.
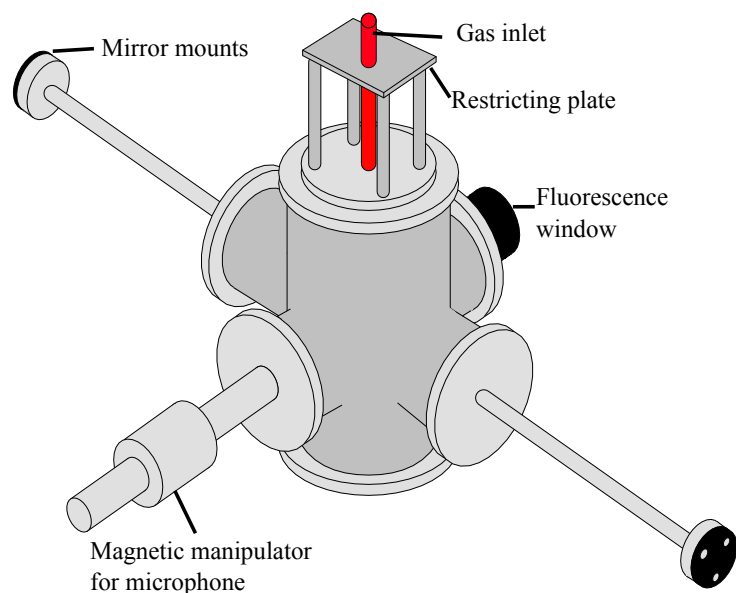
Figure 3.4: Vacuum chamber set-up with the microphone and fluorescence additions.
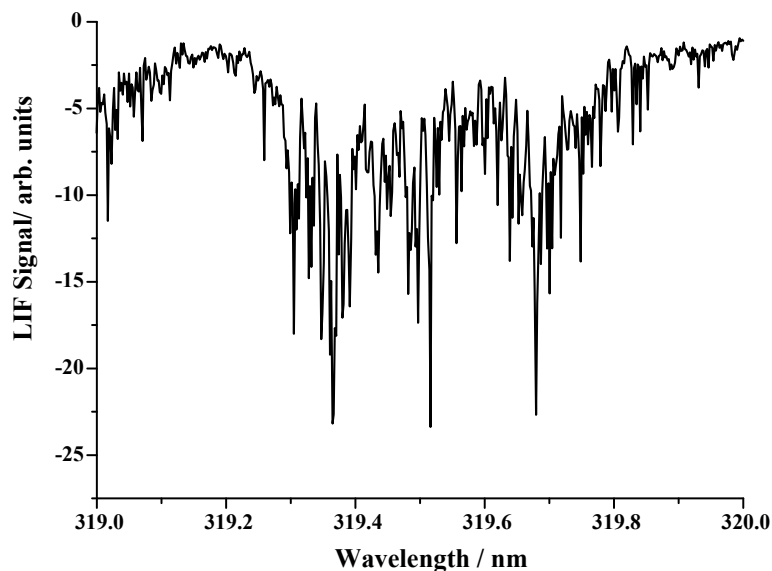
Figure 3.5: The initial LIF measurement obtained using pure SO_2 gas.

3.2.3 LIF of BPEB

With the SO_2 fluorescence measurement indicating the set-up was capable of detecting emitted photons we then progressed to using BPEB as a more relevant test molecule. The BPEB was chosen as the molecules to by analysed would have more in common with this molecule. Additionally the absorption profile was already known and so the laser could be moved to a known wavelength to test for fluorescence signal. Timing of the molecular beam pulse was optimised by first performing a measurement using the cavity ring-down set-up, then, having repressurised the

vacuum chamber, replacing the reflective mirrors with another set of mirrors that are transparent at the probe wavelength, i.e. effectively using "wrong" ring-down mirrors as windows.

The laser was tuned to the wavelength of the maximum absorption (≈ 319.68 nm) and the sample reheated until a change in signal was observed in the LIF PMT. Once a change was detected the laser wavelength was scanned over a 3 nm range to obtain a spectrum. These early scans did yield spectra which displayed definite signal corresponding to those showing absorption on the ring-down time scan (Figure 3.6). The problem, however, was that these results were obtained around the same temperatures as the CRDS ($\approx 130°$C), not producing the increased sensitivity that had been hoped for.
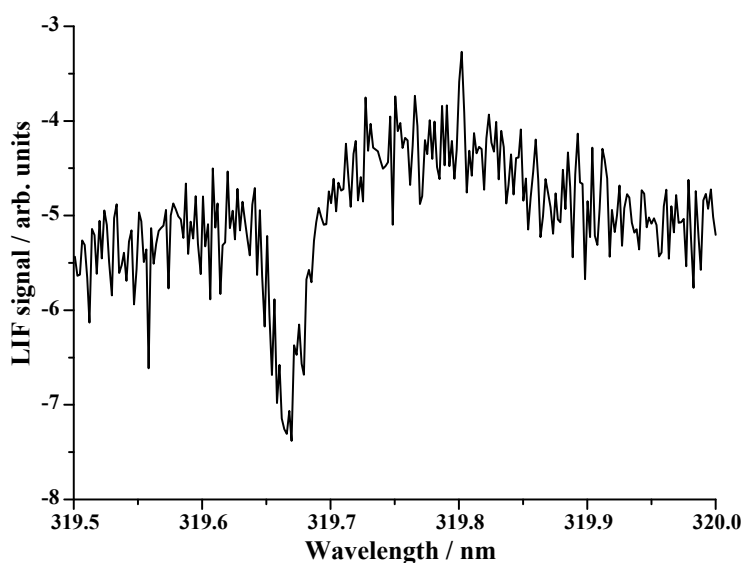
Figure 3.6: LIF spectrum of BPEB main absorption peak taken at 130°C .

The reason for the poor performance lies in the fact that the fluorescence lifetime of BPEB is <1 ns.[30] This raised concerns regarding the limits of the instrumentation used in the data acquisition, namely the performance of the digitisation card (number of points to digitise over) and PMT module response time. The difficulty came with distinguishing any fluorescence signal (Figure 3.7) from scattered light from the 5 ns laser pulse. It was decided to press ahead with the trial runs, but with a severely restricted data range to perform the acquisition over.
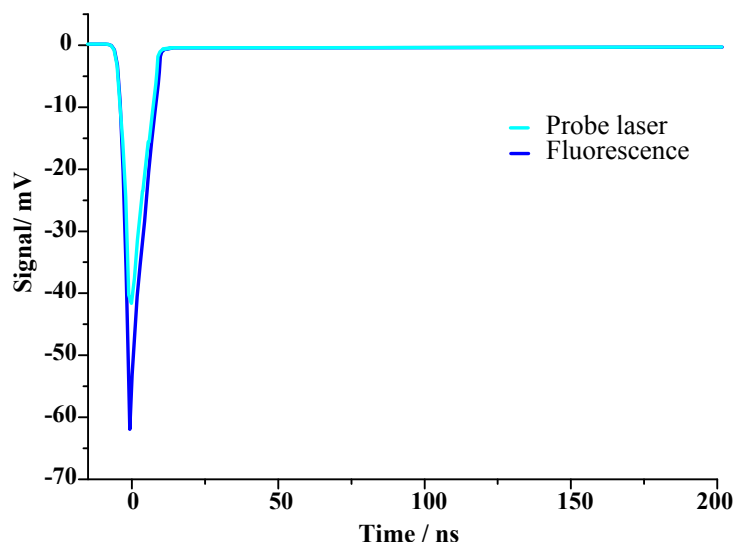
(a) Fluorescence lifetime which is difficult to distinguish from the probe laser pulse length, as in BPEB.
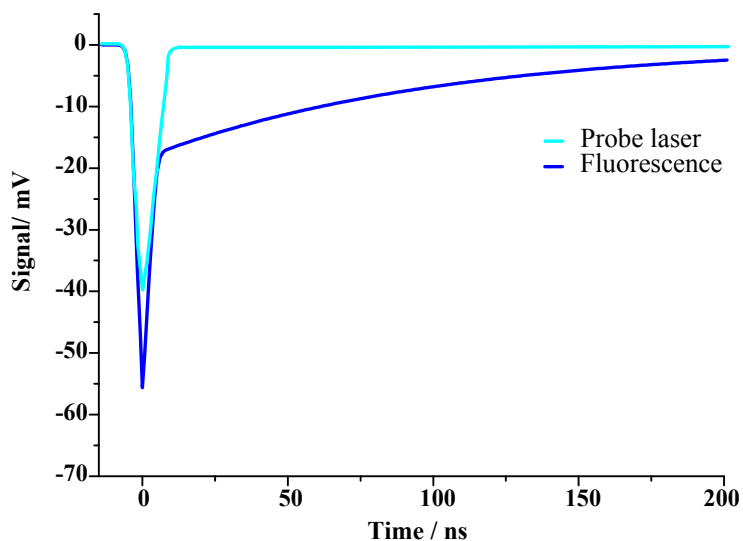
(b) A fluorescence lifetime in excess of the probe laser pulse length. This longer fluorescence signal is simple to distinguish from the scattered laser light, as in SO_2.

Figure 3.7: Illustration of the difficulty in distinguishing fluorescence signal from the initial laser pulse. The fluorescence does result in increased signal intensity so the occurrence of fluorescence can be verified.

3.3 Cavity-Enhanced Laser-Induced Fluorescence (CeLIF)

With the poorer than expected performance of the LIF system the chamber was then returned to the original CRDS configuration, whilst retaining the LIF set-up. The retention of the cavity meant that only a small portion of the light $(1 - R)$ of the incident laser pulse could enter the chamber. With the sensitivity of the PMT module allowing detection of individual photons it was thought possible for

the small amount of laser intensity to generate a sufficient LIF signal.

To our surprise the fluorescence spectrum obtained was a significant improvement on both the CRDS and the LIF spectra individually (Figure 3.8).
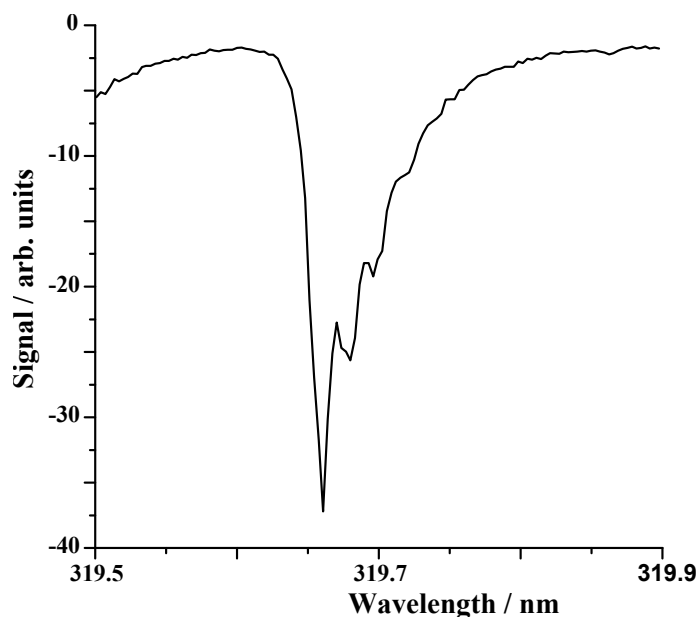
Figure 3.8: LIF of BPEB from the main absorption peak (319.68 nm) taken at an oven temperature of 140°C, using the cavity.

3.3.1 CeLIF Data Aquisition

In addition to extracting and recording data concerning the ring-down time, the original CRDS LabView program was also modified to record simultaneous LIF signals. Since each round trip of the ring-down event yields a voltage signal, as part of the ring-down transient, the effective number of photons in the cavity can be determined by calculating the area under the ring-down signal curve. The value for the area of the ring-down curve could then be used to normalise the signal received from the LIF PMT (see Section 3.3.3). To do so the program records the signal received from a second PMT unit and also calculates the area of the ring-down decay over a predetermined number of data points. The area selected for integration was over the same data point range used to determine the ring-down time. This ensures the value for the LIF is proportional to the laser intensity delivered into the chamber with each laser shot. In this sense the technique is self calibrating, and removes the need to monitor the power of the laser for LIF calibration.

3.3.2 Investigation of CeLIF

To gain a better understanding of the phenomenon which produced such striking results it is beneficial to focus on the processes occurring within the cavity. By separating out the set-up into discrete portions (Figure 3.9) it can be seen that the effective laser intensity inside the cavity eventually reaches approximately the value of the incident pulse (Table 3.1). Sectioning the apparatus into three portions allowed the determination of the light leaving the cavity (through the mirrors) and the power of the confined pulse.
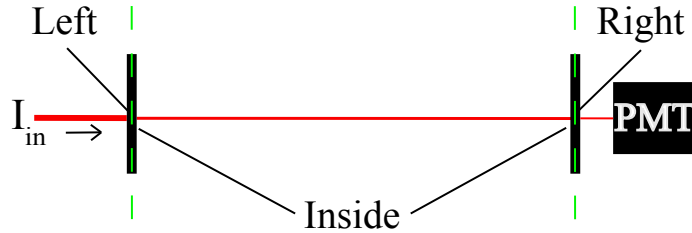
Figure 3.9: The partitioned experimental set-up.

The light intensity, I_{in} (number of photons), is incident upon the entrance (Left) mirror (Figure 3.9). Of this light $T \leq 1 - R$ is the fraction of the initial intensity which enters the cavity ($I_{\mathrm{in}}T$). The photons are then subject to any cavity mode properties between the entrance and exit mirrors ($\mathcal{M}$). If the cavity length allows the formation of a standing wave the mode effects on the photons will follow the cavity finesse ($\mathcal{F}$), as described in Section 1.5.3, to reduce the photon density by $\mathcal{M} = 1/\mathcal{F}$. When the cavity length does not permit the formation of the standing wave the $\mathcal{F}$ factor does not contribute to the number of photons in the cavity. This is then incident upon the exit (Right) mirror, where $I_{\mathrm{in}}TR$ is reflected back and $I_{\mathrm{in}}T^2$ exits the cavity. The intensity inside, and leaving, the cavity during each single trip is summerised in Table 3.1. Assuming no absorbing species is present in the cavity the effective number of photons in the cavity is approximately that of the initial laser pulse (corrected for any cavity mode influences). In the table T is the transmittance of the mirror, which is the proportion of light which travels through the mirror. From a first approximation this can be defined as $(1 - R)$, where R is the mirror reflectivity, but will actually have a value less than this as other losses to the photon number occur such as scattering and absorption by the mirror coating.

Table 3.1: The initial stages of a laser pulse entering the cavity between the two highly reflective mirrors. The arrows indicate the direction of beam propagation, R is the mirror reflectivity, T is the mirror transmittance $(1 - R)$ and I_{in} is the initial laser intensity confined within the cavity.

Trip	Left	Inside Cavity	Right
0		$I_{in}\mathcal{M}TR^0 \Rightarrow$	$I_{in}\mathcal{M}T^2R^0$
1	$I_{in}\mathcal{M}T^2R^1$	$\Leftarrow I_{in}\mathcal{M}TR^1$	
2		$I_{in}\mathcal{M}TR^2 \Rightarrow$	$I_{in}\mathcal{M}T^2R^2$
3	$I_{in}\mathcal{M}T^2R^3$	$\Leftarrow I_{in}\mathcal{M}TR^3$	
4		$I_{in}\mathcal{M}TR^4 \Rightarrow$	$I_{in}\mathcal{M}T^2R^4$
$\vdots$	$\vdots$	$\vdots$	$\vdots$
n even	$\frac{I_{in}\mathcal{M}T^2}{R}R^n$	$I_{in}\mathcal{M}TR^n$	$I_{in}\mathcal{M}T^2R^n$

Once in the cavity, the laser pulse remains confined until it has completely decayed, changing power by R^n after n trips. The reflection of the photons within the cavity means those which are not lost through transmittance, or other losses, have a chance to be "recycled" and begin the process again.

Using the geometric expansion

$$\sum_{i=0}^{n-1} R^i = \frac{1 - R^n}{1 - R} \text{with} \lim_{n \to \inf} R^n = 0 \tag{3.4}$$

gives the result that the effective light intensity inside the cavity which interacts with the sample during the course of the ring-down event. This can be seen to be approximately that of the initial laser pulse, corrected for any mode effects.

$$\lim_{n \to \infty} I_{in}\mathcal{M}T \sum_{i=0}^{n-1} R^i = \frac{I_{in}\mathcal{M}T}{1 - R} \simeq \frac{I_{in}\mathcal{M}(1 - R)}{1 - R} = \mathcal{M}I_{in} \tag{3.5}$$

In addition to the confined laser pulse interacting within the sample volume it is also important to determine the loss through each mirror. Using a geometric expansion on the result of the left mirror we see

$$\lim_{n \to \infty} \frac{I_{in}\mathcal{M}T^2}{R} \left[\sum_{i=0}^{n-1} R^{2i} - 1 \right] = \frac{I_{in}\mathcal{M}T^2}{R} \left[\frac{1}{(1 - R)(1 + R)} - 1 \right]$$

where the -1 compensates for the initial pass of the laser pulse through the sample area before beginning its reflections between the mirrors.

Upon expansion of the $1 - R^2$ component from the -1 the system then becomes

$$\frac{I_{\text{in}}\mathcal{M}T^2}{R}\left[\frac{1 - 1 + R^2}{(1 - R)(1 + R)}\right] = \frac{I_{\text{in}}\mathcal{M}T^2}{R}\left[\frac{R^2}{(1 - R)(1 + R)}\right]$$

Finally the relationship produces

$$\frac{I_{\text{in}}\mathcal{M}T^2 R}{(1 - R)(1 + R)}$$

With the assumption $R \approx 1$ we produce

$$\frac{I_{\text{in}}\mathcal{M}T^2}{2(1 - R)} \tag{3.6}$$

The mirror on the right of the cavity has a simpler description when assuming $R \approx 1$:

$$I_{\text{in}}\mathcal{M}T^2 \sum_{i=0}^{n-1} R^{2i} = \frac{I_{\text{in}}\mathcal{M}T^2}{2(1 - R)} \tag{3.7}$$

These results become very important when considering how to normalise the LIF signal produced by the laser pulse. Since each end of the cavity leaks approximately equal amounts of laser intensity (getting closer to an equivalent amount as $R \to 1$) it allows the successful determination of the effective number of photons within the cavity.

In cavity ring-down the lengthening of the pathlength, and hence laser pulse duration, leads to an enhancement in sensitivity to transitions which are normally too weak to observe.[61] A similar process may occur with the fluorescence signal in the cavity as the beam makes multiple passes through the sample, coupled with the fast rate of fluorescence and reasonable quantum yield ($\Phi_{\text{F}} = 0.56$)[30] of BPEB, generating a stream of fluorescence signal for detection.

Sample Signal

With the addition of an absorber to the cavity volume the reduction in I_0 is not only the result of loss through the mirrors, but also the absorption of photons by the sample, $I_0 T R^{n-1}(\alpha L)^n$, where αL represents the molecular absorption coefficient over the length of the absorber volume.

The absorption of the photons by the sample provides a pathway for fluorescence. To detect these emitted photons a focussing lens can be used to guide the emitted photons onto a PMT to generate a signal. Figure 3.11 illustrates the inclusion of

63
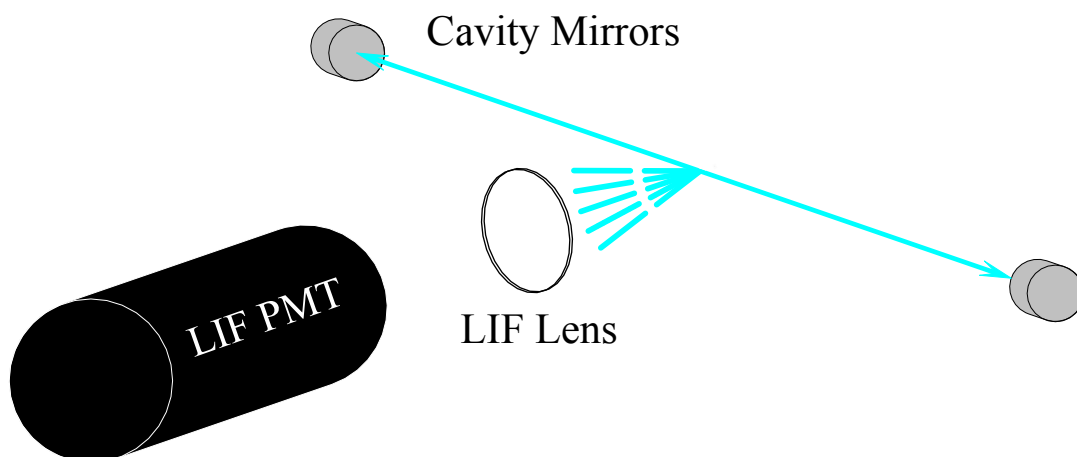
Figure 3.10: Schematic of combined LIF and CRDS set-up. The laser pulse that is coupled into the cavity passes repeatedly through the sample volume. With each pass a fluorescence or Rayleigh/Raman signal is produced.

a focussing lens to a ring-down cavity in order to collect the emitted photons from any fluorescing molecules in the laser probe volume.

In this case I_L represents the initial laser intensity I_0, the mirror transmission $T = (1 - R)$ and the correction factor for the mode effects of the cavity $\mathcal{M}$.

$$I_L = I_0 T \mathcal{M} \tag{3.8}$$

It can be seen that the lens does not cover the entire length of the cavity and so any fluorescing molecules outside the view of the lens will not contribute to any signal on the PMT. However, the area probed by the lens will see a reduction in the laser intensity by the time it reaches molecules which emit photons the lens can focus $(I_L(1 - [\alpha(L/2 - d/2)]))$. If the sample volume is smaller than the area viewed by the lens, such as in a molecular beam, the laser intensity will not be reduced and so the correction factor $= 1$.

In considering the two extreme cases of absorption volume a general treatment can be used for both instances. Figure 3.11 shows the initial stage of the laser pulse as it enters the cavity, through a mirror, where it must travel distance $(L/2 - d/2)$ before it reaches the area probed by the LIF lens mount. During this journey the laser intensity (I_L) will be reduced by $(1 - [\alpha(L/2 - d/2)])$ and as such the intensity of the fluorescence signal will be similarly affected. Once a fluorescence signal is detected it will have a value approximately equal to (1-αd), corrected for the $(1 - [\alpha(L/2 - d/2)])$ power reduction. Upon completion of the laser pulse moving across the length of the cavity the whole process will begin once again, with the addition of a (1-αL)

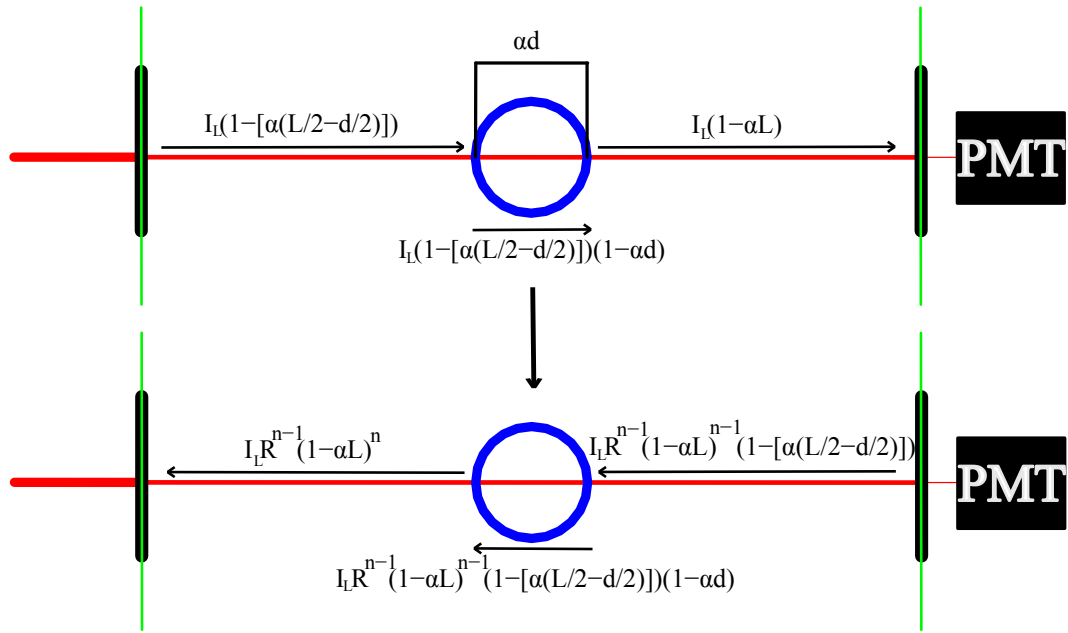Figure 3.11: The intensity of the laser pulse entering the cavity is I_L, R and $T = 1{-}R$ are the mirror reflectivity and transmission, respectively, L is the length of the sample inside the cavity, d the length of the LIF probe volume and α the molecular absorption coefficient.

correction factor as well as the $(1{-}[\alpha(L/2{-}d/2)])$. Table 3.2 describes the generation of a CeLIF signal using successive laser reflections. With each successive trip within the cavity the laser power is reduced by both the reflectivity (R) and the the $(1{-}\alpha L)$ component from the previous trip. The $[1{-}\alpha(L/2{-}d/2)]$ does not increase to power n with each trip as the overall power of pulse i is still $I_L R^i (1 - \alpha L)^i$, meaning that with each new trip the laser power needs to be corrected for the $[1 - \alpha(L/2 - d/2)]$ portion before the lens.

Table 3.2: The generation of the CeLIF signal from a confined laser pulse. The arrows indicate the direction of beam propagation, with $I_L = I_0 T \mathcal{M}$ and γ the correction for the laser power between the start of the laser round trip and the eventual start of the CeLIF signal $(1{-}[\alpha(L/2{-}d/2)])$.

Trip	Before CeLIF Signal	CeLIF Signal	After CeLIF Signal
1	$I_L\gamma$	$I_L\gamma(1 - \alpha d) \quad \Rightarrow$	$I_L(1 - \alpha L)$
2	$I_L\gamma R(1 - \alpha L)$	$\Leftarrow I_L\gamma R(1 - \alpha L)(1 - \alpha d)$	$I_L R(1 - \alpha L)^2$
3	$I_L\gamma R^2(1 - \alpha L)^2$	$I_L\gamma R^2(1 - \alpha L)^2(1 - \alpha d) \Rightarrow$	$I_L R^2(1 - \alpha L)^3$
4	$I_L\gamma R^3(1 - \alpha L)^3$	$\Leftarrow I_L\gamma R^3(1 - \alpha L)^3(1 - \alpha d)$	$I_L R^3(1 - \alpha L)^4$
5	$I_L\gamma R^4(1 - \alpha L)^4$	$I_L\gamma R^4(1 - \alpha L)^4(1 - \alpha d) \Rightarrow$	$I_L R^4(1 - \alpha L)^5$
6	$I_L\gamma R^5(1 - \alpha L)^5$	$\Leftarrow I_L\gamma R^5(1 - \alpha L)^5(1 - \alpha d)$	$I_L R^5(1 - \alpha L)^6$
$\vdots$	$\vdots$	$\vdots$	$\vdots$
		$I_L\gamma R^n(1 - \alpha L)^n(1 - \alpha d)$	

Each trip thus takes the form of Equation (3.9), as would occur in CRDS with the

presence of an absorber.

$$I_L R^n (1 - \alpha L)^n \qquad (3.9)$$

The actual CeLIF signal obtained with each pass of the laser beam follows Equation (3.10).

$$I_L R^n (1 - \alpha L)^n (1 - [\alpha(L/2 - d/2)])(1 - \alpha d) \qquad (3.10)$$

Treating this in a similar fashion to the result of the empty cavity yields

$$\lim_{n \to \infty} I_L \gamma (1 - \alpha d) \sum_{i=0}^{n-1} R^i (1 - \alpha L)^i$$

$$= I_L \gamma (1 - \alpha d) \frac{1 - [R^i(1 - \alpha L)^i]}{1 - [R(1 - \alpha L)]}$$

$$= \frac{I_L \gamma (1 - \alpha d)}{1 - [R(1 - \alpha L)]} \qquad (3.11)$$

This general treatment can be applied to both a cavity filled with the sample for detection and to a regime which has a more confined probe volume (molecular beam). The stated method can be used as reported for a cavity which is filled with sample gas, with the only adjustment for a molecular beam environment being that the $(1-[\alpha(L/2-d/2)])$ factor is no longer present. This removal is the result of the molecular beam width containing the absorber, therefore no photon absorption occurs prior to the laser beam entering the area probed by the LIF lens, meaning $(1 - \alpha L) = (1 - \alpha d)$. Should the probe volume be wider than the LIF lens, but not fill the entire cavity length, then the L factor will correct for this providing it is accurately known.

The corresponding change in ring-down time transient intensity can be described using a similar set of equations and assumptions. Since the PMT receives a signal every second laser trip (roundtrip) the equations are adjusted accordingly and $I_L^{\text{CRD}} = I_0 T^2 \mathcal{M}(1 - \alpha L)$

$$I_n^{\text{CRD}} = I_L^{CRD} \sum_{i=0}^{n/2} (1 - \alpha L)^{2i} R^{2i}$$

$$I_n^{\text{CRD}} = I_L^{CRD} \frac{1}{1 - [(1 - \alpha L)^2 R^2]}$$

Comparison of the integrated LIF and CRDS intensities yields

$$I^{\text{LIF}} = I^{CRD} \frac{[1 + (1 - \alpha L)R][\gamma(1 - \alpha d)]}{T(1 - \alpha L)}$$

In the limit of small loss, where $\alpha L \ll 1$ and additionally $R \approx 1$, I^{LIF} can be approximated as

$$I^{\text{LIF}} = I^{CRD}\frac{1+R}{T} \approx I^{CRD}\frac{2}{T}$$

3.3.3 Signal Normalisation

By monitoring the emitted photons from the BPEB sample seeded in the molecular beam it became apparent that the combination of CRDS and LIF had yielded a method of producing spectra which displayed a far superior signal-to-noise ratio and, after further testing, a much enhanced sensitivity to lower molecular densities. As in conventional, single-pass LIF (spLIF), to obtain a quantitative spectrum it was necessary to normalise the fluorescence measured with respect to the laser power shot-by-shot. For our spLIF measurements this was accomplished through the use of a pyrometer placed behind the exit window of the chamber.

Whilst the ring-down transient is used to determine the lifetime of the laser pulse within the cavity the intensity of the trace is proportional to the number of photons within the cavity $(I_0(1-R))$, at any given time. Thus, integrating the same area of ring-down trace as used in LIF provides a measure of the number of photons in the cavity which correspond to to the LIF intensity (Figure 3.12). The entire ring-down trace was not used to determine the ring-down time and photon number as we wanted to minimise the chances of recording data from a feature with a saturation signal, while the tail end of the ring-down trace was not used as this would generate more noise on the ring-down fit.

A feature of the experimental set-up was that very little stray light was detected across the fluorescence signal, even though no specialist adaptions (such as baffles or a filter) were in place to minimise this effect. In the experimental set-up the light is confined in the cavity. The beam shaping optics are used to couple the light into the cavity in such a a way as to maximise the light entering the TEM_{00} mode. Any stray light is initially filtered by the cavity entrance mirror, with any stray light which enters the cavity quickly scattering and dissipating. The length of time the laser pulse is confined in the cavity means the LIF signal can be integrated after any scattered light has dissipated.

As the ring-down event caused multiple passes through the sample, and consequently multiple bursts fluorescence signal, the CeLIF trace can be seen to follow the ring-down transient (Figure 3.13). With no heating of the sample oven no CeLIF signal is produced, with only an initial spike, attributed to scattering of light (note the high setting of the PMT), present on the trace (Trace A). As the temperature increases
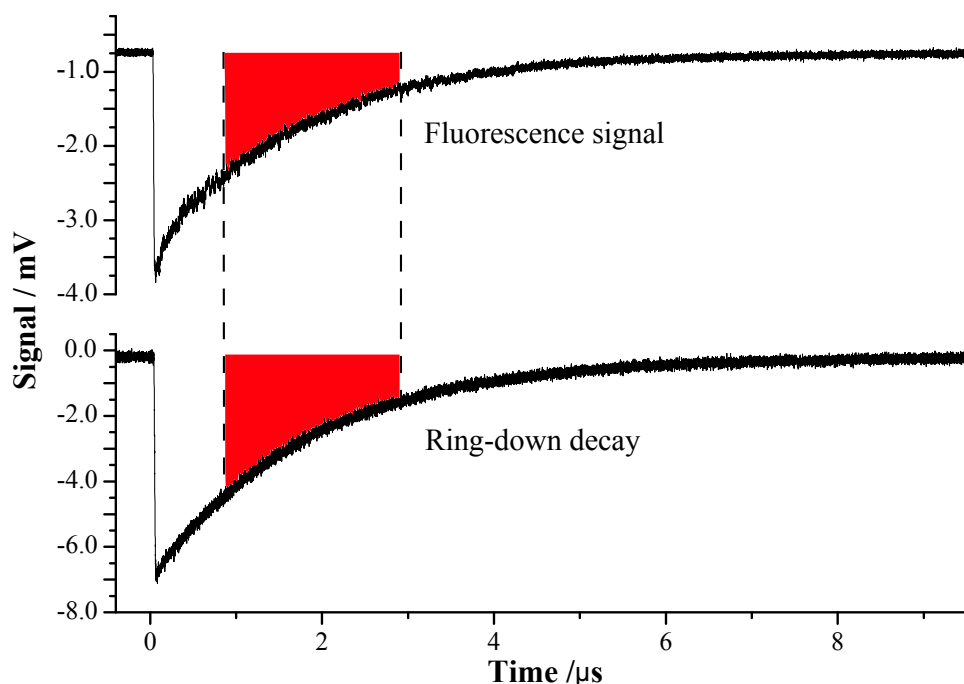
Figure 3.12: Illustration of the normalisation of the LIF signal using the corresponding area under the ring-down curve.

the CeLIF signal can be seen to emerge (Trace B). Even with this small CeLIF signal it was still possible to generate a useable spectrum as LIF detects a change from zero signal (background) and so can more easily distinguish signal from the baseline/background. In our particular case further heating of the oven resulted in sufficient number densities to yield a fluorescence trace which mimicked the ring-down transient (Trace C). This will not necessarily occur with all compounds, but the high molecular cross-section and fluorescence quantum yield of BPEB mean a large number of photons will be expelled to generate the LIF signal.

3.3.4 A Re-Visit to 1,4-diphenylbutadiyne (Compound 9)

With the successful implementation of the CeLIF set-up in the apparatus a new test molecule was selected to ensure the technique was viable on species other than those with extremely high absorption coefficients, such as BPEB. Since 1,4-diphenylbutadiyne (DPB) had already been identified as a possible candidate it was selected as a true test for CeLIF. The molecule was chosen as it displayed a sub-nanosecond fluorescence lifetime,[90] as seen in BPEB, and an approximate temperature profile was known from thermo-gravimetric analysis.

Investigations into the properties of 1,4-diphenylbutadiyne (DPB) have included the crystal structure,[91] photochemistry[92] and excited state studies.[93;94] The crystal structure study found the molecule possess a linear configuration, with the phenyl
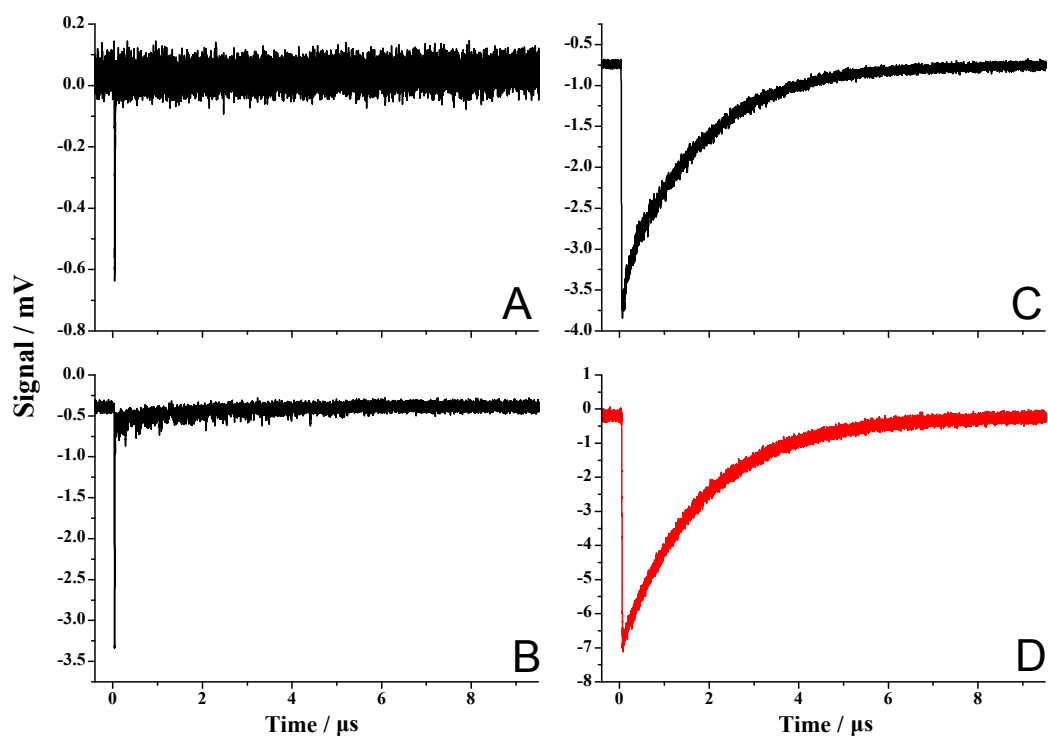
Figure 3.13: BPEB CeLIF transients obtained at different oven temperatures (number densities). A) CeLIF obtained with a pure Ar beam i.e. no sample, and with a higher PMT setting than the other transients. Panels B) (oven temp $\approx 90°$C) and C) (oven temp $145°$C) show the effect of increasing number density on the degree of CeLIF signal observed. D) (red) is the ring-down transient recorded simultaneously with the CeLIF in C), illustrating the CeLIF signal lasting the duration of the ring-down signal.

rings existing in a coplanar arrangement. Excited state studies have found this linear configuration appeared to be maintained in the lowest excited triplet state. The molecule has also been compared to polyarylethynyl molecules by Thomas *et al.* to ascertain the effect of the additional ethynyl bond between the two phenyl rings.[95] In this study Thomas found that the single bond joining to two ethynylaryl portions in DPB displayed characteristics more common in double bonds. Additionally the degree of conjugation was found to be less pronounced in DPB. The group concluded that the presence of the single bond between the two ethynylaryl groups was found to impose more restriction on the degree of conjugation possible throughout the molecule when compared to Tolane.

With the temperature profile of the sample known one of the main issues in producing a sample spectrum was minimised. However, whilst the vapourisation temperature was known the successful timing of the nozzle to intersect the molecular beam with the laser pulse was still a concern. During CeLIF analysis of BPEB it was found the molecule displayed a broad feature in addition to the main peaks identified. This

meant the molecule produced a fluorescence signal between the main peaks. It was hoped the DPB may display a similar characteristic and allow its identification in the molecular beam. If the molecule did not have a broad feature to generate a LIF signal it was also thought that the large number of aromatic electrons would be sufficiently polarisable to produce a small, detectable Rayleigh scattering signal. The DPB was analysed using the standard CeLIF experimental apparatus as with the BPEB. The sample was detected in the beam from an oven temperature of $\approx 74°C$ via Rayleigh scattering, although no useable spectrum was produced until the oven reached 80°C.
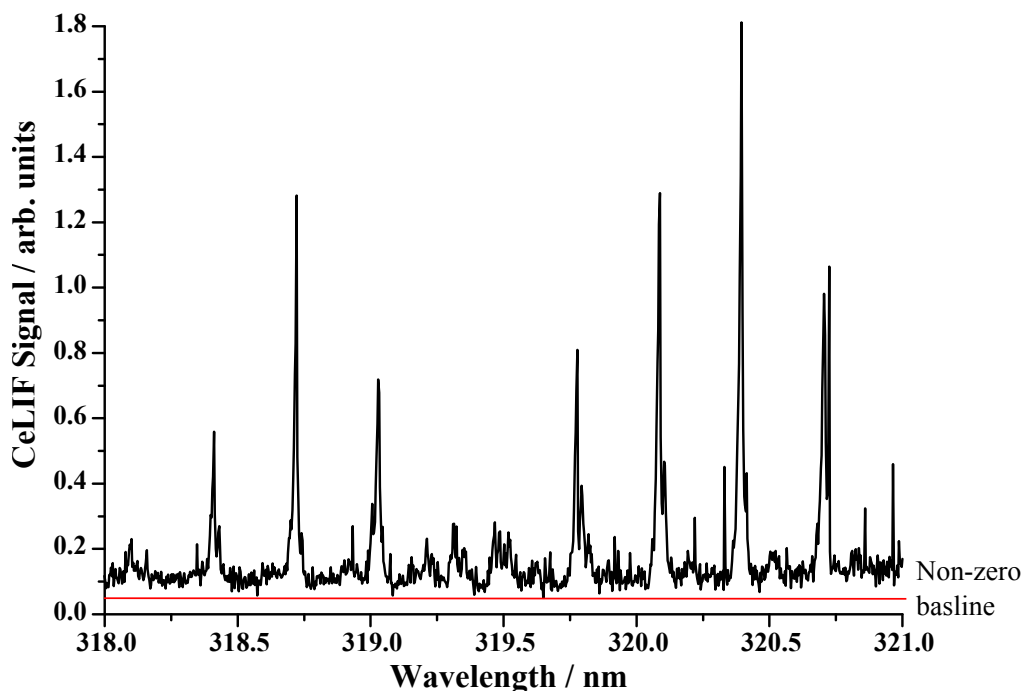
Figure 3.14: CeLIF spectrum of 1,4-diphenylbutadiyne taken at 84°C across the range 321-318 nm. The non-zero baseline, attributed to Rayleigh scattering, can clearly be seen. This made it possible to detect the sample molecules in the molecular beam.

Initial testing with a pure Ar beam indicated that the scatter caused was negligible and could not be distinguished from a chamber with no nozzle firing. The molecules analysed are much larger species than Ar and have delocalised π systems which can be distorted by the incoming electric field of the light and produce a much greater Rayleigh scattering signal. While not as powerful as the fluorescence signal, as stated previously the LIF has the advantage of working from an essentially zero background. Thus the small signal from the Rayleigh scatter could be detected and manifested itself in the spectra as causing the signal to have a non-zero baseline (Figure 3.14). This Rayleigh scattering signal could be removed with the addition of an appropriate filter, however, in this particular case it was more advantageous to perform the scans without a filter. With the location of the Rayleigh signal the

nozzle fire time could be optimised for laser scans and eventual peak location.

From qualitative comparisons between the CeLIF scans of the DPB with that of the BPEB it can be seen that the signal-to-noise ratio on the spectrum of the DPB is not as compelling as that obtained in the BPEB trial. In addition to this observation in the CeLIF spectrum it was also found that the CRDS recoded simultaneously did not produce a corresponding absorption spectrum. This lack of an absorption spectrum points towards the absorption coefficient (α) of the DPB sample being too low to allow its detection using the current CRDS set-up. The greater sensitivity of the LIF portion of the CeLIF was also crucially important as the DPB displayed a very narrow temperature range over which it could be detected (Section 2.2.1).

With the successful procurement of a CeLIF spectrum for DPB at attempt was made to analyse the data to determine the torsional energy of the molecule. This proved unsuccessful as the wavelength range the spectra were recorded over could not be simulated with any confidence. The mass of sample available for analysis in the chamber was quickly depleted and so longer scans were not possible.

3.3.5 Characterisation of CeLIF

To better assess the performance of CeLIF in relation to molecular beam measurements the technique was characterised using the established experimental set-up, with BPEB selected as the test molecule. Obtaining a spectrum at various oven temperatures (sample densities), allowed the CeLIF and CRD signals to be compared qualitatively and show the relative difference in sensitivity. This was accomplished by recording spectra at oven temperature intervals of 10°C from the temperature which first yielded a CeLIF signal. Each scan being carried out over a range of 321-319 nm with 36 laser shots per point.

From a qualitative standpoint the spectra produced from the CeLIF portion of the scans display a much greater degree of signal compared to the background value. The results from the CeLIF scans differ from those of the CRDS in the respect that the background level in the scans is significantly lower, allowing the emergence of any fluorescence signal to be seen much more easily. This could be seen even at the lowest temperature probed (75°C), which yielded a spectrum which was, qualitatively, very similar to the best spectrum obtained with CRDS. The baseline for CeLIF scans does increase with temperature, however, which is due to Rayleigh scattering increasing with the number density, resulting from the heating, in the beam.

A selection of the scans can be seen in Figure 3.15, where the qualitative enhance-

ment produced using CeLIF is compared to the simultaneously obtained ring-down measurements. As neither the molecular cross-section nor number density were accurately known for the gas phase BPEB the results were converted into a photon loss per pass (parts per million (ppm)) format. The ppm scaling of the CeLIF signal peaks was accomplished by equating the CeLIF peak in the best CRDS scan ($135°C$) and then taking a scaling factor between the two. This was consequently applied to the other CeLIF scans after they had been scaled to account for the different PMT settings used in their acquisition.
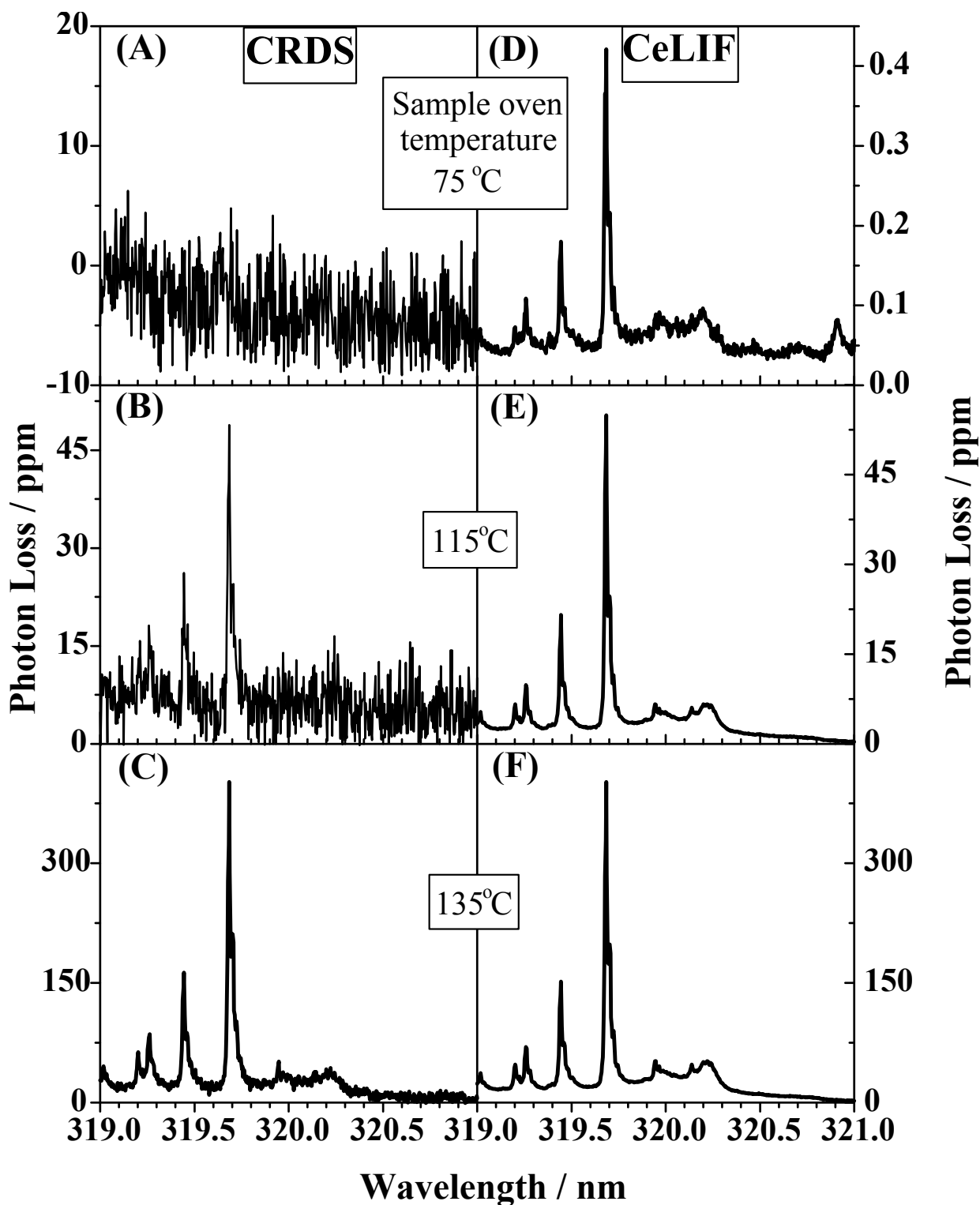
Figure 3.15: CeLIF and CRDS scans performed using BPEB at different temperatures (number densities). Spectra A), B) and C) are all CRDS absorption scans shown as photon loss per pass, while D), E) and F) are those obtained from CeLIF. The CeLIF scans have been normalised with the absorption loss per pass to display the enhanced sensitivity afforded by the technique.

Later tests with the CeLIF set-up even managed to produce a weak spectrum of

BPEB at 65°C (Figure 3.16). This further illustrated the enhanced sensitivity afforded by the CeLIF method.
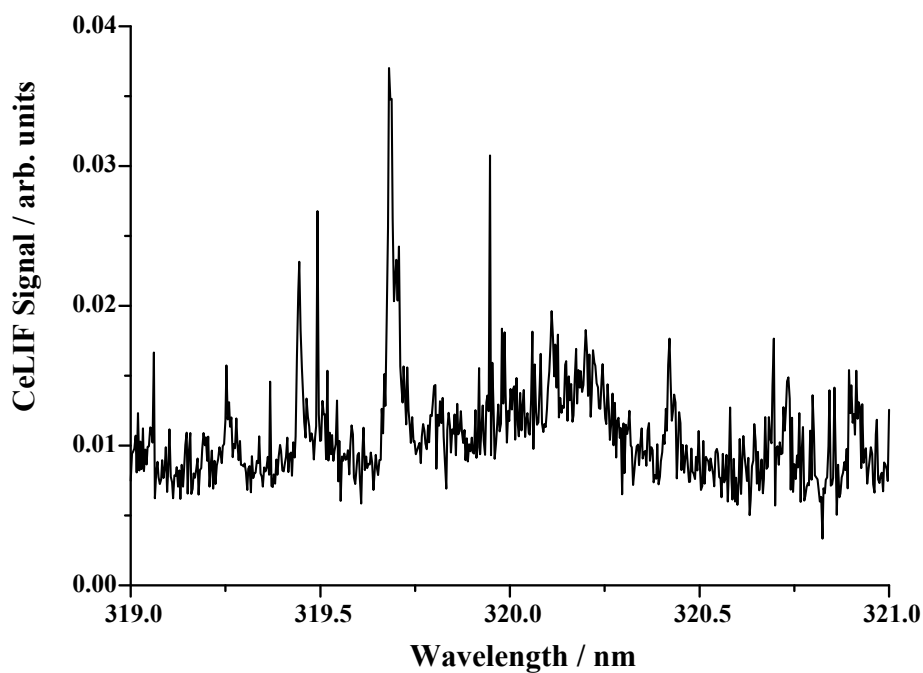
(a) CeLIF scan at an oven temperature of 65°C
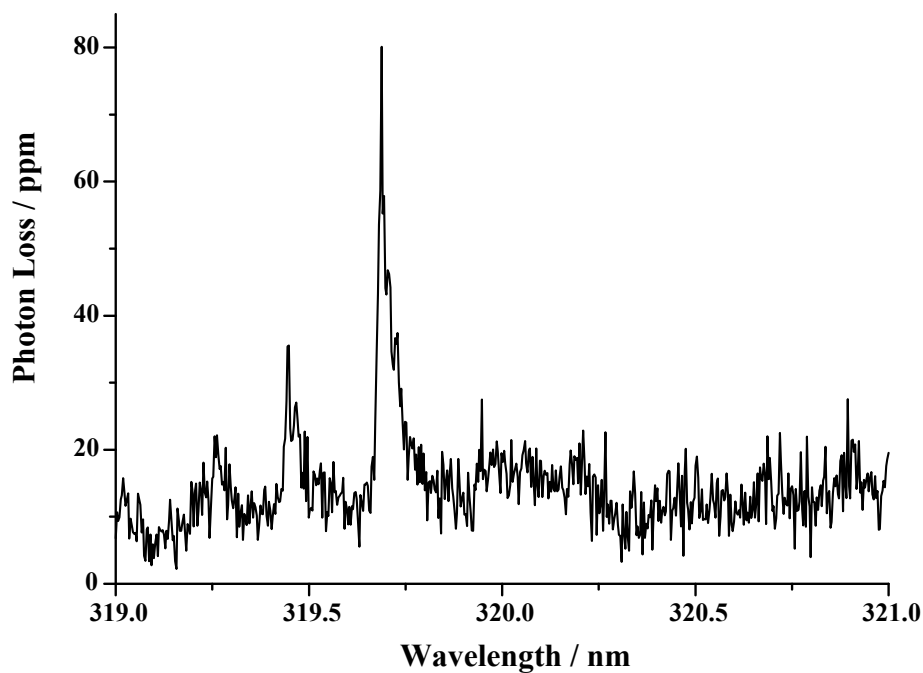
(b) Photon loss from CRDS scan at an oven temperature of 115°C

Figure 3.16: Comparison of the sensitivity between CeLIF and CRDS. PMT scaling factors were unavailable to properly scale the CeLIF into a ppm format.

Quantitative Comparison of the Simultaneous Measurements

In addition to a qualitative comparison between the two techniques the signal-to-noise (S/N) and signal-to-detection limit (S/DL) were also investigated. In this particular analysis the detection limit/sensitivity is with respect to a feature emerging three standard deviations (3σ) of the background level. The reported S/DL is thus a multiplication factor for the 3σ value, which corresponds to the signal intensity. This would be used as an indicator of the number density sensitivity of the two respective techniques (CeLIF and CRDS).
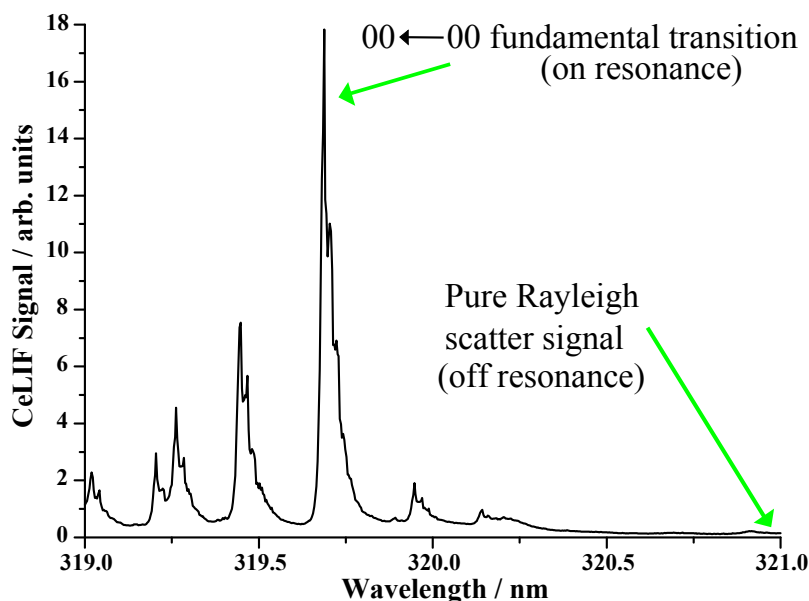
Figure 3.17: A CeLIF spectrum illustrating the two points used as a fluorescence signal measurement and the CeLIF background value (minimal Rayleigh scatter).

The collection of data for the S/N and S/DL analysis required the use of a customised LabView program, developed within the group by O. Willis, and different data collection hardware in the form a 125 MS/s, 14 bit Digitiser (PCI Express, model ATS9440). To determine the S/N and S/DL the CeLIF and CRDS signals were measured at two different points in the BPEB spectrum. Since the CeLIF inherently possessed a background signal from Rayleigh scattering an alternative was needed to extract a background measurement. Whilst the implementation of a filter would be the simplest solution the fluorescence frequencies emitted from the BPEB over the selected wavelength range were not known. Pure Rayleigh scattering signal was obtained by keeping the nozzle timed to produce signal, but moving the laser to a wavelength which yielded no fluorescence (320.8 nm), as can be seen in Figure 3.17. The Rayleigh scattering baseline was judged to be constant for our purposes over the scan as over such a short range the increase is negligible. The noise on the 320.8 nm signal could then be used as the background level which a fluorescence

signal would need to emerge 3σ from. The position selected to produce the signal measurements was 319.68 nm (the torsional motion fundamental transition). At each point the fluorescence was analysed over 2500 laser shots, with the signal traces also saved from both the CRDS and CeLIF components from the first 100 shots. These 2500 laser shots were used for statistical analysis to determine average absorption coefficients, their errors and the corresponding CeLIF values for both the S/N level and the S/DL via a custom Python script (Table 3.3). The absorption coefficients of the ring-down signals on and off resonance were determined using the standard ring-down method of a "blank" ring-down time (τ_0) and a corresponding ring-down with the absorber present (τ').

Table 3.3: Comparison of the S/N, detection limit and S/DL of the CRDS and CeLIF study.

| | On Resonance | | | | | | Off Resonance | | | |
| | CRDS/ppm | | | CeLIF/ppm | | | CRDS | | CeLIF | |
T/°C	Loss	σ_{Loss}	S/N	Loss	σ_{Loss}	S/N	σ/ppm	S/DL	σ/ppm	S/DL
75	0	0	0	0.485	0.096	5.0	0	0	0.03	6.0
85	0	0	0	1	0.178	6.0	0	0	0.05	7.6
95	0	0	0	4	0.676	6.0	0	0	0.04	31.2
105	18	15	1.2	15	2	6.5	18	0.4	0.08	64.3
115	54	15	3.6	52	83	6.3	17	1.1	0.19	90.0
125	132	23	5.8	148	25	5.8	16	2.8	0.75	65.4
135	355	46	7.7	332	64	5.2	16	7.4	1.74	63.4

During the data collection the maximum signal intensity of the traces was maintained around the 5 mV mark for both the CRDS and the CELIF PMTs. In performing the measurements in such a way the likelihood of PMT saturation was minimised. The CRD PMT could be operated with the same PMT voltage for all measurements. The CeLIF PMT, however, required several adjustments as the signal became progressively more intense as the oven temperature, and hence number density, increased. As a result, the signal intensities required scaling by a relevant factor to give a more accurate indication of the signal magnitude. These scaled values are used in the determination of the S/N ratios of the technique, whereas the nominal values obtained during the respective scans are used for determining the S/DL. This was done as the background value should scale with the obtained signal from the resonance scan.

The data for the S/N indicates that the two techniques do not differ in performance to any significant degree, with the CRDS apparently surpassing the CeLIF for shot-to-shot stability, although imperfect scaling of the CeLIF signal may be the cause of the difference. This variance can also be seen from Table 3.4 in which the noise from the background (τ_0) remains at a relatively constant level, while the signal

from the probed transition (τ') shows progression towards a much lower signal to noise ratio of τ. The most likely cause of the S/N ratios in both CRDS and CeLIF are fluctuations in the sample density in the molecular beam.

Table 3.4: Table of ring-down time data obtained both on resonance (τ') and mistimed nozzle (τ_0). The ring-down time and associated standard deviation (σ) are included along with the ratios between the τ and associated fluctuation.

T/°C	$\tau_0/\mu s$			$\tau'/\mu s$		
	τ_0	σ_{τ_0}	Ratio	τ'	$\sigma_{\tau'}$	Ratio
75	2.177	0.01438	151	2.167	0.0157	138
85	2.163	0.01679	129	2.153	0.0160	134
95	2.156	0.01664	130	2.141	0.0172	125
105	2.153	0.01638	131	2.123	0.0176	121
115	2.151	0.01411	152	2.067	0.0183	113
125	2.143	0.01477	145	1.947	0.0284	69
135	2.136	0.01436	149	1.685	0.0452	37

Analysis of the data with respect to the S/DL limit produced results which showed CeLIF to be more sensitive in a molecular beam environment. The CRDS only yielded signal discernable from the noise around an oven temperature of 115°C, even then only having signal strength slightly greater than three times the standard deviation of the background signal. CeLIF, on the other hand, had more than enough signal at the lowest scanned temperature (75°C), allowing a spectrum to be obtained with much lower number densities than with CRDS. The contrast between the two methods is likely the result of the sample length compared to the overall length of the cavity. With a molecular beam diameter of between 3-5 mm the interaction volume is much smaller than the overall size of the ring-down cavity (85 cm). Equation 3.12 illustrates how the sample pathlength influences the absorption coefficient value for the CRDS

$$\frac{1}{\tau'} - \frac{1}{\tau_0} = \alpha c \frac{d}{l} \tag{3.12}$$

in which d is the sample pathlength and l is the overall cavity length.

With the molecular beam having a significantly smaller diameter than the length of the ring-down cavity the interaction volume only allows a limited level of absorption, even with the multiple passes which define CRDS. Owing to this discrepancy between the length of the cavity and the absorption length of the sample the absorption coefficient must be corrected from the effective (α_{eff}) to the true (α_{true}) value. The LIF portion of the set-up does not suffer from this same problem. In CRDS the integrated density along the laser axis is responsible for the reduction in ring-down time (in addition to the conventional losses such as from the mirrors). As the entire

chamber is not filled with BPEB vapour the CRDS is not used to its full potential with respect to the entire laser pathlength interacting with sample molecules. LIF, however, is position sensitive and only produces signal from the photons which are collected through the lens and directed to the PMT. Using the current set-up the entire width of the molecular beam probe volume can emit photons in the direction of the LIF lens.

The performance of the CeLIF technique in terms of detection sensitivity can be related to the low background noise of the LIF component. With CRDS the system still suffers from a similar restriction to a standard spectrometer for absorption measurements in that eventually a small change in signal must be distinguished from a larger background. In the case of CRDS it is a signal change of $\tau_0 - 3\sigma_{\tau_0}$ from a background signal of τ_0. Using the τ_0 from the 75°C scan (before the sample can contaminate the mirrors and so reduce τ_0) this corresponds to a change from 2.177 μs to 2.134 μs, which places the start of the signal reduction around the 105°C. This reduction in ring-down time corresponds to an absorption coefficient value of $\approx 5 \times 10^{-4}$ m^{-1} (16 ppm).

Cavity mode effects can also influence the sensitivity of the CRDS as multi-mode excitation may result in a range of ring-down times and, hence, baseline noise. In the case of LIF, the mode structure of the cavity will have very little effect on signal (and background) as the method is a secondary technique. Since it only requires the absorption (of a photon for subsequent spontaneous emission) the mode the photon happened to be present in is irrelevant. Finally, as previously mentioned, the background component of the scan is the Rayleigh scattering, which is significantly less than a fluorescence signal and so any spectral features are easier to distinguish from the baseline. The incorporation of a spectral filter would eliminate the Rayleigh background altogether.

Previous CeLIF Type Studies

Simultaneous measurements of ring-down time and LIF, using a geometry similar to our set-up, have been performed in several investigations.[96–98] With each experiment having its own aim the advantages of combined CRDS/LIF measurements were not investigated.

The investigation by Luque *et al.*[96] was concerned with analysing CH radicals in low pressure flames. While both techniques were employed the LIF aspect was used to determine concentration distributions in the flame through the spatial imaging of the fluorescence. The investigation also noted the effect of cavity modes on the quality of the LIF signal produced. With the laser aligned to maximise the TEM$_{00}$ mode

the FWHM of the beamwaist was significantly narrower than with a more poorly aligned cavity (0.08 mm vs 2.2 mm). By combining the two techniques the group was able to extract a quantitative column density (CRDS) and also spatial distribution (LIF). For our study, the mode structure was less crucial as the technique has been used to generate spectra as opposed to determination of number density and its distribution.

The study by Tokaryk *et al.*[97] was also carried out on a molecular beam using cavity ring-down as the primary analysis tool. Their study was focussed on the location of a calculated electronic state which had, thus far, eluded detection using LIF. With the implementation of CRDS the group were able to locate the spectroscopic feature and find no corresponding LIF signal. With the combination of the two distinct methods they obtained simultaneous measurements of two different molecular properties, and subsequently identifying a known transition (which yielded simultaneous LIF and CRDS measurements) and then moving to find the previously unidentified feature. As with our research, they too did not set out to intentionally use the combined measurement.

The final study was conducted by Zwier *et al.*[98] with the aim of studying tropolone clusters, in particular the photophysics of the S_1 state. One of the main methods of analysis in the group was LIF, but with the addition of CRDS the experiment was run with the techniques acquiring data in tandem. While the group did not explore the method any further they concluded that an advantage of the simultaneous measurements was that "the ring-down cavity produces LIF scans with similar signal-to-noise to single-pass experiments, but without the saturation effects that invariably creep into the latter studies".

3.3.6 CeLIF and Optimised Single-Pass LIF

During the initial incorporation of the LIF set-up into the experiment the results of the BPEB scans were vastly inferior to those obtained using CRDS. With the subsequent development of the CeLIF technique an honest comparison between CeLIF and the optimum spLIF was sought. This was done to ensure the CeLIF was indeed superior in performance to the best spLIF possible with the available resources. The systems were tested for not only signal intensity, but also the detection sensitivity. Three different configurations were compared: the original spLIF with the telescope beam shaping optics in place i.e. the laser beam is the same size inside the cavity as with CeLIF, spLIF with a larger laser beam cross sectional area and finally the CeLIF method. The results of the three configurations are shown in Figure 3.18.
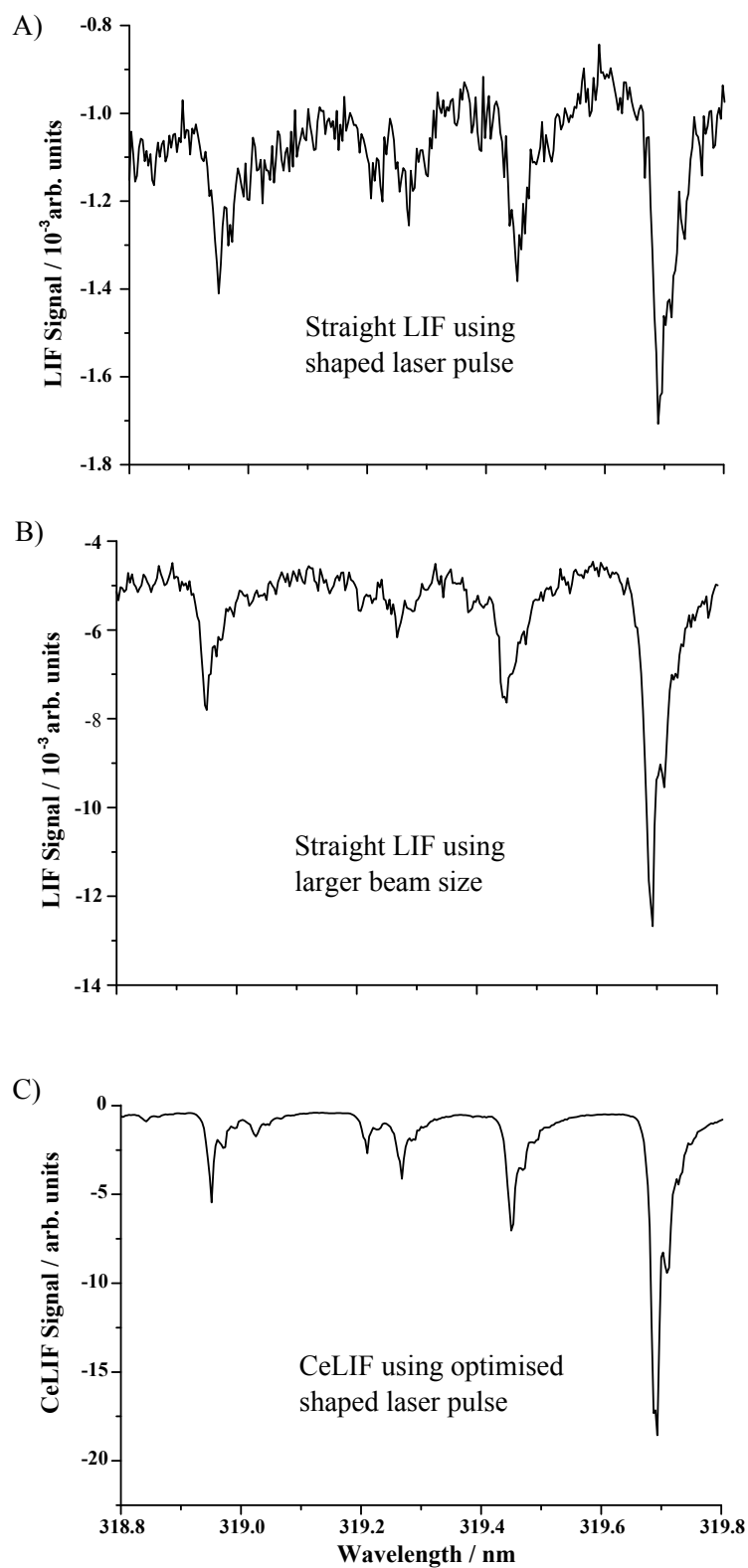
Figure 3.18: The optimised outputs from the LIF PMT under different conditions. In ascending order: A) with the beam shaping optics still in place, B) with the beam shaping optics removed and finally C) with the CeLIF set-up. The result obtained from the CeLIF has been inverted to match with the LIF spectra.

The main difference between each configuration employed related to the number of photons relative to the number density of sample molecules. In the original spLIF set-up the laser beam entering the cavity was the same size as that of the CRDS. By comparison, the size of the laser beam when the beam shaping optics were removed was larger by a factor of ≈ 300. The net effect of this was to increase the size of the laser beam which interacts with the molecular beam. The larger beam size has a dramatic effect on the probability (p) of a photon been absorbed by a sample molecule (Equation 3.13), in which the number of photons (n_{p}) and cross sectional area of the laser beam (A_{w}) provide the integrated photon flux.

$$p = 1 - e^{-\sigma \frac{n_p}{A_w}} \tag{3.13}$$

With the beam shaping optics in place the laser beam was focussed to a smaller size where it interacted with the molecular beam ($\approx 3 \times 10^{-3}$ mm^2). When compared to the size of laser beam at the molecular beam when the telescope assembly was removed (≈ 0.9 mm^2) the number of available sample molecules to excite was much greater in the larger beam case. As the number of photons in both instances is the same the sample probed with the shaped beam will experience a more intense photon pulse. Any sample molecules present in the volume of the focussed photons will be excited and the resulting fluorescence detected. The sample molecules within the volume are then essentially bleached and any remaining photons which have not been absorbed will continue on the beampath through the chamber. With the expanded beam the number of molecules available for excitation and, consequently, to emit photons for detection is increased.

Comparison between the three methods indicated that the original spLIF set-up provided the poorest performance overall, with the subsequent removal of the beam shaping optics providing a noticeable increase in signal quality. CeLIF, however, once again proved to be superior to the best spLIF obtained by a significant margin.

The signal produced in CeLIF is also a result of the shaping optics and focussed beam waist. With the presence of the cavity the laser pulse is effectively stretched to microseconds as opposed to the 5 ns in the spLIF. This lengthened pulse also contains less photons per pass by virtue of the mirror transmittance and the mode structure of the cavity. This reduction in photon density limits the likelihood of saturation due to bleaching the probe volume.

3.3.7 Large Absorption Cross Section

If, as in our case, the fluorescence lifetime of a compound is significantly shorter than the ring-down time the LIF signal will follow the ring-down transient (Figure 3.19).
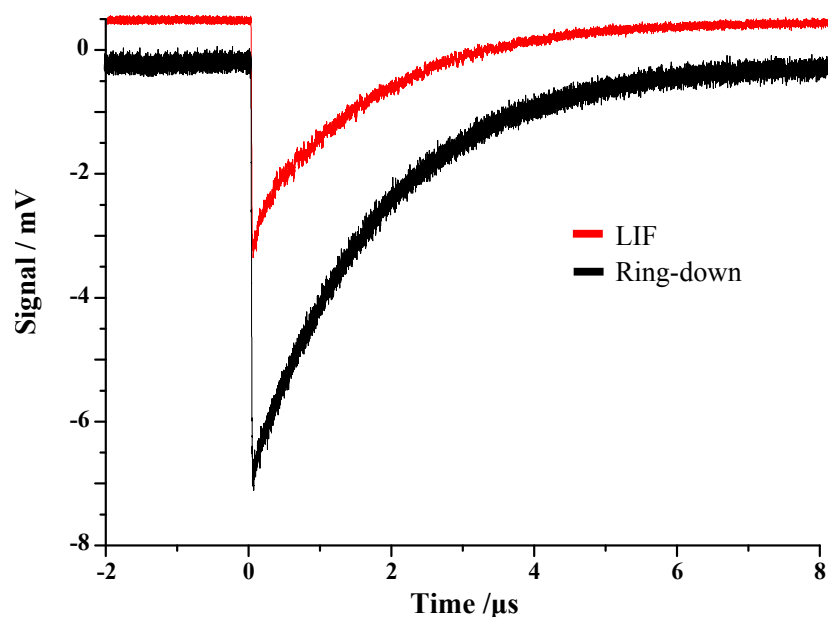
Figure 3.19: CeLIF signal trace of BPEB taken during a scan at 319.61 nm and 135°C oven temperature.

However, BPEB produced an additional signal type when the fluorescence was emitted from a strong absorption feature (the fundamental absorption peak in this instance). While the majority of the scan range yielded fluorescence transients which followed the laser pulse decay in the cavity, the transient obtained from the fundamental transition (Figure 3.20) was found to take on a form which did not follow the exponential decay of the ring-down transient. Initially this effect was thought to be the result of the gain causing saturation of the PMT.

Figure 3.20: CeLIF signal trace taken on fundamental absorption peak at 319.68 nm and 135°C oven temperature.

To corroborate this the scans were performed with PMT voltages which yielded signal intensities of ≈ 5 mV. These scans also produced similar transients to those seen during the earlier stages in the research, when the PMT voltage may have been too high to avoid saturation of the PMT.

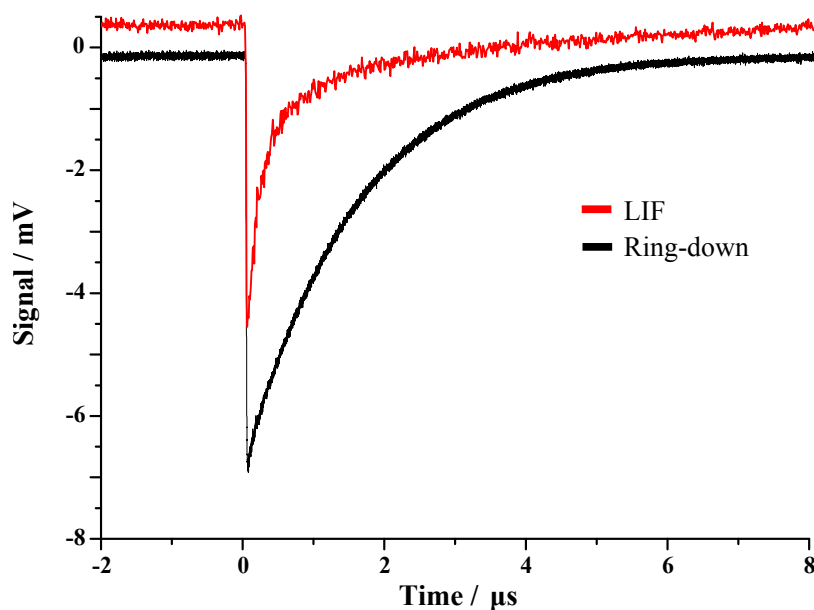Additionally, this effect was seen at reasonably low oven temperatures (<95°C) as the fundamental peak was used to establish and optimise the fluorescence signal (Figure 3.21). With the reduced temperatures came the lower corresponding number density of the sample molecules. Since the signal distortion was still seen at these temperatures it was further evidence that something more than simple PMT saturation effects were responsible for the signal achieved.

After preliminary simulation work it was found that the signal shape may be influenced by several variables which result in the bleaching of the sample compound from the laser probe volume.

Using the probability of absorption of a photon (Equation 3.13), the degree of excitation is such that the initial signal peak is seen to be the result of bleaching away of the sample in the molecular beam, when the photon pulse first interacts with the molecules at the start of the ring-down event. As the time between round trips is shorter than the speed of the molecular beam the molecules are not replaced as quickly as they are removed through excitation. As a consequence the fluorescence signal is significantly greater at the start of the process compared to the end. The tail end of the CeLIF signal, which appears as a more constant reduction in signal magnitude, is the product of the molecular beam refreshing the probe volume
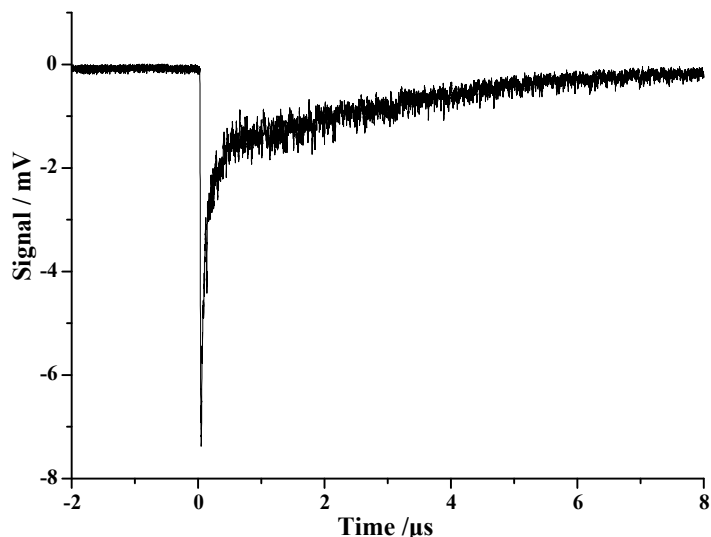
83

Figure 3.21: CeLIF signal trace taken on fundamental absorption peak at 319.68 nm and 87°C.

with non-excited "virgin" molecules, and so can be viewed as a more steady state environment. A study by Brown *et al.*[99] found a similar trend when analysing the kinetics of NO_2 formation. While monitoring the concentration of NO_3 in the system the group found that logarithmic plots of the ring-down data yielded results which were not linear. As such they attributed this change in behaviour to the NO_3 concentration changing quicker than the total ring-down time as the slope of the τ' signal eventually returned to that of the empty cavity τ_0. In the case of the CeLIF set-up it was possible to see the extent of signal change during the ring-down event which would otherwise be missed as we tended to fit the CRD decay from about $0.5\mu s$ after the cavity excitation, thus the likelihood of noticing the non-exponential decay in the CRD was minimal.

3.3.8 "Fast" Fluorescence vs "Slow" Fluorescence

A common feature of the molecules used in this study was their short (sub-nanosecond) fluorescence lifetime. The SO_2 fluorescence excitation spectra were repeated using the CeLIF technique (Figure 3.22) to test if CeLIF also shows enhancement when the fluorescence lifetime of the molecule is long (comparable to the ring-down time in this case). When compared to Figure 3.5, from the initial LIF trials, the quality of the spectrum can be seen to be only slightly better than that obtained from the conventional LIF measurements.

While the absorption cross section plays an important role in CeLIF for the production of sufficient fluorescence signal the success of the technique appears to be more influenced by the fluorescence lifetime of the molecule. In the case of the analysed
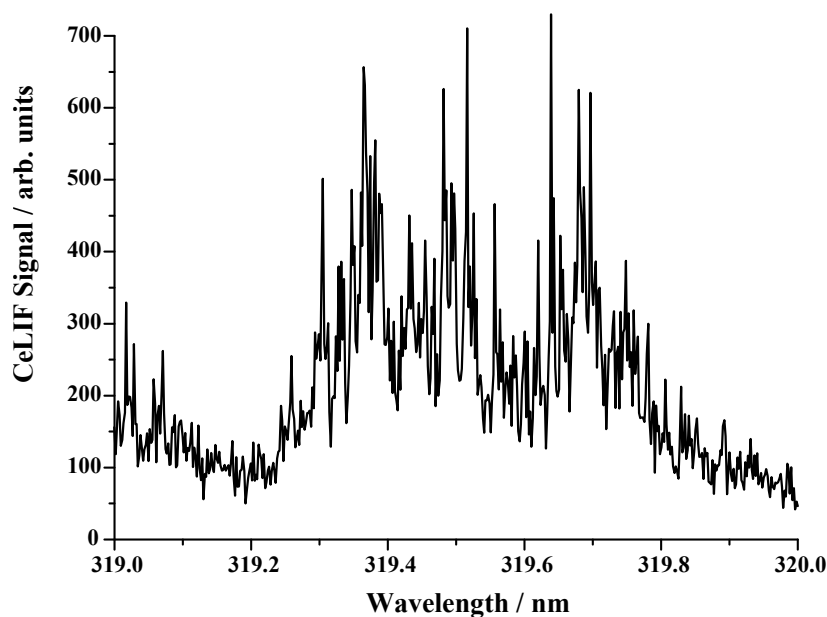
(a) CeLIF scan of SO_2.
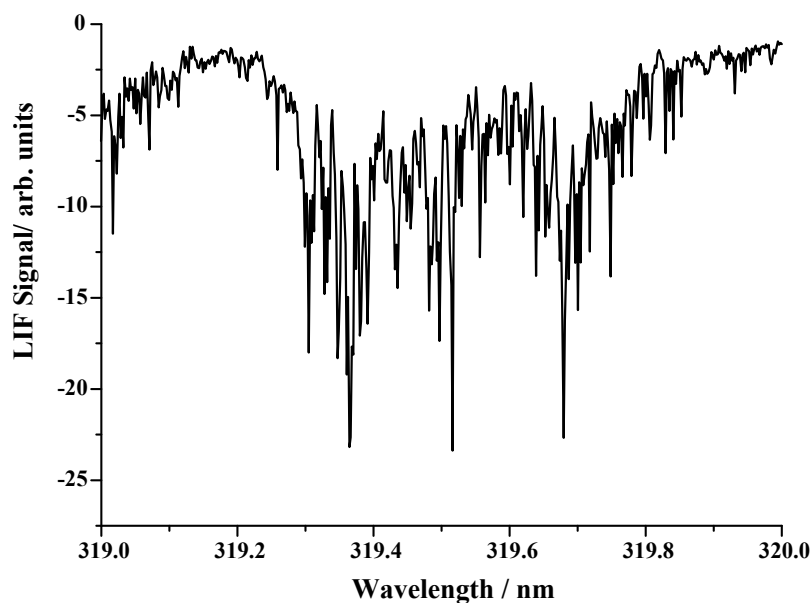
(b) Original LIF scan carried out on SO_2 using spLIF.

Figure 3.22: Comparison between the original LIF measurement and CeLIF analysis. From the results it can be seen that the spectra are qualitatively similar.

organic molecules all have sub-nanosecond fluorescence lifetimes and so undergo the emission process significantly faster than the SO_2, which has a fluorescence lifetime on the microsecond timescale. As the laser pulse is confined within the cavity the photons will make multiple trips through the sample. However, unlike the sub-nanosecond fluorescence lifetime of the organic molecules, the SO_2 will emit photons over a much longer period of time. This period of emission is in excess of the the roundtrip time of the laser pulse in the cavity (≈ 5.5 ns), meaning the SO_2 continues to produce fluorescence signal even as more and more molecules are excited (and

begin fluorescing) by successive laser pulse roundtrips. This has the result of the fluorescence signal lasting significantly longer than the ring-down event and so brings difficulty in normalising the signal with the ring-down area (Figure 3.23).
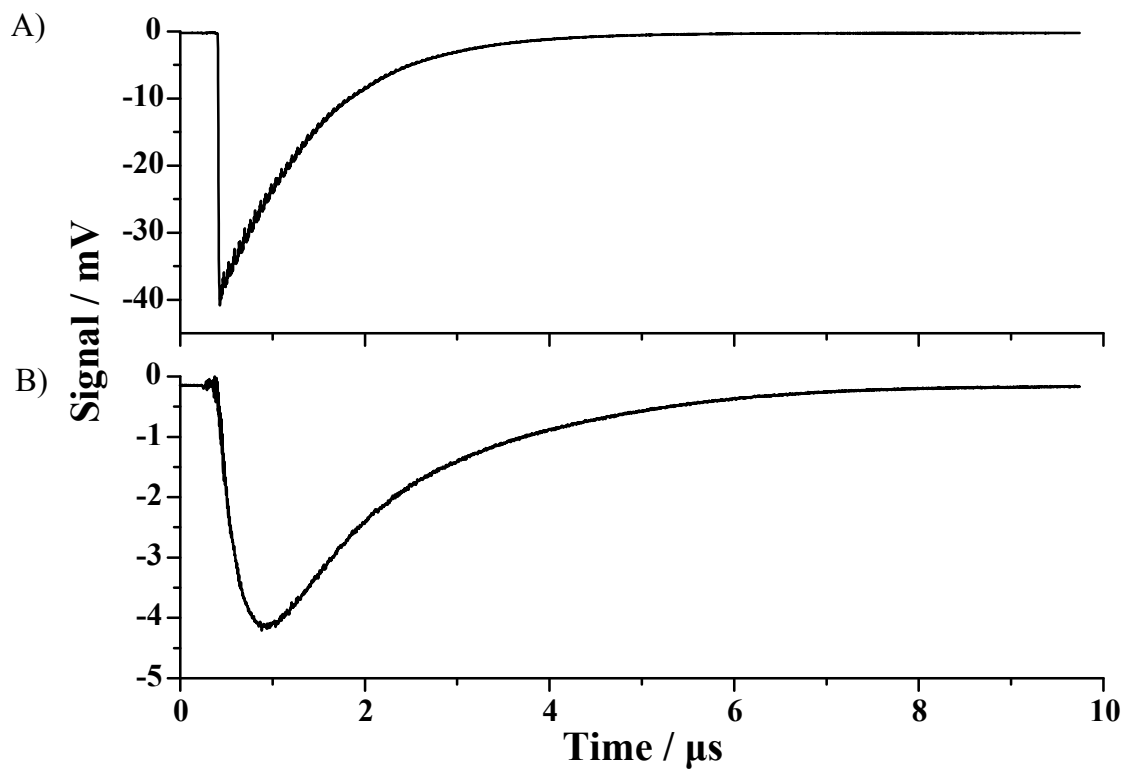
Figure 3.23: (A) A ring-down transient of SO_2 with accompanying (B) CeLIF signal CeLIF signal trace.

Chapter 4

Spectra of a New Polyaryl Molecule: 2,5-bis(phenylethynyl)thiophene

4.1 From Benzene to Thiophene

With the success of the 1,4,bis-(phenylethynyl)benzene and 1,4-diphenylbutadiyne spectra a new molecule was selected for analysis using CeLIF.

2,5-bis(phenylethynyl)thiophene (BPET) was selected as the C_{2v} symmetry of the the molecule was anticipated to yield a spectrum similar in complexity to that of BPEB. In addition to the potential spectral similarities with BPEB the molecule also displayed a favourable vapourisation curve as well as possessing an absorption profile which lay within the useable range of the cavity ring-down mirrors (Figure 4.1).

Where BPEB is a linear arrangement of three benzene rings separated by ethynyl linker units, the BPET molecule possess a thiophene ring in the middle section of the chain of three rings. Thiophene, however, displays its conjugation as a result of one of the lone pairs of the sulphur atom (in a p-obital) completing the conjugated system between the four carbon atom p-orbitals. The sulphur orbital used in the conjugation is the $3p_z$-orbital and so the quality of overlap is less than in benzene (or furan and pyrrole) owing to the carbon electrons (used in delocalisation) being located in the $2p_z$-orbital.
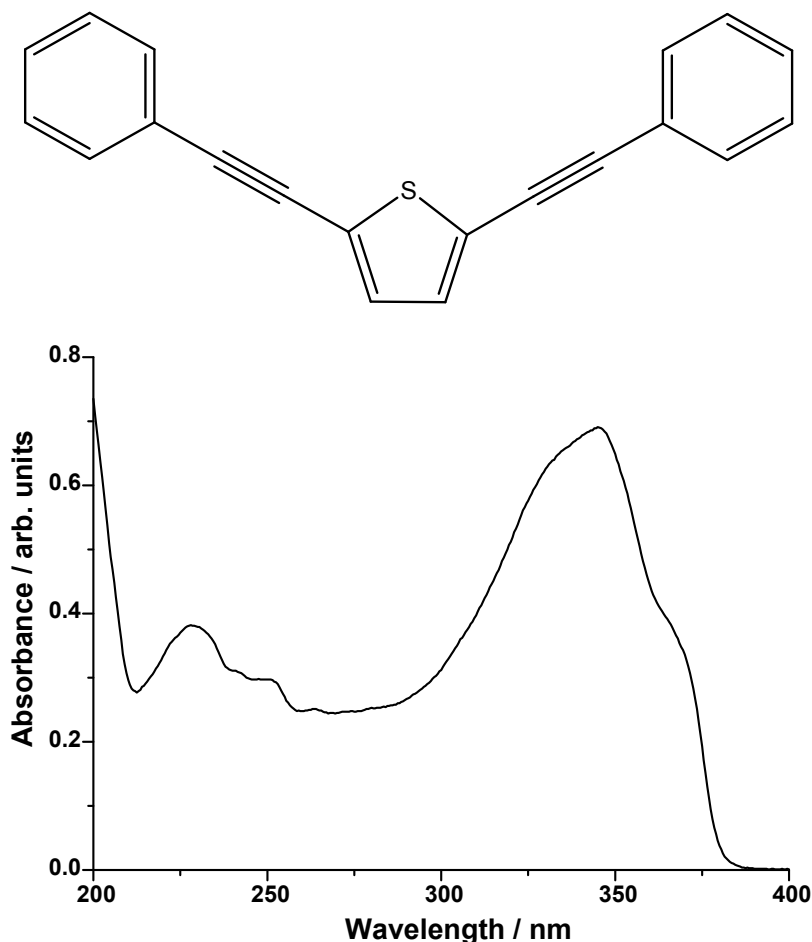
Figure 4.1: 2,5-bis(phenylethynyl)thiophene with accompanying UV spectrum carried out in hexane.

Areas of interest studied in thiophene containing architectures have included their non-linear optical properties[100;101] and luminescence qualities.[102;103] During the non-linear studies by Lind *et al.*[101] it was found that increasing the length of the side chains, and hence extent of π conjugation, resulted in increasing the observed non-linear effect of absorbing probe laser energy. Of note from the luminescence study undertaken by Rodriguez *et al.*[102] was the decrease in quantum yield (Φ_F =0.34 decreasing to Φ_F =0.1) for 2,5-substituted thiophene systems when linking the 2,5-bis(phenylethynyl)thiophene unit to an additional thiophene molecule using a double bond (Molecule B) as opposed to a triple bond (Molecule A) (Figure 4.2).

Thiophenes have also been investigated, in a similar fashion to benzene based systems, through the use of scanning tunneling microscopy.[104] During the investigation it was found that the thiophene systems scrutinised displayed non-linear behaviour when larger voltages were applied between the electrodes. This took the form of a step like pattern, which was later accounted for by considering the discrete energy levels in the molecule. With interest in the properties of these molecules when attached a metal surface Casado *et al.* studied thiophene based molecules which
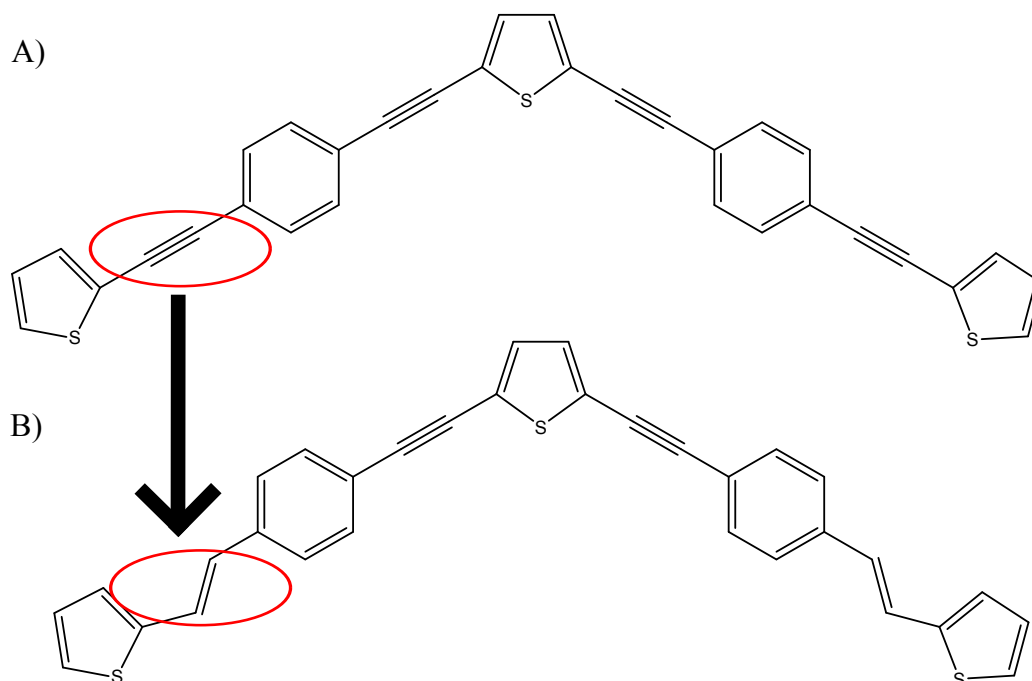
Figure 4.2: Decrease in quantum yield.

contained sulphur linking atoms, but were not themselves chemically bonded to a metal electrode.[105] Part of the motivation for carrying out this research was interest in the chemically bonded sulphur distorting the true HOMO and LUMO levels of the extended π system in the molecules.[106] The samples were analysed using both IR and Raman spectroscopy, with the results compared to theoretical vibrational data calculated by the group. By comparison to the calculated results the group was able to assign spectroscopic features to various vibrations within the molecules and determine the impact the degree of conjugation had on the samples molecular properties.

Analysis of 2,5-bis(phenylethynyl)thiophene

Acquiring a vapour phase spectrum of the BPET proved extremely difficult and so an alternative approach was adopted. Previous work, carried out in the department, into the photophysics of such molecules meant that absorption and fluorescence spectra had been recorded at 77 K in an argon matrix (Figure 4.3).[107]

This data allowed the identification of an approximate area to scan the dye laser over in the search for an absorption/fluorescence signal. Additionally, the solution UV-scans of BPEB and DPB had revealed a solvent shift of up to approximately 20 nm when proceeding from a solution UV-measurement to one in the gas phase. With these two molecules displaying a similar shift in absorption from solution to vapour phase measurement the scanning wavelength for BPET transitions was adjusted by

89
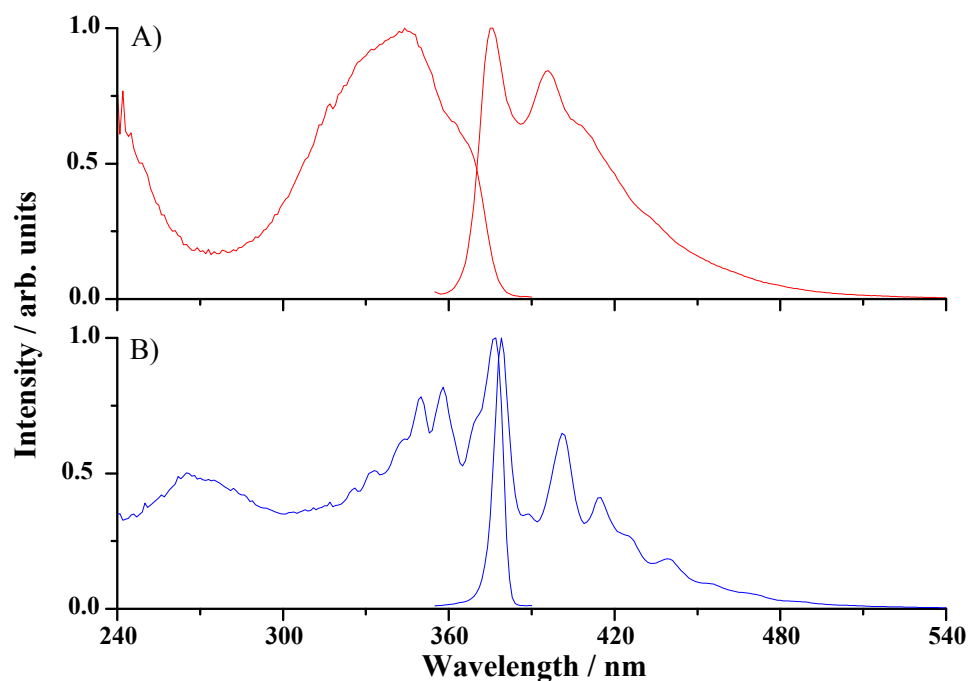
Figure 4.3: The UV absorption (left) and emission (right) spectra of BPET taken at A) 298 K in cyclohexane and B) 77 K in an argon matrix.

a similar margin. Taking this into account it was decided to scan the laser over a range originating around 350 nm, with the DCM laser dye exchanged for Pyridine 1.

Use of CeLIF made it possible to locate the Rayleigh scattering from the sample molecules seeded in the molecular beam. With the detection of the molecules in the beam the nozzle firing time could be optimised to allow the successful interaction of the laser pulse with the molecular beam. This resulted in the detection of several peaks from the photoexcitation spectrum of BPET.

Gradual heating finally resulted in the production of an absorption spectrum, from the cavity ring-down, using both oven designs. However, the newer design was found to yield a more intense spectrum and produce them at higher oven temperatures (120°C) than previously obtained with the older oven, before the sample completely vapourised. Both units managed to produce spectra at an oven temperature of 105°C, with the older model expelling all of the BPET sample around this temperature in approximately 10 minutes. Since the new design yielded results up to an oven temperature of 120°C, this allowed the identification of additional features in the absorption spectrum. While the absorption spectra did reveal several features the CeLIF proved more useful as it allowed the detection of peaks lost in the noise of the absorption spectra. The CeLIF scans also produced results over a much wider wavelength range (353-343 nm) compared to those obtained using the cavity

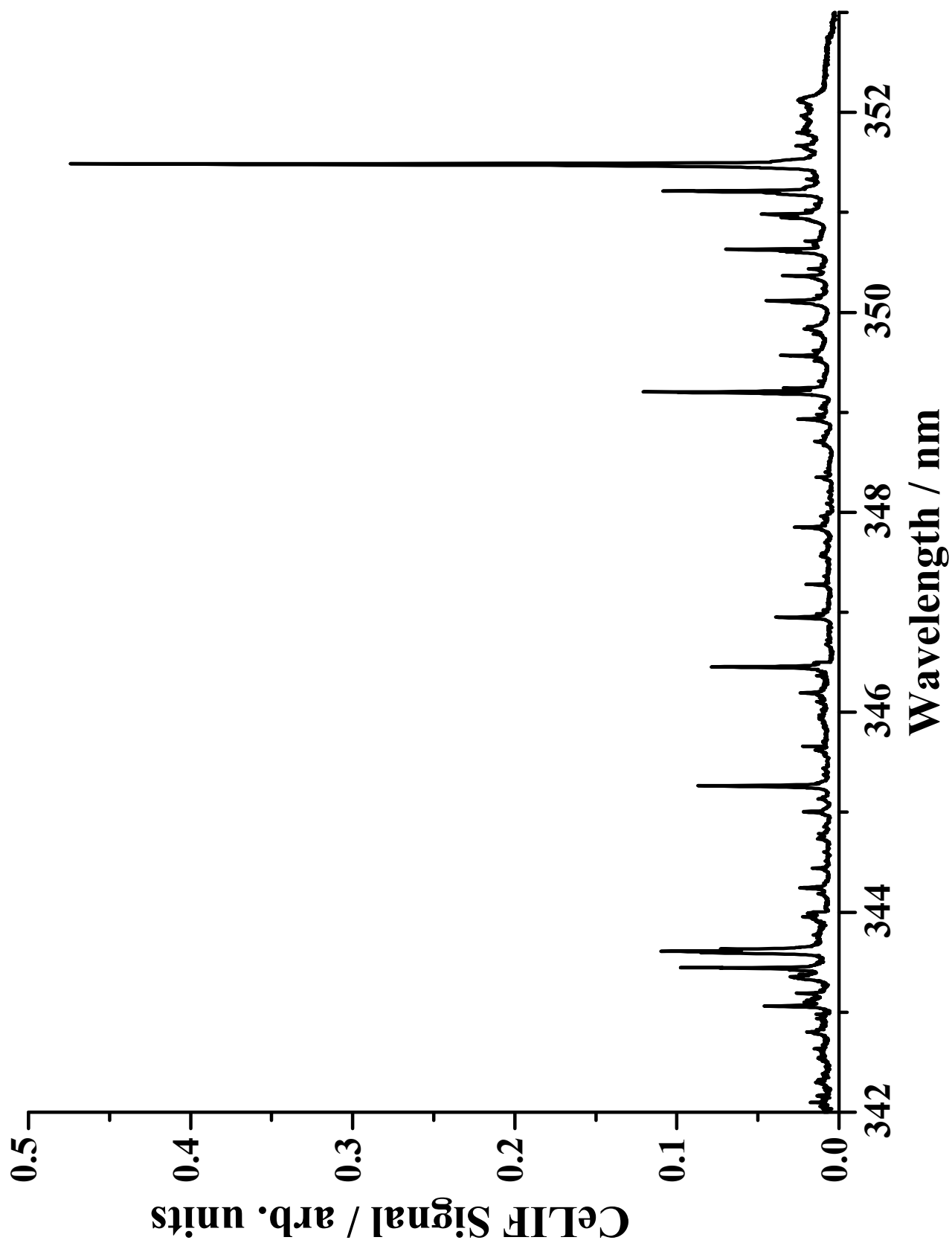ring-down (353-348 nm).

Figure 4.4: CeLIF spectrum of BPET taken at an oven temperature of 80°C.

4.2 Torsional Barrier in 2,5-bis(phenylethynyl)thiophene

4.2.1 Analysis of Spectra

After successfully obtaining spectra of 2,5-bis(phenylethynyl)thiophene the data could then be analysed to determine the torsional barrier height of the system. In order to accomplish this the normal vibrational modes, and torsional in particular, of the molecule are required. This was accomplished by employing the lumped-inertia technique as used in the previous work by S.Greaves.[48]

The Lumped-Inertia Technique

The lumped-inertia technique was initially developed for use in mechanical engineering to describe bending and flexing vibrations of nanorods and nanotubes.[108] Of particular importance was the work done by Qiao *et al.* which was concerned with the torsional vibration of a non-uniform shaft carrying an arbitrary distribution of discs.[109] Zheng *et al.*[48] adapted the method for use with linear polyphenylenes and polyethynylphenylenes for simulating the torsional frequencies of the systems. Employing the lumped inertia method allows the deduction of the force constants, k, from the phenyl ring torsional motions.

Using the method simplifies the analysis of the system by treating each ring as a "lumped-inertia" about the principal axis of the molecule. This lumped-inertia is equivalent to the ring and accompanying attached hydrogens and other substituents, with adjacent inertias interacting via force constants. The system is treated as a rigid body i.e. attached hydrogens etc do not move. The equations of torsional motion are described using the angle of the particular inertia relative to the principal axis, with a three ring system taking the form

$$
\begin{aligned}
I_1\ddot{\theta}_1 &= k_1(\theta_2 - \theta_1) + k_2(\theta_3 - \theta_1) \\
I_2\ddot{\theta}_2 &= k_1(\theta_1 - 2\theta_2 + \theta_3) \\
I_3\ddot{\theta}_3 &= k_1(\theta_2 - \theta_3) + k_2(\theta_1 - \theta_3)
\end{aligned}
\tag{4.1}
$$

This representation allows the determination of the second derivative of the torsion angle $(\ddot{\theta})$, yielding the symbolic relationship

$$
\vec{\ddot{\theta}} = \mathbf{M}\vec{\theta}
\tag{4.2}
$$

where θ_j is the angular position of the jth phenyl ring relative to its position at equilibrium and I_j is the reduced moment of inertia of the ring about its twist axis. $\mathbf{M}$ is a $n \times n$ matrix (in this case a 3×3 matrix as three rings are under consideration) and k_i is the torsional force constant between the analysed ring and its ith closest neighbour.

$$\mathbf{M} = \begin{pmatrix} \frac{-(k_1+k_2)}{I_1} & \frac{k_1}{I_1} & \frac{k_2}{I_1} \\ \frac{k_1}{I_2} & \frac{-2k_1}{I_2} & \frac{k_1}{I_2} \\ \frac{k_2}{I_3} & \frac{k_1}{I_3} & \frac{-(k_1+k_2)}{I_3} \end{pmatrix}$$

Using the relationship $e^{ib} = \cos b + i \sin b$, Equation (4.2) can be re-written as

$$\vec{\theta} = \vec{C} e^{-i\omega t} \tag{4.3}$$

where $\vec{C}$ is a vector of coefficients (amplitudes of the vibrations), $i = \sqrt{-1}$, t is time and ω is a vibrational frequency. From Equation (4.3) it follows that by eliminating the exponential term the relationship becomes

$$\mathbf{M}\vec{C} = -\omega^2 \vec{C} \tag{4.4}$$
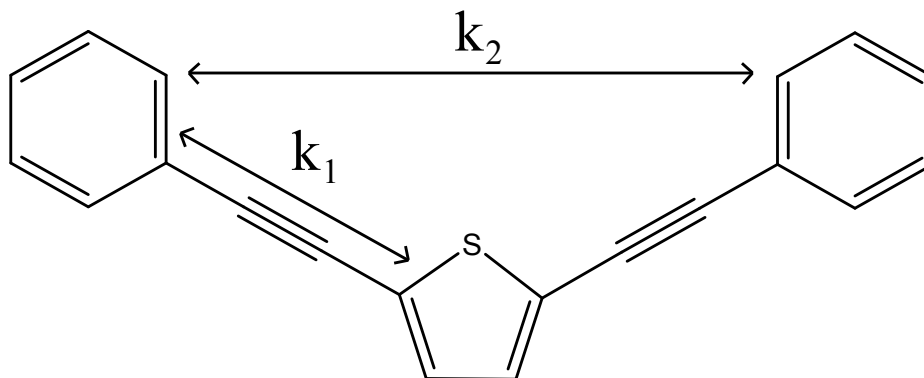
Figure 4.5: Identities of the two (torsional) force constants in the determined eigenvalues. k_1 represents the force which exists between a ring and its nearest neighbour (in this case the thiophene), and k_2 to the interaction between the ring and its next nearest neighbour (the phenyl ring on the other side of the thiophene).

The eigenvalues, $-\omega^2$, and eigenvectors are obtained in the form of force constants $(k_1, k_2...)$ by solving the eigenvalue problem (Equation (4.4)). In addition to the force constants the reduced moment of inertia (I_{red}) is also extracted from solving the

eigenvalue equation. In the matrix the reduced moments of inertia have identities $I_1 = I_3 = I_{\text{outer}}$ and $I_2 = I_{\text{inner}}$. In this case the outer inertias are the phenyl groups and the inner is the thiophene ring.

Table 4.1: Eigenvalues and eigenvectors obtained for the BPET molecule.

Vibration	Eigenvalue $-\omega^2$	Eigenvectors		
		C_1	C_2	C_3
Rotation	0	1	1	1
Antisymmetric	$-\dfrac{k_1 + 2k_2}{I_{\text{outer}}}$	-1	0	1
Symmetric	$-\dfrac{k_1(2I_{\text{outer}} + I_{\text{inner}})}{I_{\text{inner}}I_{\text{outer}}}$	1	$-\dfrac{2I_{\text{outer}}}{I_{\text{inner}}}$	1

In Table 4.1 the eigenvalue of zero corresponds to the rotation of the entire molecule in space. The eigenvalue of the antisymmetric motion contains a $2k_2$ term to compensate for the double angle size (and so restoring force constant) of the interaction between the two phenyl rings. If the long range interactions are neglected for the eigenvalue of the antisymmetric motion it simplifies to

$$-\omega_{\text{anti}}^2 = -k_1/I_{\text{outer}} \qquad (4.5)$$

In doing so, however, the accuracy of the method is reduced, as remarked by Zheng et al.[48]

4.2.2 Simulation Program

For the successful simulation of the BPET spectra, the symmetric and antisymmetric torsional potentials of the modes are required. The determination of the energy levels of these two potentials provides the location of the line transitions of the two modes. Additionally, the wave functions of the transitions are determined to provide the Franck-Condon factors for the transitions. When combined with the Boltzmann distribution the peak intensities can be calculated and matched to the spectrum. A program was developed by E. Wrede during the previous research into the torsional motions of BPEB and was employed for use with the new BPET molecule. The following pages describe a brief overview of the methodology of this simulation program.
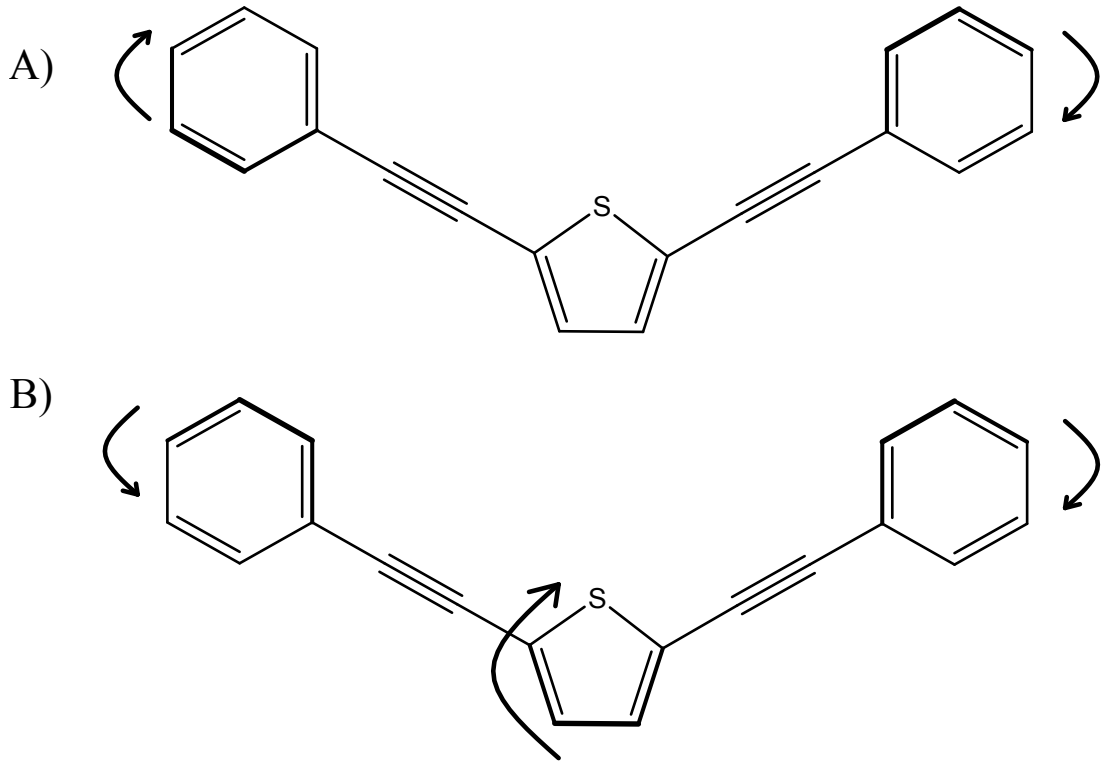
Figure 4.6: The A) Antisymmetric and B) Symmetric torsional motions of the BPET molecule.

Simulating Energy Levels

To determine the energy of each vibrational level of the system the program calculates the result of the one-dimensional Schrödinger equation.

$$-\frac{\hbar^2}{2I_{\text{red}}}\frac{d^2\psi}{d\theta^2} + V(\theta)\psi(\theta) = E\psi(\theta) \tag{4.6}$$

Where $V(\theta)$ is the potential at a particular torsional angle of the phenyl ring with respect to the ethynyl axis, and I_{red} is the reduced moment of inertia. The wave functions of the system can be expanded as a linear combination of periodic basis functions $\psi_i(\theta)$,

$$\psi_v(\theta) = \sum_i^N a_{iv}\psi_i(\theta) \tag{4.7}$$

where a_{iv} is the expansion coefficient.

We employ the method described by Lewis *et al.*[110] to describe the Schrödinger equation, and use the following periodic basis set

$$\psi_{(m)} = \frac{1}{2\sqrt{\pi}}e^{im\phi} \qquad m = 0, 1, 2... \tag{4.8}$$

95

the even and odd symmetry of the system can be maintained by expressing the set
in terms of real cosine and sine functions

$$\psi_0^{\text{even}} = \frac{1}{\sqrt{2\pi}} \tag{4.9}$$

$$\psi_n^{\text{even}} = \frac{1}{\sqrt{\pi}} \cos n\theta \quad n = 0, 1, 2, 3... \tag{4.10}$$

$$\psi_n^{\text{odd}} = \frac{1}{\sqrt{\pi}} \sin n\theta \quad n = 0, 1, 2, 3... \tag{4.11}$$

$$\tag{4.12}$$

using these basis functions the boundary condition $\psi_{v\theta} = \psi(\theta + 2\pi)$ is satisfied. The
Hamiltonian matrix of the system is then constructed as

$$H_{kl} = \int_0^{2\pi} \psi_k^* \hat{H} \psi_l d\theta \tag{4.13}$$

The Schrödinger equation in matrix form is then

$$\mathbf{H}\vec{a}_v = E_v \vec{a}_v \tag{4.14}$$

The energy levels located near the bottom of the potential well are doubly degen-
erate, while those at the top tend to split apart and above the potentials maximum
they rearrange to form further doubly degenerate pairs.[110]

Transition Line Strengths

With the simulation of the appropriate wave functions the program can then deter-
mine the intensity of the transition by taking into account two factors: the square
of the transition moment integral and the Boltzmann distribution of the molecule
at a particular simulated temperature.

The intensity of a vibrational transition is proportional to the transition moment
integral, which is composed of the electronic transition dipole moment, μ, and the
vibrational overlap integral.[111]

$$\langle \nu' | \nu'' \rangle = \int_0^{2\pi} \psi_{\nu'}^* \psi_{\nu''} d\theta \tag{4.15}$$

If the electronic transition moment is assumed to be constant with regards to the
torsion angle (θ), then the transition intensity is thus proportional to the Franck-

Condon factor, $|\langle\nu'|\nu''\rangle|^2$. The transition moment integral can then be combined with a Boltzmann distribution

$$\frac{n_\nu}{n_0} = \exp\left(-\frac{G_\nu - G_0}{k_B T}\right) \tag{4.16}$$

in which n_0 and n_ν are the populations of the ground ($\nu = 0$) and the ν-th vibrational level, which with energies G_0 and G_ν respectively. In our case T is the torsional temperature of the sample molecules in the molecular beam.

Inspection of the spectra showed each torsional peak displayed a similar shape, thought to come from a combination of vibrational hot bands and of non-torsional modes and rotations. The shape of each hot band/rotational transition was simulated using a mixture of Gaussian and Lorentzian functions.

$$f(\bar{\nu}) = g\exp\left\{(-4\ln 2)\left(\frac{\bar{\nu}_0 + p\Delta E}{w}\right)^2\right\} + (1-g)\frac{w^2}{4(\bar{\nu} + p\Delta E)^2 + w^2} \tag{4.17}$$

in which ΔE is the energy between the hotbands, w the FWHM of the peaks, p is the peak number of the hot band, $\bar{\nu}_0$ the line position of the torsion and the g factor is the degree of Gaussian character the peak possesses. The intensity of the additional peak portions are determined using a Boltzmann distribution

$$h_p = \exp\left\{-\frac{p\Delta E}{k_B T}\right\} \tag{4.18}$$

where T is the temperature of the extra vibration (which is not the same as the torsional temperature). The energy separation, temperature, Gaussian character, FWHM and number of peaks in the progression are all altered to produce a peak which best fits the experimental data.

4.2.3 Simulation of BPET Vibrations

The spectra of the BPET are composed of a variety of transitions. These are not necessarily the result of the torsional motion of the phenyl rings on the molecule. Simulations were carried out using Gaussian09 to gain a better understanding of the possible transitions which could cause these spectral features.

Density Functional Theory (DFT) calculations were performed using the 6-311G** basis set with the addition of polarisation and diffuse orbital functions to better aid in determining the vibrational motions. All calculations were performed using the B3LYP functional.

The ground state geometry of BPET was determined by allowing all coordinates in the molecule to be optimised, with restraints to bond lengths, angles and dihedral angles removed. The optimised structure was used to simulate the vibrational motions of the molecule and also to determine the highest occupied molecular orbital (HOMO) and the lowest unoccupied molecular orbital (LUMO) of the molecule. The molecule was found to have a planar conformation and has been compared to data obtained from x-ray crystallographic measurements of the solid state molecule (Table 4.2).[107]
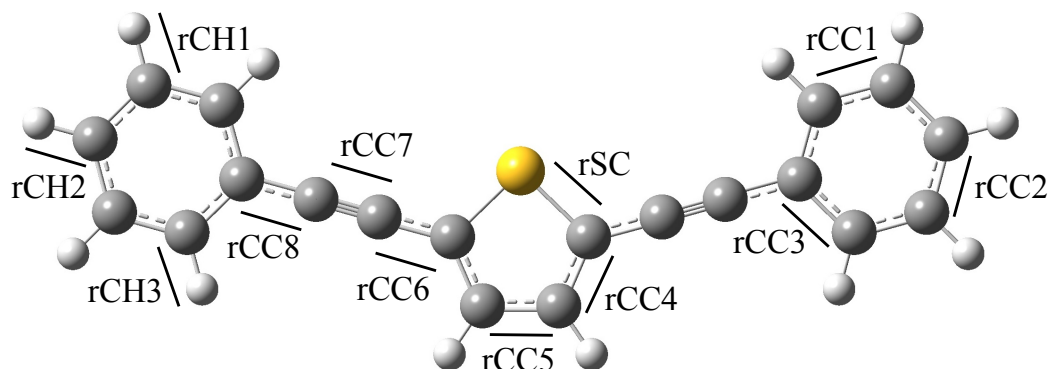
Figure 4.7: Bond length labeling for use with Table 4.2.

Table 4.2: Comparison of the solid state, x-ray crystallography bond lengths with those obtained using the B3LYP/6-311G** level of theory for simulating the molecule and determining its bond lengths.

Bond Identity	Crystallographic Bond Length / Å	Gaussian Bond Length / Å
rCS	1.73	1.74
rCC1	1.39	1.39
rCC2	1.39	1.39
rCC3	1.41	1.41
rCC4	1.38	1.38
rCC5	1.41	1.41
rCC6	1.43	1.40
rCC7	1.21	1.21
rCC8	1.44	1.42
rCH1	0.93	1.08
rCH2	0.93	1.08
rCH3	0.93	1.08

In contrast to the widely studied BPEB and tolane, BPET does not form planar stacks in its crystal structure. In BPET the two phenyl substituents are twisted out of the plane along the ethynyl bond axis. In addition to this torsional displacement the carbon chain linking the thiophene ring to the phenyl group also displays a bending feature, moving the phenyl rings out of plane with the thiophene portion.[112]

One of simplest periodic forms to represent the potential well of a molecule is

$$V(\theta) = \frac{1}{2}V_{\mathrm{max}}(1 - \cos 2\theta) \qquad (4.19)$$

where V_{max} is the torsional energy well depth and θ is the twist angle between the central thiophene ring and the phenyl substituents. This model was employed by S. Greaves for the work towards the study of BPEB, with the function in Equation 4.19 implemented in the computer program written by E. Wrede to simulate torsional specta. In order to employ the same program for BPET the torsional potential well shape was calculated using Gaussian09. This was accomplished by performing the calculations on the optimised BPET conformation, but with a fixed twist angle along the ethynyl bridge. This angle was varied from 0° to 90°, with all other parameters (such as bond lengths and bond angles) allowed to optimise.

This function yielded a fit which showed reasonable agreement with the results of the plotted Gaussian calculations. Deviations were found towards the lower portion of the potential well (Figure 4.8), but were deemed to be insufficient in causing significant problems with the resulting spectral simulation. This deviation in the model was also seen in the torsional potential well of BPEB. The level of deviation was more so than that seen in BPEB, but not to a significant degree.

Changes in bond lengths and angles as a function of torsion were also examined. Only minor changes were observed, most notably the distance between the central thiophene ring and the attached phenyl substituents increased by approximately 0.01Å ($\approx 0.25\%$) when rotating from the planar conformation to the perpendicular.

The Excited State

In addition to the energy of the ground state the optimised structures were also used to calculate the excited state energy of the molecule at each of the restricted torsional angles. This was done by employing the time-dependent DFT (td-DFT) method, again using the B3LYP/6-311G** level of theory. The optimised structure at each torsional angle was used as the basis for the excited state calculation. By calculating the first ten molecular excited states of the BPET molecule the shape and approximate depth (relative to the ground state) of these states could be determined.

When plotting the results of the excited state calculations (Figure 4.9), taking into account that td-DFT calculates excitation energies, an avoided crossing between the first two states at $\approx 80°$ can be seen. This is most prominent in the antisymmetric torsion energy surface, where the crossing can be followed in to the second excited state. Even though the crossings of the potential energy surface of the excited states
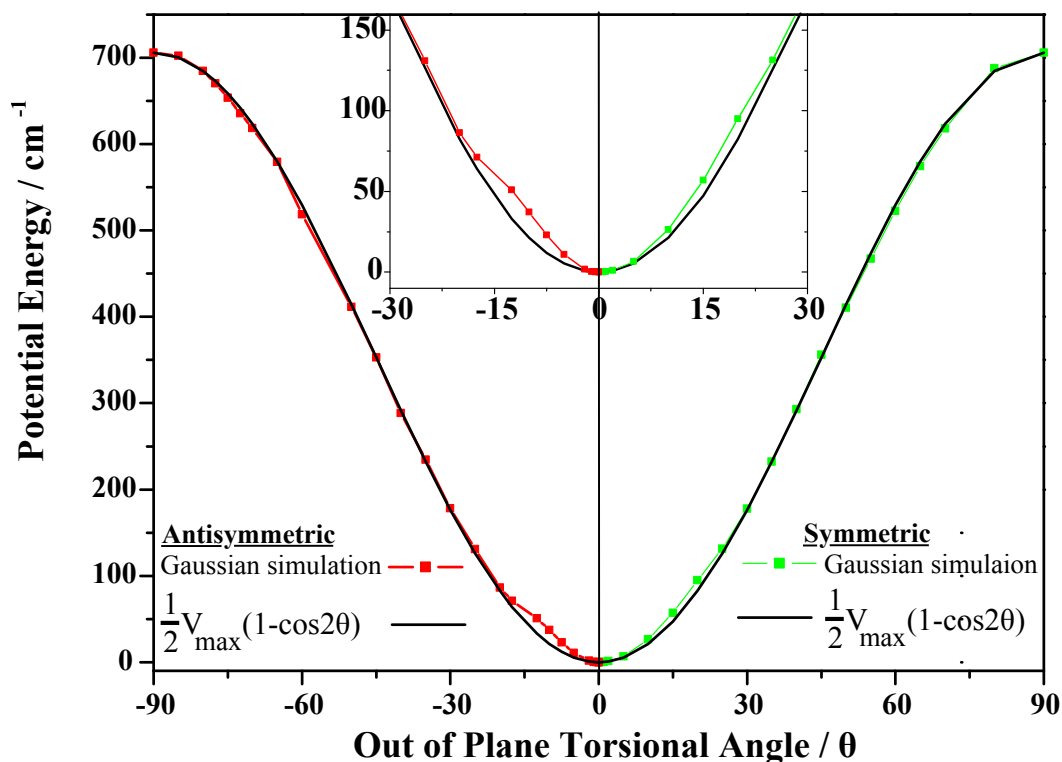
Figure 4.8: Ground state torsional potentials of the symmetric and antisymmetric ring twisting modes of BPET. The inset shows the lower portion of the well which displays the deviation of $V(\theta) = \frac{1}{2}V_{\max}(1 - \cos 2\theta)$ from the calculated energies.

meant the true potential well shape would require a more complex analysis, for the purposes of this research Equation 4.19 was sufficient to model the lower portion of the excited state well.

Spectral Simulation

After determining the torsional potential wells could be successfully described using Equation 4.19 the simulation program was used to generate a fit to the experimental data. To determine the reduced moments of inertia for the two torsional motions the results of the Gaussian calculations were used. The crystallographic measurements were judged to be incompatible as they described the molecule as part of a larger solid structure, not the individual molecules we had set out to study. By adjusting the torsional temperature of the simulation and the vibrational energy spacing in the ground and excited states the experimental data could be successfully modelled. The antisymmetric torsional peaks were simulated almost exactly, with very little adjustment (other than torsional temperature) required. When determining the reduced moment of inertia it was found to be almost identical to that of BPEB. The peaks corresponding to the symmetric torsional motion, however, were more
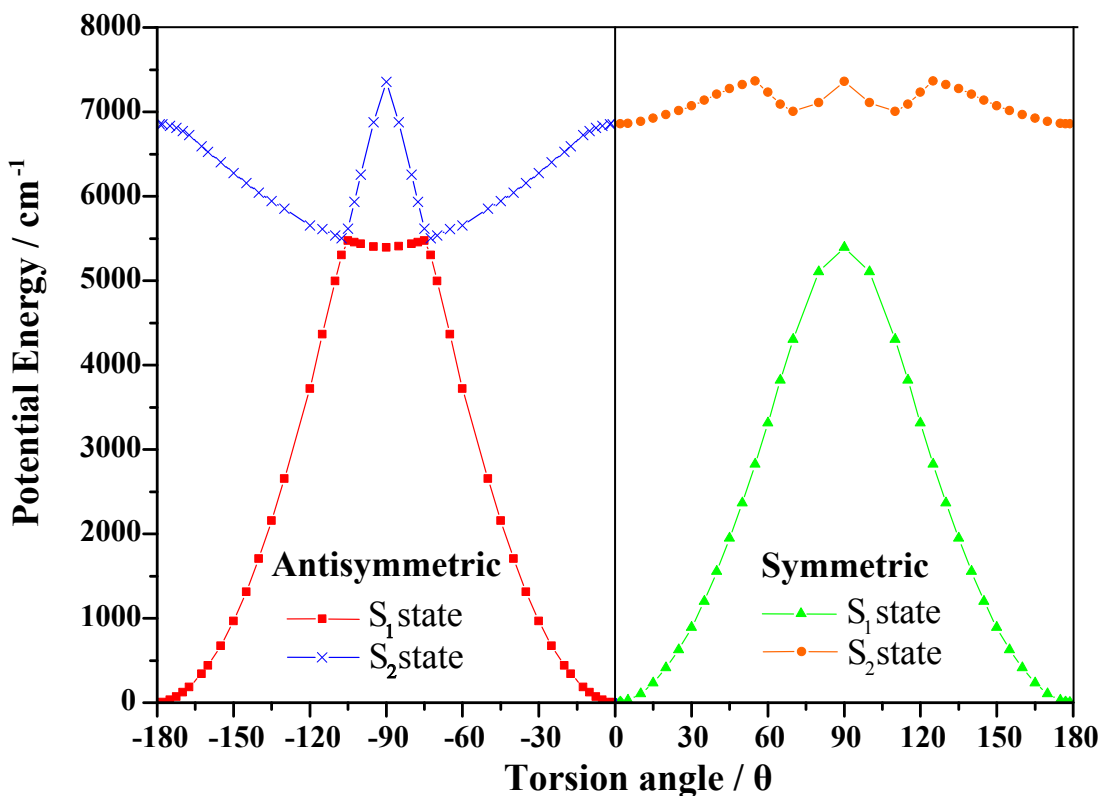
Figure 4.9: The first two singlet excited states of the BPET molecule as calculated using the optimised ground state geometries. Both the symmetric and antisymmetric torsion motions are shown.

difficult to fit to the experimental data. Using the calculated reduced moment of inertia resulted in a system which required vibrational energy spacing which made no sense in the experimental context. One approach to overcome this problem would be the development of a new simulation program. With the time constraints of the project an alternative was sought. It was found that with the input of a moment of inertia almost double the original the data could be successfully simulated.

The presence of the five-membered thiophene ring means the phenylethynyl substituents are offset from the straight axis by $\approx 60°$. This offset appeared not to influence the antisymmetric torsion of the phenyl rings when simulated using Gaussian09. The symmetric torsion, however, couples to the lowest energy out of plane bending vibration of the molecule. Coupling of these two different motions means the moment of inertia obtained for the symmetric twist does reflect the true value.

Analysis of the displacement of the rings from the plane of the molecule found that overall the largest deviation was 0.5° at a torsional angle of $\theta = 45°$, which was judged to be insufficient to cause any large scale problems with the fitting of the simulation parameters to the experimental spectrum. It was, however, acknowledged that this slight movement could alter the reduced moment of inertia of the molecule,

hence the input of an increased value in the simulation.

4.2.4 Spectral Interpretation

Peak Assignment

In the previous work by S. Greaves the torsional transitions of of BPEB were successfully assigned using the simulation program. Through comparison with deuterated BPEB spectra the transitions involving the symmetric torsional motion could unambiguously be assigned (Figure 4.10).
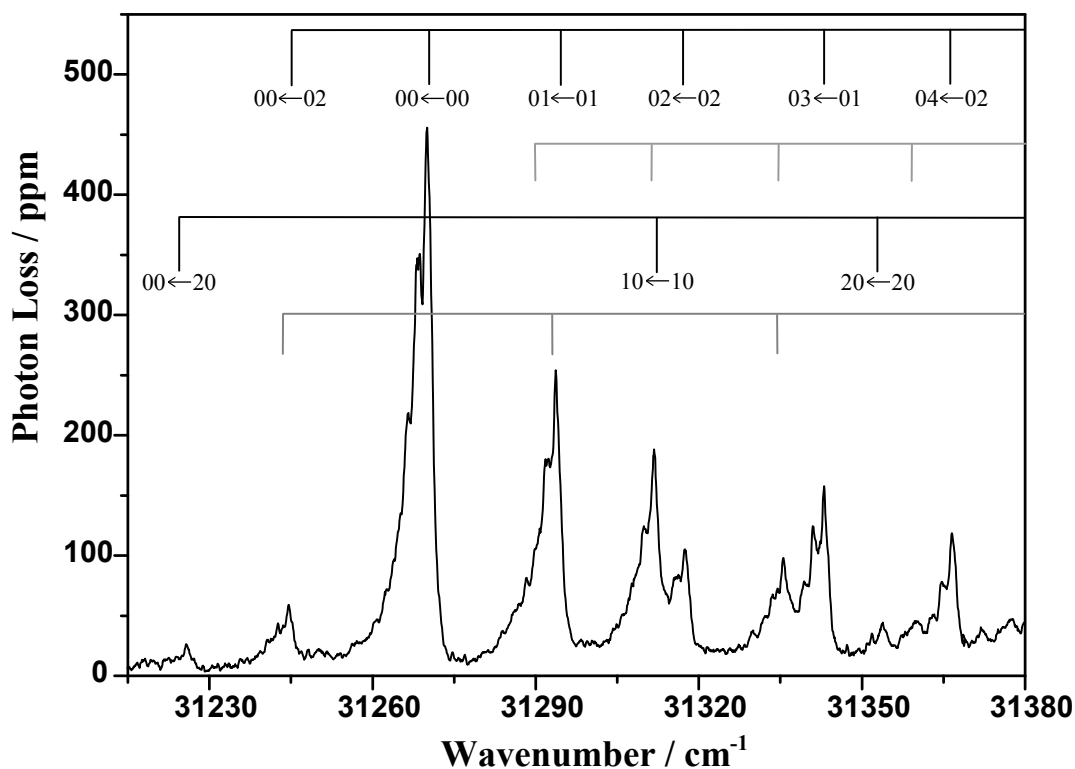
Figure 4.10: The absorption spectrum of BPEB similar to those obtained by S. Greaves. The vibrational progressions are shown for both the symmetric and antisymmetric torsional motions. The transitions are labeled as ($a's' \leftarrow a''s''$). Additionally, combination bands are indicated by grey lines.

A similar procedure using a deuterated thiophene was planned to aid in the analysis of the BPET spectrum. Unfortunately, owing to time restraints with the project, this was not possible. Using the knowledge gained during the assignment procedure of the BPEB absorption spectrum a similar process was repeated with the BPET experimental data and simulation program modelled spectrum (Figure 4.11).

Figure 4.11: Peak assignment of the BPET spectrum in which the antisymmetric transitions are represented in blue, symmetric in red and combination bands in green.

The spectral assignment initially required the identification of an absorption feature which corresponds to a hot band $(0 \leftarrow 2)$ of the symmetric and antisymmetric torsional motion. With the location of such features a value for the energy spacing in the ground state vibrational levels (harmonic vibrational constant, ν_e'') could be determine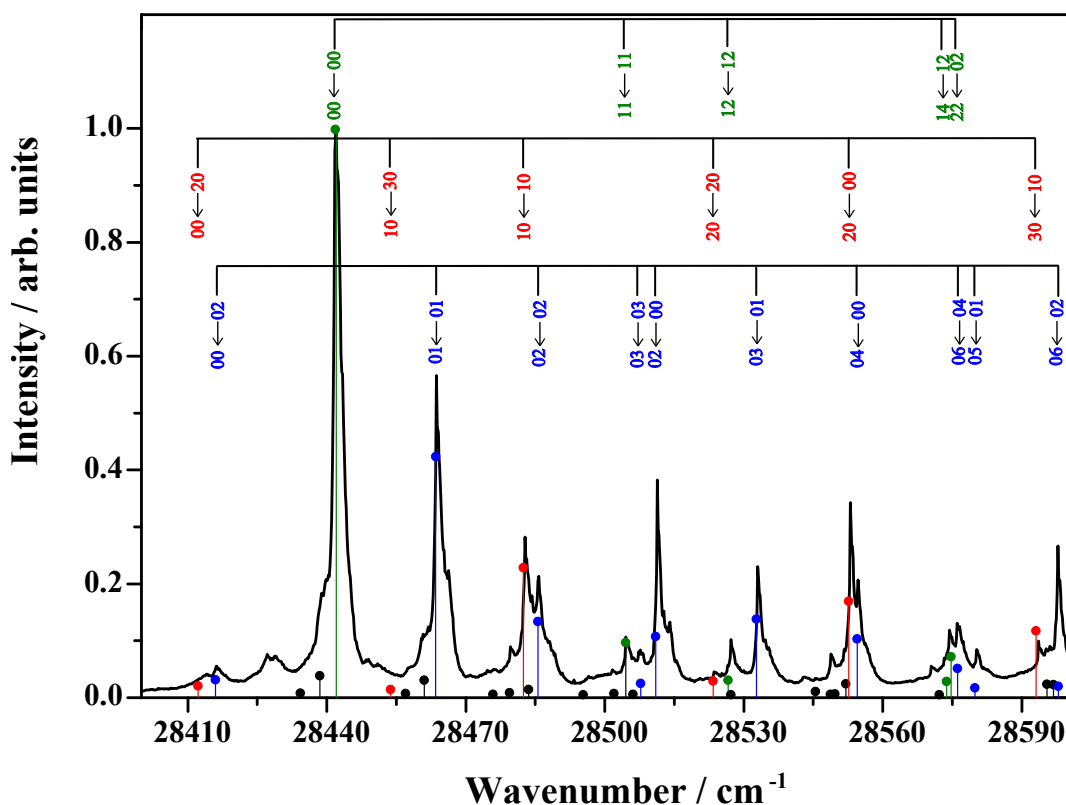d by finding the difference between these hot bands and the fundamental transition peak. With a value for this constant the other peaks can be fitted by altering the value of the vibrational constant in the excited state (ν_e'). In the fitting program the excited state is assumed to follow a similar shape to the ground state for its potential well. As a result of this a scaling factor can be used to acquire an approximate value for ν_e' for eventual refinement. The matching of the simulated peaks with those of the experimental data was performed until the two spectra showed good agreement by eye. This procedure, and increase in reduced moment of inertia for the symmetric torsional motion, resulted in the successful modelling of the BPET spectrum and assignment of the transition peaks.

While modelling the BPET spectrum with the simulation program it was found that the majority of the peaks could be successfully fitted with the exception of the $2 \leftarrow 0$ overtone. It was found that in the cooler (105°C oven temperature) spectra fit the $2 \leftarrow 0$ ovetone of the symmetric torsion displayed a calculated intensity greater

than that observed in the experimental data. The $2 \leftarrow 0$ antisymmetric overtone had a simulated intensity that was in good agreement with that obtained experimentally. The opposite trend was found in the hotter (120°C oven temperature) spectra, where the intensity of $2 \leftarrow 0$ symmetric torsion was in good agreement with the experimental data while the antisymmetric $2 \leftarrow 0$ transition was found to be significantly overestimated (Figure 4.12).

The discrepancies between the two temperature scans could be attributed to the temperature of the molecular beam. While carrying out the scans it was important to maintain a constant oven temperature. As the heating was controlled mainly with a lab power supply and a thermocouple for feedback the temperature was very limited with regards to accurate control. Consequently the temperature displayed by the thermocouple may not truly reflect the temperature at the centre of the oven and, more importantly, the molecular beam. Temperature changes during the scan could thus lead to one portion of the scan having a different temperature profile to earlier sections. Furthermore the sample may not sublimate at a constant rate, which could change the number density (and temperature) in the molecular beam.

With the simulation of the BPET spectrum the torsional energy of the system could be extracted from the data. The depth of the potential well, and hence the force constant, for each torsional motion is calculated using Equation (4.20).

$$k = \frac{d^2V}{d\theta^2} \tag{4.20}$$

The force constant, in this case, describes the restoring force ($-k$) needed when the substituents of the molecule rotate around the connecting ethynyl bond. As the model used to describe the potential well is

$$V = \frac{1}{2}V_{\max}(1 - \cos 2\theta) \tag{4.21}$$

the force constant is approximately proportional to

$$k = 2V_{\max} \tag{4.22}$$

From the parameters used in the spectral simulation an approximate number of ground state vibrational levels occupied in the molecular beam could be extracted. To establish a limit of detectable transitions only those with intensities $\geq 1\%$ of the $0 \leftarrow 0$ fundamental transition peak were considered. For the antisymmetric portion of the simulation the first eight vibrational levels possessed a sufficient population to
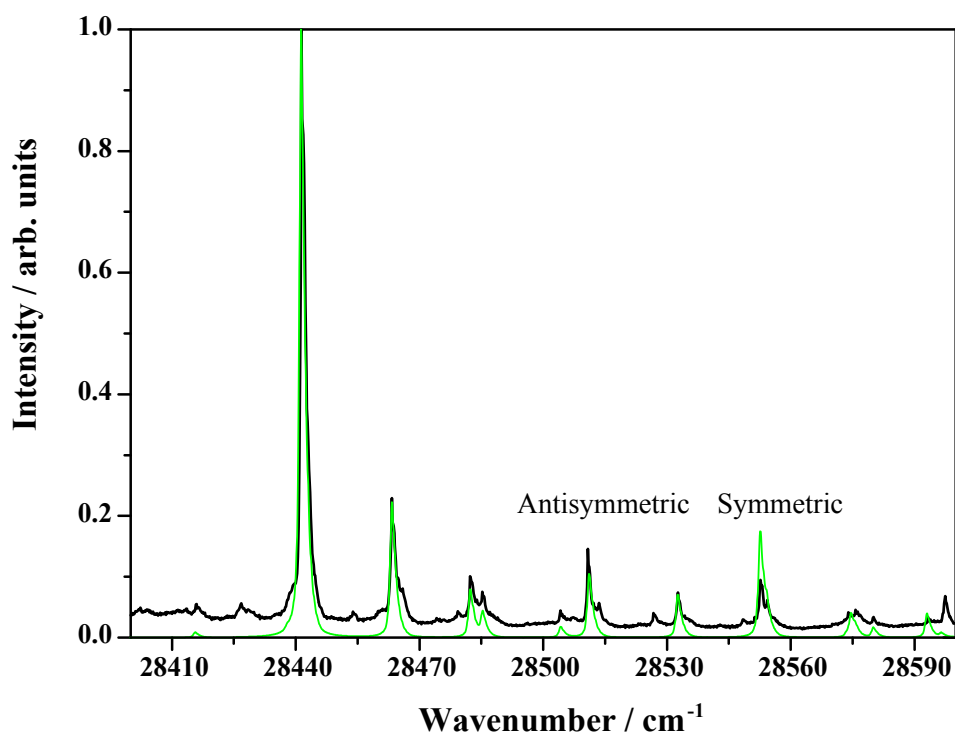
(a) CeLIF spectrum taken at an oven temperature of 105°C
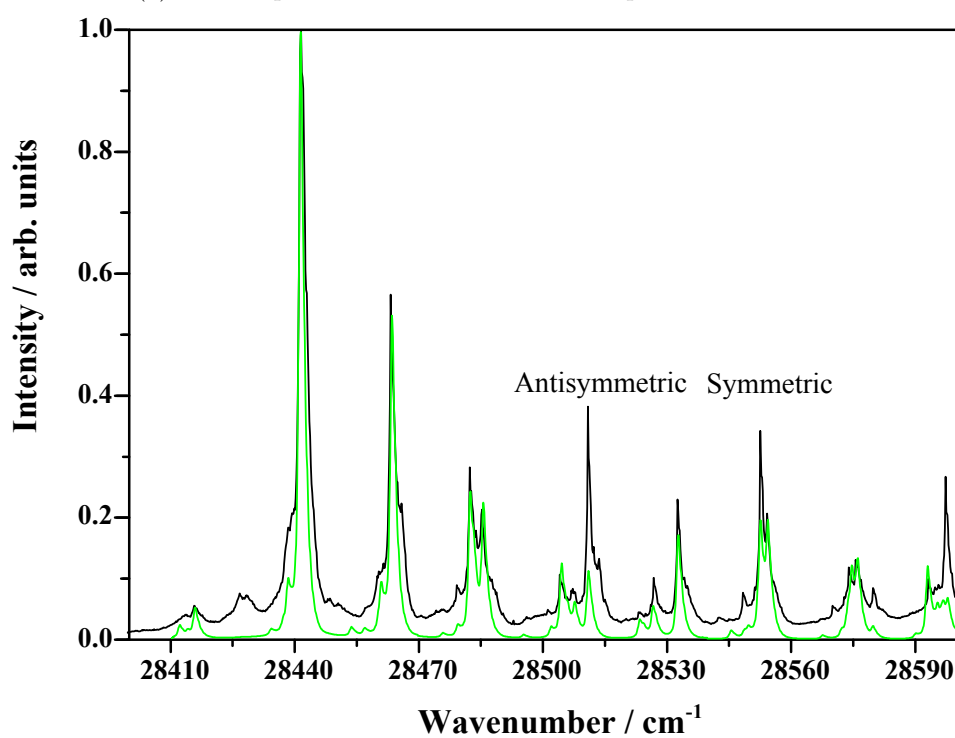
(b) CeLIF spectrum taken at an oven temperature of 120°C

Figure 4.12: The two CeLIF spectra (black) and their accompanying simulation (green) showing the $2 \leftarrow 0$ overtones, for both modes, recorded at two oven temperatures.

produce a sufficiently strong transition. The symmetric transitions, however, only resulted from the first four vibrational levels in the ground state (Figure 4.13).

Figure 4.13: From the simulation it has been found that only the first several energy levels of the BPET molecules were sufficiently populated to generate detectable transitions ($\geq 1\%$ of the $0 \leftarrow 0$ transition peak).

The potential well depths obtained from the simulation show the antisymmetric $V_{max} = 222$ cm^{-1} and symmetric $V_{max} = 233$ cm^{-1}, which are almost identical to the equivalent wells in BPEB[70] and similar to the well depth of 202 cm^{-1} obtained for tolane[23]
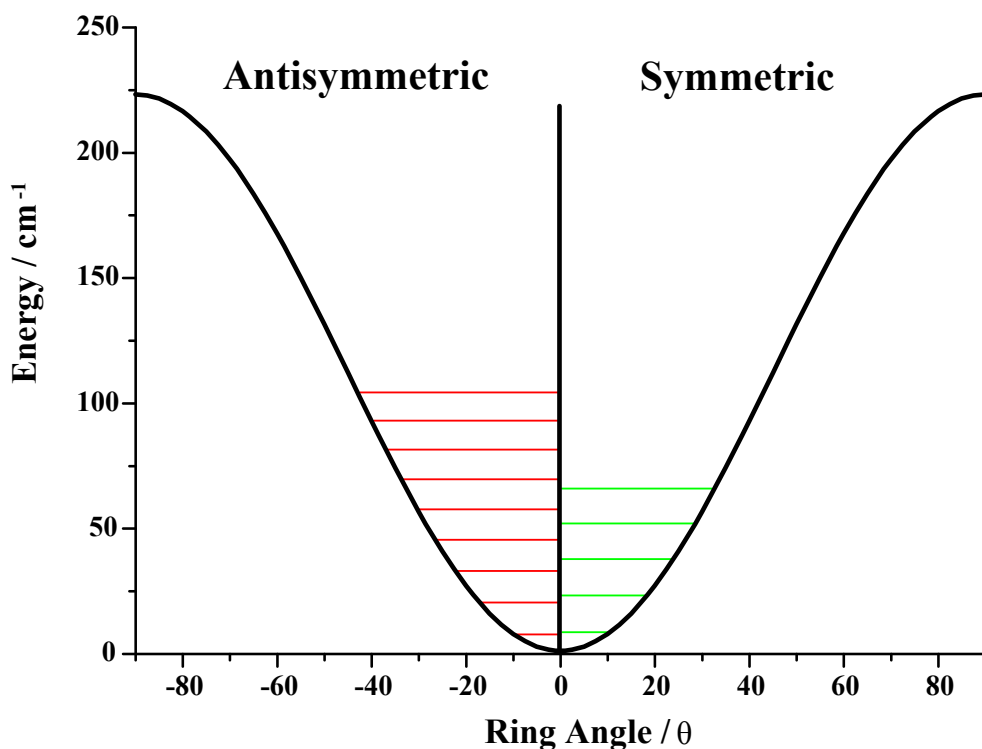
4.2.5 Comparison of BPET to BPEB

With the successful simulation of the spectrum of BPET a comparison with BPEB was possible (Table 4.3). From the data it can be seen that the two molecules share very similar characteristics. While the validity of the symmetric torsional force constant for BPET is questionable, the antisymmetric was modelled successfully. Comparison between the antisymmetric energy wells of the two molecules shows they are, for all intensive purposes, identical. With the problem of simulating the symmetric torsional transitions the value obtained can only be compared to the BPEB symmetric potential energy well sparingly. While the ground state potential well depths are similar, the excited state multiplication factor is significantly greater in the BPET compared to the BPEB. An overall comparison shows the two molecules require similar energy input to the torsional motions. This would indicate that altering the central ring in BPEB, to an equally simple non-substituted thiophene,

has little effect on increasing (or decreasing) the torsional barrier in the molecule. The geometry and π conjugation of the molecule also appears to have little influence on the delocalisation across the ethynyl bond as the sample goes from straight (BPEB) to bent (BPET). This comparison is based on the data obtained from this project using the Lumped Inertia methodology. The use of a more suitable simulation method, i.e. one which can account for the coupled vibrations of the symmetric torsional motion, would be better suited for a comparison of the two molecules.

Table 4.3: Comparison between the simulated spectra of BPET and that previously obtained for BPEB.[70]

Simulation Parameter	BPEB	BPET
T_{Torsion} / K	41 ± 1	40 ± 1
V_{max} (antisym) / cm^{-1}	222.82	222.07
V_{max} (sym) / cm^{-1}	232.76	233.57
Excited State Scaling Factor (antisym)	8	7.2
Excited State Scaling Factor (sym)	8	13.95

Chapter 5

Conclusion and Further Experimental Work

5.1 Conclusion

The addition of several new components to a cavity-ring down set-up has resulted in an experimental configuration with great possibilities for future use in the study of molecular wire candidates. A new sample oven has been developed and implemented with the potential to yield colder molecular beam temperatures. The capability to place a microphone into the molecular beam has resulted in a simple, effective method to measure the temporal profile of the gas pulse. The most important addition to the experiment was the inclusion of simple lens set-up to enable the collection of molecular fluorescence while maintaining the cavity, resulting in the CeLIF technique. This has enabled the project to proceed to its ultimate goal of measuring an absorption spectra of molecular wire candidate.

The fluorescence aspect of the experiment yielded a technique which shows great promise for application in spatially restricted, low number density environments, such as those in a molecular beam. When compared to both the original CRDS and the best single-pass LIF possible with the set-up CeLIF was found to perform in excess of either of the two single methods, with eventual detection sensitivities for photon loss per pass in the < 100 parts per billion range where we had previously been restricted to < 100 parts per million. Similar examples of simultaneous methods have been reported in the literature, with each group benefiting from the combination technique, be that for feature identification or determining density distribution.[96–98] None of these groups, however, explored the technique any further. With the increased sensitivity the set-up was able to successfully acquire

an absorption, and photoexcitation, spectrum of a new polyaromatic molecular wire candidate, 2,5-bis(phenylethynyl)thiophene (BPET).

With the successful recording of the BPET spectrum it was possible to simulate the transitions in the molecule and model the recorded data. The simulation was accomplished using a simple periodic potential, which has already been used in the simulation of the spectra of polyphenyl molecules tolane[23] and BPEB.[41] While the transitions corresponding to the antisymmetric torsional motion were well reproduced, difficulty was encountered when attempting to simulate the transitions corresponding to the symmetric torsional motions for our BPET spectra.

The potential well depth (V_{max}) determined from the simulation is approximately 220-235 cm^{-1}, which is virtually identical to values obtained for BPEB. The well depth is only an approximation as the transitions probed are towards the bottom of the well, meaning the fitting function used only simulates the shape of the bottom portion of the well and not the true barrier height. This is in stark contrast to the values obtained using DFT to calculate the potential well depth. This gives a value in the region of 700 cm^{-1}, which is very similar to the value obtained for BPEB. The value determined using the simulation program is open to scrutiny as the method employed in the analysis (lumped inertia technique) was developed for use with linear systems. Additionally, the problem of the determining the reduced moment of inertia of the symmetric torsion means a true idea of the potential well depth is difficult to determine.

5.2 Further Work

5.2.1 CeLIF Characterisation

Further characterisation of the CeLIF technique is an avenue which holds significant potential with respect to further analysis of these polyphenyl molecular wire species and in a more general aspect with other species in low number density, molecular beam environments. The effect of a species fluorescence lifetime on the quality of the CeLIF signal when compared to standard LIF measurements is of particular interest. The three molecules trialled in our CeLIF study (BPEB, DPB and BPET) all have solution fluorescence lifetimes of less than 1 ns (0.63 ns, 0.80 ns and 0.24 ns respectively)[19;90;112]. Performing the CeLIF measurements on a species which have a longer fluorescence decay time, which can be detected easily by a standard LIF set-up, would be a useful comparison to have between the two methods. With a sufficiently long fluorescence lifetime a species will generate sufficient data points

for analysis in its fluorescence transient, hence one of the main advantages of CeLIF will be lost. While SO_2 was given an initial trial using the CeLIF set-up a more robust analysis of different molecules is required for a more accurate comparison.

In addition to the CeLIF performance characteristics the technique could also be altered to employ dispersed fluorescence. With sufficient signal intensity the addition of this method would allow the collection of information concerning the higher vibrational levels within the ground state molecule. This would yield a better test for the fitting function used in the simulation program as the higher vibrational levels would increase the height of the potential well mapped, thus the model fit would need to describe more than the bottom portion of the well.

CeLIF is also currently under scrutiny for use in the research carried out by N.H. Nahler and O. Willis. Their investigation is concerned with studying the uptake and chemical reactions in and on ices contained within the stratosphere, more particularly the polar stratosphere, using CRDS. As the surface used to generate the ice is significantly smaller than the length of the laser axis used to produce a cavity ring-down signal CeLIF is being incorporated into the experiment to maximise the detection power of the set-up.

5.2.2   Future Experimental Development

Some of the simplest options for enhancing the experimental system is the alteration of backing pressure and also the sample oven. In the case of the backing pressure the set-up is limited by the ability of the current pumping system to remove the excess gas from the chamber. In order to successfully increase the backing pressure the chamber would require more powerful vacuum pumps to remove the higher gas load. Altering the oven to use a slit nozzle design is also a distinct possibility, as shown in the investigation by Fujiwara *et al.*[30] With the placement of the slit nozzle the group were able to obtain much cooler spectra of BPEB, seeded in molecular beam, as they could increase the laser absorption pathlength. Another limitation with the oven was the reliance on a small mass of BPEB, contained within the sample screw, for heating and subsequent analysis. An additional screw could be mounted into the oven to increase the available sample mass. The CeLIF already provides the ability to perform scans at lower temperatures, however, should a state not yield any fluorescence signal the technique would miss that particular spectral feature.

The initial aim of this research was the characterisation of substituted polyaromtic molecules. During feasibility studies on these species one of the main problems

encountered was the vapourisation point. As the General Valve nozzle has a limiting temperature alternatives to the "brute force" approach of severe heating need to be explored. One approach is the use of a laser ablation source to extract molecules for seeding in the molecular beam. By producing sample molecules in such a manner the energy within the species themselves is also significantly reduced, which may aid in obtaining colder molecular beam temperatures. Another possibility is the use of supercritical fluid in order to dissolve a portion of the sample and then release the resulting mixture into the chamber via a nozzle and shaped exit channel. The use of supercritical CO_2 would still satisfy the need for the pressure difference between the backing pressure and the vacuum environment, allowing the molecular beam analysis to be maintained.[113] A limitation with using this method is obviously ensuring the supercritical species has no/minimal absorption at the analytes wavelength and that the sample will dissolve in the supercritical fluid. The implementation of a supercritical fluid assembly would require significant investment and alteration to the apparatus.

With the suggestion of cluster formation in the molecular beam it may also be beneficial to include a mass spectrometer modification to the chamber to allow the detection of any species larger than our individual polyaromatics.

5.2.3   New Molecular Candidates

With the introduction of the CeLIF technique to the experimental set-up the work towards characterising the torsional motion of a range of polyphenyls can progress to cover a wider assortment of this class of molecules. During the initial stages of this research a variety of possible samples were investigated for their suitability for analysis using the cavity ring-down technique. While the majority failed-for various reasons-two potential candidates proved suitable for the investigation. These two were 1,4 diphenylbutadiyne, which was analysed as a trial for CeLIF, and the other 1-nitro, 4-phenylethynyl benzene, a tolane derivative containing an NO_2 substituent.

In addition to molecules which have already been analysed, the treatment could be extended to investigate other polyaromatic species based on the BPEB framework. Including substituted molecules is important for the eventual goal of the project in determining the change in orbital distribution in a molecular scale wire. With the addition of electron donating and withdrawing groups the molecules can mimic the environment between two electrodes. With analysis of these molecules it should elude to any changes in the molecular orbitals and how this influences the torsional motion around the ethynyl bridges. As the lumped inertia technique displays a reliance on the symmetry of the molecule treated,[48] future candidates should be

symmetric, where possible, to aid in simplifying the analysis. This can extend to a whole range of potential options for the configuration of the molecules, with one such interesting example being 1,4-bis(2,4,6-tri*tert*butylphenylethynyl)-2,3,5,6-tetramethylbenzene (Figure 5.1).[107] Owing to this molecule possessing a number of large substituents the steric interactions of the structure are such that the ground state configuration has the central ring positioned at 90° to the two external ring units.[114] With this behaviour the molecule satisfies one of the main requirements of functioning as a molecular scale switch.
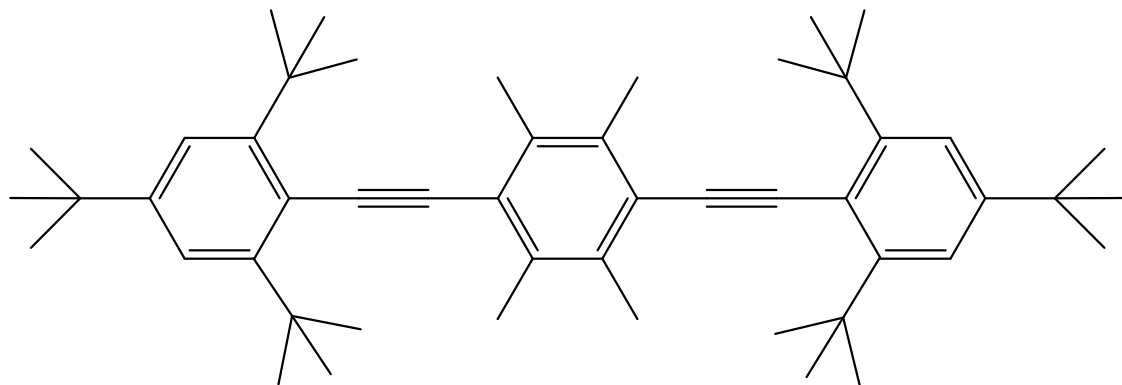
Figure 5.1: 1,4-bis(2,4,6-tri*tert*butylphenylethynyl)-2,3,5,6-tetramethylbenzene

A more refined simulation program would be a useful addition to the research. As already mentioned the lumped inertia method was developed for use with linear systems. An alternative model for use with non-linear systems would be highly beneficial to this work. Of particular importance would be a way to accurately determine the moment of inertia, should a similar problem of mode mixing be encountered.

Bibliography

[1] Tipler, P. A. and Mosca, G. *Physics for Scientists and Engineers.* Freeman, (2004).

[2] Low, P. J. *Dalton Trans.* **17**, 2821–2824 (2005).

[3] Turro, N. J., Ramamurthy, V., and Scaiano, J. *Principles of Molecular Photochemistry : An Introduction.* University Science Books, (2009).

[4] Oevering, H., Paddon-Row, M. N., Heppener, M., Oliver, A. M., Cotsaris, E., Verhoeven, J. W., and Hush, N. S. *J. Am. Chem. SOC* **109**, 3258–3269 (1987).

[5] Lambert, C., Noll, G., and Schelter, J. *Nat. Mat.* **1**, 69–73 (2002).

[6] Aviram, A. and Ratner, M. A. *Chem. Phys. Lett* **29**, 277–283 (1974).

[7] Chiang, C. K., Fincher, C. R., Park, W., Heeger, A. J., Shirikawa, H., Louis, E. J., Gau, S. C., and MacDairmid, A. C. *Phys. Rev. Lett* **39**, 1098–1101 (1977).

[8] Friend, R. H., Gymer, R. W., Holmes, A. B., Burroghes, J. H., Marks, R. N., Taliani, C., Bradley, D. D., Santos, D. A. D., Bredas, J. L., Logdlund, M., and Salaneck, W. R. *Nature* **397**, 121–128 (1999).

[9] Kelly, S. O. and Barton, J. K. *Science* **283**, 375–381 (1999).

[10] Porath, D., Bezryadin, A., de Vries, S., and Dekker, C. *Nature* **403**, 635–638 (2000).

[11] Shirikawa, H., Louis, E. J., MacDairmid, A. G., Chiang, C. K., and Heeger, A. J. *J. C. S. Chem Comm* **16**, 578–580 (1977).

[12] Harriman, A. and Ziessel, R. *Chem. Comm* , 1707–1716 (1996).

[13] Wagner, R. W. and Lindsey, J. S. *J. Am .Chem. Soc* **116**, 9759–9760 (1994).

[14] Collin, J., Laine, P., Launay, P., Sauvage, J., and Sour, A. *J. Chem. Soc. Chem. Commun* , 434–495 (1993).

[15] Benniston, A. C., Harriman, A., Rewinska, D. B., Yang, S., and Zhi, Y. *Chem. Eur. J.* **13**, 10194–10203 (2007).

[16] Chen, J., Reed, M. A., Rawlett, A. M., and Tour, J. M. *Science* **286**, 1550–1552 (1999).

[17] Seminario, J., Zacarias, A. G., and Tour, J. M. *J. Am. Chem. Soc* **120**, 3970–3974 (1998).

[18] Chen, J., Wang, W., and Reed, M. A. *Appl. Phys. Lett* **77**, 1224–1226 (2000).

[19] Beeby, A., Findlay, K., Low, P. J., and Marder, T. B. *J. Am .Chem. Soc* **124**, 8280–8284 (2002).

[20] Mavridis, A. *Acta. Cryst* **B33**, 3612–3615 (1977).

[21] Liberles, A. and Matlosz, B. *J. Org. Chem* **36**, 2710–2713 (1971).

[22] Ferrante, C., Kensy, U., and Dick, B. *J. Phys. Chem.* **97**, 13457–13463 (1993).

[23] Okuyama, K., Hasegawa, T., Ito, M., and Mikami, N. *J. Phys. Chem.* **88**, 1711–1716 (1984).

[24] Hirata, Y., Okada, T., and Nomoto, T. *Chem. Phys. Lett* **293**, 371–377 (1998).

[25] Abramenkov, A. V., Almenningen, A., Cyvin, B. N., Cyvin, S. J., Jonvik, T., Khaikin, L. S., Romming, C., and Vilkov, L. V. *Acta. Chem. Scand.* **42A**, 674–684 (1988).

[26] Zgierski, M. Z. and Lim, E. C. *Chem. Phys. Lett* **393**, 143–149 (2004).

[27] Beeby, A., Findlay, K. S., Low, P. J., Marder, T. B., Matousek, P., Parker, A. W., Rutter, S. R., and Towrie, M. *Chem. Comm* , 2406–2407 (2003).

[28] Kohler, A. and Beljonne, D. *Adv. Funct. Mater.* **14**, 11–18 (2004).

[29] Biswas, M., Nguyen, P., Marder, T. B., and Khundkar, L. R. *J. Phys. Chem. A* **101**, 1689–1695 (1997).

[30] Fujiwara, T., Zgierski, M. Z., and Lim, E. C. *J. Phys. Chem. A* **112**, 4736–4741 (2008).

[31] Levitus, M., Schmieder, K., Ricks, H., Shimizu, K. D., Bunz, U. H. F., and Garcia-Garibay, M. A. *J. Am. Chem. Soc* **123**, 4259–4265 (2001).

[32] Levitus, M., Schmieder, K., Ricks, H., Shimizu, K. D., Bunz, U. H. F., and Garcia-Garibay, M. A. *J. Am . Chem. Soc* **124**, 8181 (2002).

[33] Magyar, R. J., Tretiak, S., Gao, Y., Wang, H.-L., and Shreve, A. P. *Chem. Phys. Lett* **401**, 149–156 (2005).

[34] Levitus, M. and Garcia-Garibay, M. A. *J. Phys. Chem. A* **104**, 8632–8637 (2000).

[35] Reichert, J., Ochs, R., Beckmann, D., Weber, H. B., Mayor, M., and Lohneysen, H. *Phys. Rev. Lett* **88**, 176804 (2002).

[36] Seminario, J. M., Zacarias, A. G., and Tour, J. M. *J. Am. Chem .Soc* **122**, 3015–3020 (2000).

[37] Donhauser, Z. J., Mantooth, B. A., Kelly, K. F., Bumm, L. A., Monnell, J. D., Stapleton, J. J., Jr, D. W. P., Rawlett, A. M., Allara, D. L., Tour, J. M., and Weiss, P. S. *Science* **292**, 2303–2307 (2001).

[38] Reed, M. A., Chen, J., Rawlett, A. M., Price, D. W., and Tour, J. M. *Appl Phys Lett* **78**, 3735–3737 (2001).

[39] Kruger, D., Fuchs, H., Rousseau, R., Marx, D., and Parrinello, M. *Phys. Rev. Lett* **89**, 186402 (2002).

[40] Sluch, M. I., Godt, S., Bunz, U. H. F., and Berg, M. A. *J. Am. Chem .Soc* **123**, 6447 (2001).

[41] Greaves, S. J., Flynn, E. L., Futcher, E. L., Wrede, E., Lydon, D. P., Low, P. J., Rutter, S. R., and Beeby, A. *J. Phys. Chem. A* **110**, 2114–2121 (2006).

[42] Englert, B. C., Smith, M. D., Hardcastle, K. I., and Bunz, U. H. F. *Macromolecules* **37**, 8212–8221 (2004).

[43] Reinerthy, W. A., IIy, L. J., Burginy, T. P., Zhouz, C., Mullerz, C. J., Deshpandez, M. R., Reedz, M. A., and Toury, J. M. *Nanotechnology* **9**, 246–250 (1998).

[44] Fernholt, L., Romming, C., and Samdal, S. *Acat. Chemica. Scandinavica* **35A**, 707–715 (1981).

[45] Goller, A., Klemm, E., and Egbe, D. A. M. *Int. Journ. Quant. Chem* **84**, 86–98 (2001).

[46] Saebo, S., Almlof, J. G., Stark, J. E., and Boggs, J. *J. Mol. Struc* **200**, 361 (1989).

[47] Xu, D. and Cooksy, A. L. *J. Mol. Struc:THEOCHEM* **815**, 119–125 (2007).

[48] Zheng, X., Vedova-Brook, N., and Sohlberg, K. *J. Phys. Chem. A* **108**, 2499–2507 (2004).

[49] Halkyard, C. E., Rampey, M. E., Kloppenburg, L., Struder-Martinez, S. L., and Bunz, U. H. F. *Macromolecules* **31**, 8655–8659 (1998).

[50] Miteva, T., Palmer, L., Kloppenburg, L., Neher, D., and Bunz, U. H. F. *Macromolecules* **33**, 652–654 (2000).

[51] Naus, H. and Ubachs, W. *Opt. Lett* **25**, 347–349 (2000).

[52] Brown, S. S., Stark, H., and Ravishankara, A. R. *Appl. Phys. B* **75**, 173–182 (2002).

[53] Dube, W. P., Brown, S. S., Osthoff, H. D., Nunley, M. R., Ciciora, S. J., Paris, M. W., Mclaughlin, R. J., and Ravishankara, A. R. *Rev. Sci. Inst* **77**, 034101 (2006).

[54] Smets, A. H. M., van Helden, J. H., and van Sanden, M. C. M. *Journal of Non-Crystalline Solids* **299**, 610–614 (2002).

[55] Aarts, I. M. P., Hoex, B., Smets, A. H. M., Engeln, R., Kessels, W. M. M., and van de Sanden, M. C. M. *App. phys. lett.* **84**, 3079–3081 (2004).

[56] Kleine, D., Lauterbach, J., Kleinermanns, K., and Hering, P. *Appl. Phys. B.* **72**, 249–252 (2001).

[57] Hallock, A. J., Berman, E. S. F., and Zare, R. N. *Anal. Chem* **74**, 1741–1743 (2002).

[58] Xu, S., Sha, G., and Xie, J. *Rev. Sci. Inst* **73**, 255–258 (2002).

[59] Schnippering, M., Neil, S. R. T., Mackenzie, S. R., and Urwin, P. R. *Chem. Soc. Rev.* **40**, 207–220 (2011).

[60] Chen, M. S., Fan, H. F., and Lin, K. C. *Anal. Chem* **82**, 868–877 (2010).

[61] Okeefe, A. and Deacon, D. A. G. *Rev. Sci. Inst* **59**(12), 2544–2551 (1988).

[62] Herbelin, J. M., McKay, J. A., Kwok, M. A., Ueunten, R. H., Urevig, D. S., Spencer, D. J., and Benard, D. J. *Appl. Opt.* **19**(1), 144–147 (1980).

[63] Anderson, D. Z., Frisch, J. C., and Masser, C. S. *Appl. Opt.* **23**(8), 1238–1245 (1984).

[64] Andrews, D. L. *Lasers in Chemistry.* Springer, (1997).

[65] Brooker, G. *Modern Classical Optics.* Oxford University Press, (2008).

[66] Lee, D., Yoon, Y., Kim, B., Lee, J., Yoo, Y., and Hahn, J. *Appl. Phys. B* **74**, 435–440 (2002).

[67] Hodges, J. T., Looney, J. P., and van Zee, R. D. *J. Chem. Phys.* **105**, 10278–10288 (1996).

[68] Berden, G. and Engeln, R. *Cavity Ring-Down Spectroscopy: Techniques and Applications.* Wiley, (2009).

[69] Scherer, J. J., Paul, J. B., OKeefe, A., and Saykally, R. J. *Chem. Rev.* **97**, 25–51 (1997).

[70] Greaves, S. J. *Theoretical and Experimental Studies of Molecular Motions and Reaction Mechanisms.* PhD thesis, Durham University, (2005).

[71] Atkins, P. and de Paula, J. *Atkins' Physical Chemistry.* Oxford, 7th edition, (2002).

[72] Scoles, G. *Atomic and Molecular Beam Methods.* Oxford University Press, (1988).

[73] Estermann, I. *Rev. Mod. Phys* **18**, 300–323 (1946).

[74] Snoek, L., Robertson, E., Kroemer, R., and Simons, J. *Chem. Phys. Lett* **321**, 49–56 (2000).

[75] Hillenkamp, M., Keinan, S., and Even, U. *J. Chem. Phys.* **118**, 8699–8705 (2003).

[76] Lee, S., Hoobler, R. J., and Leone, S. R. *Rev. Sci. Inst.* **71**, 1816–1823 (2000).

[77] Yariv, A. *Optical electronics in modern communications.* Oxford University Press, 5th edition, (1997).

[78] Orr-Ewing, A. J. and Rennick, C. J. Private Communication, University of Bristol.

[79] Hirata, Y., Okada, T., Mataga, N., and Nomoto, T. *J. Phys. Chem.* **96**, 6559–6563 (1992).

[80] Herschel, J. *Philiosphical Transactions of the Royal Society of London* , 143–145 (1845).

[81] Herschel, J. *Philiosphical Transactions of the Royal Society of London* , 147–153 (1845).

[82] Brewster, D. *Philiosphical Transactions of the Royal Society of London* , 401–412 (1848).

[83] Stokes, G. G. *Philiosphical Transactions of the Royal Society of London* , 463–561 (1852).

[84] Kopfermann, H. and Ladenburg, R. *Nature* **122**, 438–439 (1928).

[85] Fairbank, W. M., Hansch, T. W., and Schawlow, A. L. *J. Opt. Soc. Am.* **65**(2), 199–204 (1975).

[86] Lakowicz, J. L. *Principles of Fluorescence.* Springer, third edition, (2006).

[87] Brus, L. E. and McDonald, J. R. *J. Chem. Phys* **61**, 97–105 (1974).

[88] Rufus, J., Stark, G., Smith, P. L., Pickering, J. C., and Thorne, A. P. *Journal of Geophysical Research* **108** (2003).

[89] Biswal, S. B., Kumar, S. V. K., and Wategaonkar, S. J. *J. Chem. Phys.* **128**, 204312 (2008).

[90] Nagano, Y., Ikoma, T., Akiyama, K., and Tero-Kubota, S. *J. Am .Chem. Soc* **125**, 14103–14112 (2003).

[91] Surette, J. K. D., MacDonald, M., Zaworotko, M. J., and Singer, R. D. *J. Chem. Crys* **24**, 715–717 (1994).

[92] Chung, C. B., Kim, G., Kwon, J. H., and Shim, S. C. *Bull. Korean. Chem. Soc* **14**, 506–510 (1993).

[93] Yoneda, H., Hiura, H., and Takahashi, H. *J. Mol. Struc.* **301**, 47–56 (1993).

[94] Nagano, Y., Ikoma, T., Akiyama, K., and Tero-Kubota, S. *J. Phys. Chem. A* **102**, 5769–5774 (1998).

[95] Thomas, R., Mallajyosula, S. S., Lakshmi, S., Pati, S. K., and Kulkarni, G. U. *J. Mol. Struc* **922**, 46–50 (2009).

[96] Luque, J., Berg, P. A., Jeffries, J. B., Smith, G. P., Crosley, D. R., and Scherer, J. J. *Appl. Phys. B.* **78**, 93–102 (2004).

[97] Tokaryk, D. W., Adam, A. G., and Slaney, M. E. *Chem. Phys. Lett.* **433**, 264–267 (2007).

[98] Hagemeister, F. C., Arrington, C. A., Giles, B. J., Quimpo, B., Zhang, L., and Zwier, T. S. *Cavity Ring-Down Spectroscopy: An Ultimate-Absorption Measurement Technique.* American Chemical Society, (1999).

[99] Brown, S. S., Ravishankara, R. A., and Stark, H. *J. Phys. Chem. A* **104**, 7044–7052 (2000).

[100] Lind, P., Lopes, C., Oberg, K., and Eliasson, B. *Chem. Phys. Lett* **387**, 238–242 (2004).

[101] Lind, P., Eriksson, A., Lopes, C., and Eliasson, B. *J. Phys. Org. Chem* **18**, 426–433 (2005).

[102] Rodriguez, J. G., Lafuente, A., Rubio, L., and Esquivias, J. *Tet. Lett.* **45**, 7061–7064 (2004).

[103] Jung, T. S., Kim, J. H., Jang, E. K., Kim, D. H., Shim, Y., Park, B., and Shin, S. C. *J. Organomet. Chem* **599**, 232–237 (2000).

[104] Kergueris, C., Bourgoin, J. P., Palacin, S., Esteve, D., Urbina, C., Magoga, M., and Joachim, C. *Phys. Rev. B* **59**, 12505–12513 (1999).

[105] Casado, J., Hicks, R. G., Hernandez, V., Myles, D. J. T., Delgrado, M. C. R., and Navarrete, J. T. L. *J. Chem. Phys.* **118**, 1912–1920 (2003).

[106] Wada, Y. *Atomic and Molecular Wires.* Kluwer Academic, Dordrecht, (1997).

[107] Rutter, S. R. *PhD Thesis.* PhD thesis, Durham University, (2007).

[108] Sohlberg, K., Sumpter, B. G., Tuzun, R. E., and Noid, D. W. *Nanotechnology* **9**, 30–36 (1998).

[109] Qiao, H., Li, Q. S., and Li, G. Q. *J. Vib. Acoust* **124**, 656–659 (2002).

[110] J. D. Lewis, T. B. Malloy Jr, T. H. C. and Laane, J. *J. Mol. Struct* **12**, 427–449 (1972).

[111] Hollas, J. M. *Modern Spectroscopy.* Wiley, (2008).

[112] Siddle, J. S., Ward, R. M., Collings, J. C., Rutter, S. R., Porres, L., Applegarth, L., Beeby, A., Batsanov, A. S., Thompson, A. L., Howard, J. A. K., Boucekkine, A., Costuas, K., Halet, J., and Marder, T. B. *New. J. Chem* **31**, 841–851 (2007).

[113] Suarez, J. J., Bueno, J. L., and Madina, I. *Chemical Engineering Science* , 2419–2427 (1993).

[114] Beeby, A. Private Communication.